A MICROWAVE BACKSCATTERING MODEL FOR PRECIPITATION

by

SEDA ERMIS

Presented to the Faculty of the Graduate School of

The University of Texas at Arlington in Partial Fulfillment

of the Requirements for the Degree of

DOCTOR OF PHILOSOPHY

THE UNIVERSITY OF TEXAS AT ARLINGTON

August 2015

When you go through a hard period, when everything seems to oppose you, when you feel you cannot even bear one more minute, never give up! Because it is the time and place that the course will divert!

Mevlana Celaleddin Rumi, The Essential Rumi

Acknowledgements

Firstly I would like to thank my supervisor, Dr. Saibun Tjuatja, not just for giving me the opportunity to pursue my PhD degree under his guidance, but also for his support, and encouragement over the period that I spent to complete my degree. Without his guidance and patience throughout my study, this thesis could not have been accomplished. I would also like to thank Dr. Jonathan W. Bredow, Dr. Dong-Jun Seo, Dr. W. Alan Davis, and Dr. Ioannis D. Schizas for serving on my dissertation committee. I appreciate for their valuable time to review my dissertation and attend my defense. I am very thankful to Dr. Krzysztof A. Orzel. His support and important contribution to bring this work to completion.

I am deeply grateful to my father; Seref Ermis, my mother; Nevin Ermis and my little sister; Gozde Ermis for their unconditional love, care, support and effort to keep me motivated in this long journey. I am truly thankful having them in my life. Special thanks to all my relatives, especially Tulay Erdim who has always been there for me through my tough times.

Last, but not least, I send big thanks to all my friends in here and in Turkiye, because each of you brings something wonderful to my life. Gul Karaduman deserves special recognition and thanks for being there to help me in anyway possible till the last moment.

July 14, 2015

Abstract

A MICROWAVE BACKSCATTERING MODEL FOR PRECIPITATION

Seda Ermis, PhD

The University of Texas at Arlington, 2015

Supervising Professor: Saibun Tjuatja

A geophysical microwave backscattering model for space borne and ground-based remote sensing of precipitation is developed and used to analyze backscattering measurements from rain and snow type precipitation. Vector Radiative Transfer (VRT) equations for a multilayered inhomogeneous medium are applied to the precipitation region for calculation of backscattered intensity. Numerical solution of the VRT equation for multiple layers is provided by the matrix doubling method to take into account close range interactions between particles.

In previous studies, the VRT model was used to calculate backscattering from a rain column on a sea surface [41]. In the model, Mie scattering theory for closely spaced scatterers was used to determine the phase matrix for each sublayer characterized by a set of parameters. The scatterers i.e. rain drops within the sublayers were modelled as spheres with complex permittivities. The rain layer was bounded by rough boundaries; the interface between the cloud and the rain column as well as the interface between the sea surface and the rain were all analyzed by using the integral equation model (IEM). Therefore, the phase matrix for the entire rain column was generated by the combination of surface and volume scattering [41]. Besides Mie scattering, in this study, we use T-matrix approach to examine the effect of the shape to the backscattered intensities since larger raindrops are most likely oblique in shape. Analyses show that the effect of

obliquity of raindrops to the backscattered wave is related with size of the scatterers and operated frequency.

For the ground-based measurement system, the VRT model is applied to simulate the precipitation column on horizontal direction. Therefore, the backscattered reflectivities for each unit range of volume are calculated from the backscattering radar cross sections by considering radar range and effective illuminated area of the radar beam. The volume scattering phase matrices for each range interval are calculated by Mie scattering theory. VRT equations are solved by matrix doubling method to compute phase matrix for entire radar beam. Model results are validated with measured data by X-band dual polarization Phase Tilt Weather Radar (PTWR) for snow, rain, wet hail type precipitation. The geophysical parameters given the best fit with measured reflectivities are used in previous models i.e. Rayleigh Approximation and Mie scattering and compared with the VRT model. Results show that reflectivities calculated by VRT models are differed up to 10 dB from the Rayleigh approximation model and up to 5 dB from the Mie Scattering theory due to both multiple scattering and attenuation losses for the rain rates as high as 80 mm/h.

Table of Contents

List of Illustrations

List of Tables

Chapter 1

Introduction

Since precipitation is the major interest of many study areas such as hydrology, meteorology, agriculture or geology, accurate estimation of precipitation has been took more attention not only for better understanding of geophysical process of precipitation but also for the analyze the serious consequences of weather-related problems on human life [1].

Initial measurements of precipitation by using rain gauges on the ground, have eventually been evolved by using more advanced version of similar direct observation devices (e.g. autographic rain gauges). The precipitation data collected over years has been subject to regional and later on, global climatological studies to retrieve the spatial or temporal parameters of precipitation [2]. Especially, in the second half of the 20th century, our knowledge about spatial and temporal view of precipitation has expanded by taking advantage of technologically sophisticated devices which are located either on the earth's surface (e.g., ground-based radars, disdrometers) or aboard space platforms (e.g., spaceborne radars, microwave sensors), and it has guided us to better understanding of the formation, composition and of the physical process underlying [2]. In this respect, using remote sensing for the quantitative estimation of precipitation has played a crucial role, and today, the use of radars is widely spread.

The most important reason behind using a radar system in precipitation estimation instead of rain gauges is that radars can sample a large area (>30,000 km^2 for a weather radar sampling out to 100 km) in a short period of time (<5min) to provide information of spatial or temporal movement of precipitation [3]. Moreover, using dual-polarization radar systems instead of the traditional single-polarization radar systems in the last decade has allowed researchers to get additional information about hydrometeors shape, size, or composition from radar echo [3].

However, radar does not measure the precipitation rate directly, but rather the backscattered energy from many illuminated precipitation hydrometeors at the same time, in the elevated radar beam. Therefore, since the aim of rainfall retrieval algorithms is to estimate geophysical parameters for different types of precipitation hydrometeors, most studies based on inverse modelling of precipitation have aimed extracting rainfall rate information from reflected wave [3]. For this purpose, many empirical reflectivity-rain rate models were published by specifying hydrometeors size distribution [3,4,5,6]. The basic advantages of empirical models are to provide simpler calculation and easier implementation. However, the major problem is their applicability for the weather events which are not observed frequently and have not been considered as a case in the algorithm. Another modelling technique is based on the calculation of the scattered wave from known geophysical parameters i.e. forward modelling. The advantage of the forward modelling is that it allows a way to analyze the effect of geophysical parameters on the backscattered wave and to interpret the measured data [7,8]

In this study, a geophysical model based on the forward modelling technique is applied to spaceborne and ground-based remote sensing of precipitation. This is used to analyze rain and snow type precipitation. The basic assumption considered in most modelling studies is the independent scattering approximation which implies that light precipitation rate and small size scatterers with respect to wavelength [9,10,11,12]. Therefore, the close range interactions between scatterers are ignored. This assumption is valid for light to moderate rainfall events. However; in the case of high rain rate, this assumption may cause inaccurate estimation of geophysical parameters. As a result, a scattering model which considers multiple scattering effects for accurately estimating precipitation from lower to higher rates is needed.

1.1 Previous Works

In the modelling of scattering from natural terrains, both rough surface scattering and volume scattering theories have fundamental importance. Reviews of developed rough surface scattering and volume scattering theories in literature is given by Fung and Ulaby [7,8,13].

Although several surface scattering models such as the Kirchhoff rough surface scattered model [14] or the small perturbation model [15] were studied in the past, the Integral Equation Model (IEM) proposed by Fung is valid for arbitrary roughness if the standard deviation of the surface height is less than 0.4 [16]. Also, the IEM model was summarized and used by Tjuatja for the modelling of snow or sea ice layer to account for interactions between interfaces with the inhomogeneities in media [17]

Among the volume scattering models, the Vector Radiative Transfer (VRT) theory, developed by Chandresekar [18], has been widely used by many investigators [19,20,21]. The formulation of the VRT, which is given in detail in Chapter 2, is governed by the propagation of specific intensity through a medium and so, the phase changing of the scattered wave is ignored [17, 37]. Furthermore, since it is assumed that there is no correlation between scattered fields in the conventional VRT model, the distance between scattered should be far enough with respect to wavelength to apply the theory. Although there is no closed form analytical solution of the VRT equations for an inhomogeneous medium embedded with discrete scatters, many numerical solution techniques have been used [7]. One numerical technique is the matrix doubling method which was investigated by many authors [22,23] and generalized by taking into account irregular boundary and dense medium effects for small scatterers [24]. Besides, Tjuatja [17] considered a multilayer inhomogeneous medium with irregular interfaces and extended the model to include vertical variations. To take into account the phase interference effects of closely spacing scatterers, he used Mie scattering calculation for closely packed spheres inside the conventional VRT theory to calculate volume scattering phase matrices for each infinitesimal layer [17]. Mie scattering theory was originally developed by Gustav Mie in 1908, and it has been extended by considering wider range of size, and material properties. Further details are provided by Bohren and Huffman [25], and Van de Hulst [26].

In this study, beside Mie scattering for spherical shape scatterers, the T-matrix approach was used inside the multiple layer VRT model to calculate scattered field for nonspherical scatters. The T-matrix approach, also known as the extended boundary condition method, was introduced by Waterman [27] and improved by Mishchenko with the analytical orientation averaging procedure for an arbitrary multi-sphere cluster by means of superposition future of the T-matrix [28]. In this study both the Mie scattering theory and the T-matrix approach are used for the construction of volume scattering phase matrices as explained in Chapter.2. One application of the multiple layer VRT model is the calculation of backscattering intensities from precipitation hydrometeors. This is the overall goal of this study.

In 1983, Oguchi summarized the theories and numerical calculations relate to electromagnetic wave propagation and scattering from different kind of hydrometeors [5]. In this work, besides dielectric and geophysical properties of rain, ice particles and snowflakes, the scattering behaviors and attenuation effects are reviewed. The Mie scattering theory, the T-matrix approach, the spheroidal function expansion method, the Fredholm integral equation method, and the unimoment method were compared. It was stated that these methods give equally good results for the drops have size less than 3 mm and axial ratio less than 0.7, [5]. For the computation of the reflected power from the entire precipitation region was provided by the summation of backscattering cross sections for all hydrometeors.

Similar work has been done by many authors by using different single scattering models different hydrometeor geometries [4,29,30]. For instance, Aydin suggested using a two layer spheroid and performed the T-matrix solution to simulate scattering from water coated ice particles i.e. melting hail [31]. Straka mentioned that small ice crystals have a large variety of shapes and can be modelled as spheres, oblate spheroids, needles, dendrites, and bullet columns [6]. Regardless of the shape of hydrometeors, in these studies, the calculation of a scattered wave from the entire precipitation was given by the summation over the size distribution. Several size distributions i.e. Marshal Palmer, Laws and Parsons, Lognormal, or Gamma drop size distribution were developed [32,33,34.35]. The aim of using size distributions is to construct an empirical rain rate radar reflectivity relation. In this study, the number of scatterers embedded in each inhomogeneous layer in the VRT model is calculated by considered the Gamma drop size distribution developed by Ulbrich [34].

The traditional way for the calculation of the radar reflectivity factor is accomplished by summation over the size distribution which means only the first order scattered was considered and interaction between scatterers were ignored. This assumption holds for the light/medium precipitation rates since the size of the particles are small with respect to the wavelength i.e. Rayleigh approximation. However, for intense rain due to a denser medium and close range between scatterers, a multiple scattering effect may cause inaccurate estimation. That is the reason behind the models based on Rayleigh approximation. Models took into account independent scattering assumption should also be performed on the reflectivity correction algorithm to account for the attenuation, especially for long distances from the radar [36]. In the multiple layer VRT model, both the attenuation and multiple scattering effect are taken into account.

In Chapter.3, a multiple layered VRT model is applied for spaceborne remote sensing precipitation data, and both the Mie scattering theory and the T-matrix approach are used to construct volume scattering phase matrices for each infinitesimal layer by considering the rain type precipitation. In Chapter.4, a multiple layered VRT model is modified by considering the geometry of a ground based radar. Geophysical profile of the rain and snow precipitation is constructed for the calculation of the volume scattering phase matrices for each range interval. Radar beam area and range information is used to calculate reflectivities for each range unit and model validation is provided by Phase Tilt Weather Radar (PTWR) measurements. In Chapter.5, further model analyses are provided by considering different geophysical parameters for space borne and ground based remotely sensed data.

Chapter 2

Radiative Transfer Theory

Radiative transfer theory provides the means for energy transformation in terms of electromagnetic radiation. It describes interactions such as scattering, absorption and emission mathematically due to propagation of radiation through a medium with scatterers. The formulation of the radiative transfer equations was developed by Chandrasekhar [18]. The theory of radiative transfer was investigated for its application to the problem of scattering from an inhomogeneous layer with irregular boundaries by Ulaby [7,13], and it was extended and applied to the scattering from a multilayered inhomogeneous medium by Tjuatja [17]. In this section, the radiative transfer equations which govern the propagation of specific intensity through a medium and their solutions are presented for the sake of clarity and completeness of the dissertation.

The specific intensity $\boldsymbol{I}_\nu(\mathbf{r})$ with unit of $\mathrm{W\,m^{-2}\,sr^{-1}\,Hz^{-1}}$ is the fundamental quantity of the radiative transfer theory, and it is expressed in terms of the amount of power dP flowing in the $\hat{\mathbf{r}}$ direction within a solid angle $d\Omega$ over an unit area dA in a frequency interval $(v, v + dv)$ as follows:

$$dP = \boldsymbol{I}_\nu(\mathbf{r}) \cos\theta \, dA \, d\Omega \, dv \tag{2.1}$$

where θ is the angle between the outward normal $\hat{n}$ of the area dA and the unit vector $\hat{\mathbf{r}}$ [18,38]. Figure 2.1 shows the schematic of energy flow in terms of intensity defined in Equation (2.1).

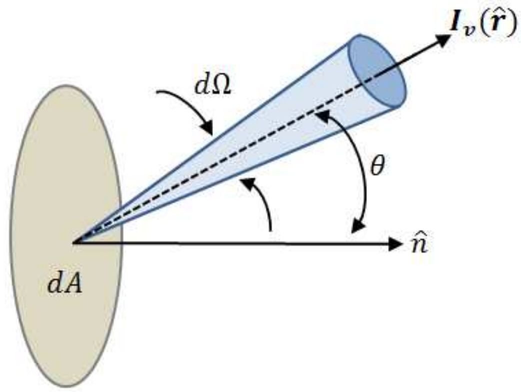

Figure 2-1 Schematic of energy flow in terms of intensity [18]

Since in most remote sensing applications, the single frequency radiation is commonly used, Equation (2.1) can be simplified by integrating $\boldsymbol{I_v}(\mathbf{r})$ over the frequency interval $(v - dv/2, v + dv/2)$ and the resulting equation is given as

$$dP = \boldsymbol{I}(\mathbf{r})\cos\theta \; dA \; d\Omega \tag{2.2}$$

Equation (2.2) is the abstract definition of the transfer equation which characterized all possible variations of intensities in a medium. To define the effect of these variations of the intensities in a medium which absorbs, emits, or scatters radiation, consider a specific intensity $\boldsymbol{I}(\mathbf{r},\hat{r})$ with the propagation direction of $\hat{r}$ incident upon an imaginary infinitesimal cylindrical volume that contains scatterers in a medium with unit length dr and cross section dA. Due to energy conservation, the possible changes in intensity $\boldsymbol{I}(\mathbf{r},\hat{r})$ can be absorption loss, scattering loss, absorption (thermal emission) or scattering in the direction of propagation. All these interactions are formulized as

$$d\boldsymbol{I}(\mathbf{r},\hat{r}) = -\boldsymbol{\kappa}_\mathbf{a}\boldsymbol{I}(\mathbf{r},\hat{r})\,dr - \boldsymbol{\kappa}_\mathbf{s}\boldsymbol{I}(\mathbf{r},\hat{r})\,dr + \boldsymbol{\kappa}_\mathbf{a}J_a\,dr + \boldsymbol{\kappa}_\mathbf{s}J_s\,dr \tag{2.3}$$

where $\boldsymbol{\kappa}_a$ and $\boldsymbol{\kappa}_s$ are the volume absorption and scattering coefficients. The decrease of the intensities in the direction of propagation over the length dr is due to absorption and scattering losses given by the first two terms on the right hand side. At the same time, the intensity is enhanced by the thermal emission and scattering of the intensities from the other directions to the direction of propagation which is represented by third and fourth terms and where J_a and J_s are the absorption and scattering source functions, respectively [17,38].

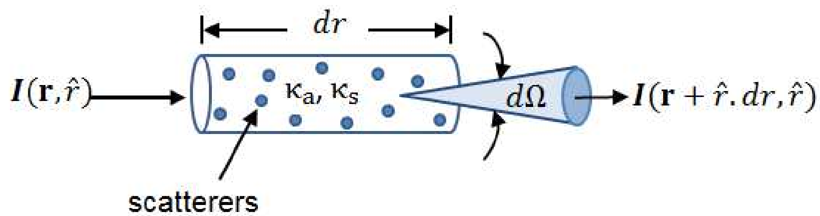

Figure 2-2 The change of intensity propagating in a cylindrical volume [38]

The definition of the scattering source function J_s in Equation (2.3) is given as

$$J_s(\theta_s,\varphi_s)=\frac{1}{4\pi}\int_0^{2\pi}\int_0^{\pi}P(\theta_s,\varphi_s;\theta,\varphi)\boldsymbol{I}(\theta,\varphi)\,d\theta d\varphi \tag{2.4}$$

where $P(\theta_s,\varphi_s;\theta,\varphi)$ is phase function which represents the relation between scattering intensities for all propagation directions and the scattering source function in the direction of propagation. From Equation (2.4), it is clear that J_s is a function of the propagating intensities. Unlike J_s , absorption source function, J_a is independent of incident intensity. It is related to temperature of the medium since under the condition of thermodynamic equilibrium, emission is equal to the absorption. Therefore, it is the source function in passive remote sensing problems. In radiative transfer theory, the intensities are defined by the Stokes parameters. For partially polarized electromagnetic wave, modified Stokes parameters are given in the following section.

2.1 Modified Stokes Parameter and Phase Matrix

2.1.1 Modified Stokes Parameters

An elliptically polarized monochromatic plane wave which is propagating through a differential solid angle $d\Omega$ in a medium with intrinsic impedance η can be written as

$$\mathbf{E} = \left(E_v \hat{\mathbf{v}} + E_h \hat{\mathbf{h}} \right) e^{\left(j\boldsymbol{k}.\boldsymbol{r} - jwt \right)} \tag{2.5}$$

where $\hat{\mathbf{v}}$ and $\hat{\mathbf{h}}$ are the unit vertical and horizontal polarization vectors and E_v and E_h are the vertical and horizontal incident field components respectively. The amplitude, phase and polarization state of an elliptically polarized wave can be completely characterized by modified Stokes parameters $\boldsymbol{I_v}$, $\boldsymbol{I_h}$, $\boldsymbol{U}$ and $\boldsymbol{V}$ which are expressed in the dimensions of intensity as follows [7]

$$\boldsymbol{I_v} d\Omega = \left\langle \left| E_v \right|^2 \right\rangle / \eta \tag{2.6}$$

$$\boldsymbol{I_h} d\Omega = \left\langle \left| E_h \right|^2 \right\rangle / \eta \tag{2.7}$$

$$\boldsymbol{U} d\Omega = 2 \ \mathrm{Re} \left\langle \left(E_v E_h^* \right) \right\rangle / \eta \tag{2.8}$$

$$\boldsymbol{V} d\Omega = 2 \ \mathrm{Im} \left\langle \left(E_v E_h^* \right) \right\rangle / \eta \tag{2.9}$$

where η is the intrinsic impedance of the medium Since the four Stokes parameters have the dimension of intensity, it is more convenient using them instead of phase or amplitude of a wave which have different dimensions.

2.1.2 Calculation of the Phase Matrix

The connection between the incident and scattering field components for the case of rough surface illumination by a plane wave is given by scattering matrix S as

$$\begin{bmatrix} E_v^s \\ E_h^s \end{bmatrix} = \frac{e^{ikR}}{R} \begin{bmatrix} S_{vv} & S_{vh} \\ S_{hv} & S_{hh} \end{bmatrix} \begin{bmatrix} E_v^i \\ E_h^i \end{bmatrix} \tag{2.10}$$

where E_v^s , E_h^s are scattered field components and E_v^i , E_h^i are incident field components polarized vertically and horizontally respectively. The scattering matrix components S_{pq} $(p, q = v \; or \; h)$ are the scattering amplitudes in meters, R is the distance from the center of the illuminated area to the observation point and k is the wave number.

To derive the Stokes parameters given by Equations (2.6) to (2.9) for the scattering wave in terms of scattering amplitudes and incident field components, the matrix relation states in Equation (2.10) is used. Then, the resulting equations are [7]

$$\left\langle \left| E_v^s \right|^2 \right\rangle / \eta = \Big\langle \Big[\left| S_{vv} \right|^2 \boldsymbol{I}_v^i + \left| S_{vh} \right|^2 \boldsymbol{I}_h^i$$

$$+ \mathrm{Re}\left(S_{vv} S_{vh}^* \right) \boldsymbol{U}^i - \mathrm{Im}\left(S_{vv} S_{vh}^* \right) \boldsymbol{V}^i \Big] \Big\rangle d\Omega / R^2 \tag{2.11}$$

$$\left\langle \left| E_h^s \right|^2 \right\rangle / \eta = \Big\langle \Big[\left| S_{hv} \right|^2 \boldsymbol{I}_v^i + \left| S_{hh} \right|^2 \boldsymbol{I}_h^i$$

$$+ \mathrm{Re}\left(S_{hv} S_{hh}^* \right) \boldsymbol{U}^i - \mathrm{Im}\left(S_{hv} S_{hh}^* \right) \boldsymbol{V}^i \Big] \Big\rangle d\Omega / R^2 \tag{2.12}$$

$$2 \; \mathrm{Re}\left\langle (E_v^s E_h^{s*}) \right\rangle / \eta = \Big\langle \Big[2\mathrm{Re}\left(S_{vv} S_{hv}^* \right) \boldsymbol{I}_v^i + 2\mathrm{Re}\left(S_{vh} S_{hh}^* \right) \boldsymbol{I}_h^i$$

$$+ \mathrm{Re}\left(S_{vv} S_{hh}^* + S_{vh} S_{hv}^* \right) \boldsymbol{U}^i - \mathrm{Im}\left(S_{vv} S_{hh}^* - S_{vh} S_{hv}^* \right) \boldsymbol{V}^i \Big] \Big\rangle d\Omega / R^2 \tag{2.13}$$

$$2 \left\langle \mathrm{Im}(E_v^s E_h^{s*}) \right\rangle / \eta = \Big\langle \Big[2\mathrm{Im}\left(S_{vv} S_{hv}^* \right) \boldsymbol{I}_v^i + 2\mathrm{Im}\left(S_{vh} S_{hh}^* \right) \boldsymbol{I}_h^i$$

$$+ \mathrm{Im}\left(S_{vv} S_{hh}^* + S_{vh} S_{hv}^* \right) \boldsymbol{U}^i + \mathrm{Re}\left(S_{vv} S_{hh}^* - S_{vh} S_{hv}^* \right) \boldsymbol{V}^i \Big] \Big\rangle d\Omega / R^2 \tag{2.14}$$

where the left hand sides relate the scattered wave in watts per meter square. To derive the intensity of the scattered wave, the above equations should be divided by the solid angle. Stokes parameters given by Equation (2.6) through (2.9) is for plane wave [17]. However, the scattering intensities are defined for spherical waves, and they differ from incident plane waves by $(A\cos\theta_s)/R^2$ at the observation point where θ_s is the angle between the scattered intensity direction and the normal of the area. Therefore, the Stokes parameters for scattered field are given by [17]

$$\boldsymbol{I}_v^s = R^2\left\langle\left|E_v^s\right|^2\right\rangle/\left(\eta A\cos(\theta_s)\right) = \left\langle\left[\left|S_{vv}\right|^2\boldsymbol{I}_v^i + \left|S_{vh}\right|^2\boldsymbol{I}_h^i\right.\right.$$

$$\left.\left.+\mathrm{Re}\left(S_{vv}S_{vh}^*\right)\boldsymbol{U}^i - \mathrm{Im}\left(S_{vv}S_{vh}^*\right)\boldsymbol{V}^i\right]\right\rangle d\Omega/\left(A\cos(\theta_s)\right) \tag{2.15}$$

$$\boldsymbol{I}_h^s = R^2\left\langle\left|E_h^s\right|^2\right\rangle/\left(\eta A\cos(\theta_s)\right) = \left\langle\left[\left|S_{hv}\right|^2\boldsymbol{I}_v^i + \left|S_{hh}\right|^2\boldsymbol{I}_h^i\right.\right.$$

$$\left.\left.+\mathrm{Re}\left(S_{hv}S_{hh}^*\right)\boldsymbol{U}^i - \mathrm{Im}\left(S_{hv}S_{hh}^*\right)\boldsymbol{V}^i\right]\right\rangle d\Omega/\left(A\cos(\theta_s)\right) \tag{2.16}$$

$$\boldsymbol{U}^s = 2\ \mathrm{Re}\left\langle(E_v^sE_h^{s*})\right\rangle/\left(\eta A\cos(\theta_s)\right) = \left\langle\left[2\mathrm{Re}\left(S_{vv}S_{hv}^*\right)\boldsymbol{I}_v^i + 2\mathrm{Re}\left(S_{vh}S_{hh}^*\right)\boldsymbol{I}_h^i\right.\right.$$

$$\left.\left.+\mathrm{Re}\left(S_{vv}S_{hh}^* + S_{vh}S_{hv}^*\right)\boldsymbol{U}^i - \mathrm{Im}\left(S_{vv}S_{hh}^* - S_{vh}S_{hv}^*\right)\boldsymbol{V}^i\right]\right\rangle d\Omega/\left(A\cos(\theta_s)\right) \tag{2.17}$$

$$\boldsymbol{V}^s = 2\left\langle\mathrm{Im}(E_v^sE_h^{s*})\right\rangle/\left(\eta A\cos(\theta_s)\right) = \left\langle\left[2\mathrm{Im}\left(S_{vv}S_{hv}^*\right)\boldsymbol{I}_v^i + 2\mathrm{Im}\left(S_{vh}S_{hh}^*\right)\boldsymbol{I}_h^i\right.\right.$$

$$\left.\left.+\mathrm{Im}\left(S_{vv}S_{hh}^* + S_{vh}S_{hv}^*\right)\boldsymbol{U}^i + \mathrm{Re}\left(S_{vv}S_{hh}^* - S_{vh}S_{hv}^*\right)\boldsymbol{V}^i\right]\right\rangle d\Omega/\left(A\cos(\theta_s)\right) \tag{2.18}$$

In Equation (2.15) through (2.18), the Stokes parameters for a scattering wave on the left hand side relate incident Stokes parameters by dimensionless quantity known as phase matrix [7]. If incident and scattering Stokes parameters are given by column vector $\boldsymbol{I}^i$ and $\boldsymbol{I}^s$, respectively, the phase $\boldsymbol{P}$ matrix can be expressed as

$$\boldsymbol{I}^s = \frac{1}{4\pi}\boldsymbol{P}\boldsymbol{I}^i d\Omega \tag{2.19}$$

For instance, from Equation (2.15), it can be seen that the element of the phase matrix relates $\boldsymbol{I}_v^s$ to $\boldsymbol{I}_v^i$ is $4\pi\left\langle \left|S_{vv}\right|^2 \right\rangle / (A\cos\theta_s)$ [17]. To consider all possible incident directions contributes scattering intensity $\boldsymbol{I}^s$ along scattering direction, phase matrix should be integrated over solid angle as

$$\boldsymbol{I}^s = \frac{1}{4\pi}\int_{4\pi}\boldsymbol{P}\boldsymbol{I}^i d\Omega \tag{2.20}$$

In Equation (2.19), $\boldsymbol{P}$ can be written in terms of Stokes matrix, $\mathbf{M}$ which is [17]

$$\boldsymbol{P} = 4\pi\langle\mathbf{M}\rangle / \left(A\ \cos\theta_s\right) \tag{2.21}$$

Since incident and scattered Stokes parameters $\boldsymbol{I}^i$ and $\boldsymbol{I}^s$ are 4 by 1 column vectors, from Equation (2.15) –(2.18) and Equation (2.19), it can be seen that $\mathbf{M}$ is a 4 by 4 matrix given by

$$\mathbf{M} = \begin{bmatrix} \left|S_{vv}\right|^2 & \left|S_{vh}\right|^2 & \mathrm{Re}\left(S_{vv}S_{vh}^*\right) & -\mathrm{Im}\left(S_{vv}S_{vh}^*\right) \\ \left|S_{hv}\right|^2 & \left|S_{hh}\right|^2 & \mathrm{Re}\left(S_{hv}S_{hh}^*\right) & -\mathrm{Im}\left(S_{hv}S_{hh}^*\right) \\ 2\mathrm{Re}\left(S_{vv}S_{hv}^*\right) & 2\mathrm{Re}\left(S_{vh}S_{hh}^*\right) & \mathrm{Re}\left(S_{vv}S_{hh}^* + S_{vh}S_{hv}^*\right) & -\mathrm{Im}\left(S_{vv}S_{hh}^* - S_{vh}S_{hv}^*\right) \\ 2\mathrm{Im}\left(S_{vv}S_{hv}^*\right) & 2\mathrm{Im}\left(S_{vh}S_{hh}^*\right) & \mathrm{Im}\left(S_{vv}S_{hh}^* + S_{vh}S_{hv}^*\right) & \mathrm{Re}\left(S_{vv}S_{hh}^* - S_{vh}S_{hv}^*\right) \end{bmatrix} \tag{2.22}$$

The phase matrix given by Equation (2.21) represents the relation between the incident and scattering intensities for one scatterer when a rough surface is illuminated by a plane wave. In the case of a homogeneous medium embedded with randomly positioned particles, the phase matrix is constructed by scattering and extinction cross sections of the particles [17]. Scattering cross section, Q_{sp} is defined as the hypothetical cross sectional area of the scatterer which intercepts the total amount of power actually scattered by the scatterer and extinction cross section, Q_{ep}, is given as the total cross section where power is scattered and absorbed by a scatterer due to incident Poynting vector with polarization p ($p = v$ or h). Therefore, Q_{sp} can be expressed for each scatterer as

$$Q_{sp}(\theta,\phi) = \frac{1}{4\pi}\int_{4\pi} \sigma_p d\Omega_s = \int_{4\pi} \left\langle \left|S_{vp}\right|^2 + \left|S_{hp}\right|^2 \right\rangle d\Omega_s, \tag{2.23}$$

where σ_p is the bistatic radar cross section due to a p-polarized ($p = v$ or h) incident intensity, and θ, ϕ are the angles of the incident direction. The volume-scattering coefficient of the inhomogeneous medium is given as

$$\boldsymbol{\kappa}_{sp} = N_v Q_{sp} \tag{2.24}$$

where N_v is the number of particles per unit volume. In Equation (2.24), $\boldsymbol{\kappa}_{sp}$ is the scattering coefficient defined by the scattering loss per unit length with the unit of $\mathrm{Np\ m^{-1}}$. Similarly, the absorption cross section for one particle and for the p-polarized incidence is defined as

$$\boldsymbol{\kappa}_{ap} = N_v Q_{ap} \tag{2.25}$$

and total cross section of a particle known as the extinction cross section is expressed as the summation of the scattering and absorption coefficients as follows

$$Q_{ep} = Q_{sp} + Q_{ap} \tag{2.26}$$

Similarly, the extinction coefficient is $\boldsymbol{\kappa}_{ep} = N_v Q_{ep}$. For a number of scatterer within the homogeneous volume, either Q_{ep} or Q_{sp} can be used in Equation (2.21) instead of the illuminated area by radar, $A cos\theta_s$, and, so the phase matrix can be stated as [17]

$$\boldsymbol{P}_s = 4\pi \boldsymbol{Q}_s^{-1} \left\langle \boldsymbol{M} \right\rangle \tag{2.27}$$

or

$$\boldsymbol{P}_e = 4\pi \boldsymbol{Q}_e^{-1} \left\langle \boldsymbol{M} \right\rangle \tag{2.28}$$

The phase matrix definition given by either Equation (2.27) or (2.28) can be chosen with respect to the source term [17].

2.2 Vector Radiative Transfer (VRT) Equations

By considering the definition of the phase matrix for a homogeneous medium embedded with randomly positioned particles, the radiative transfer equation for partially polarized waves is [7]

$$\frac{d\boldsymbol{I}}{dl} = -\boldsymbol{\kappa}_e \boldsymbol{I} + \frac{\boldsymbol{\kappa}_e}{4\pi} \int_{4\pi} \boldsymbol{P}_e \boldsymbol{I} d\Omega + \boldsymbol{\kappa}_a \boldsymbol{J}_a \tag{2.29}$$

or

$$\frac{d\boldsymbol{I}}{dl} = -\boldsymbol{\kappa}_e \boldsymbol{I} + \frac{\boldsymbol{\kappa}_s}{4\pi} \int_{4\pi} \boldsymbol{P}_s \boldsymbol{I} d\Omega + \boldsymbol{\kappa}_a \boldsymbol{J}_a \tag{2.30}$$

where $\boldsymbol{\kappa}_s$ and $\boldsymbol{\kappa}_e$ are the scattering and extinction cross sections respectively [17]. In the case of randomly positioned nonspherical particles or spherical particles, $\boldsymbol{\kappa}_s$ and $\boldsymbol{\kappa}_e$ becomes scalar and Equations (2.29) and (2.30) can be simplified as

$$\frac{d\boldsymbol{I}}{d\tau} = -\boldsymbol{I} + \frac{1}{4\pi} \int_{4\pi} \boldsymbol{P}_e \boldsymbol{I} d\Omega + (1\text{-}a) \boldsymbol{J}_a \tag{2.31}$$

and

$$\frac{d\boldsymbol{I}}{d\tau} = -\boldsymbol{I} + \frac{a}{4\pi} \int_{4\pi} \boldsymbol{P}_s \boldsymbol{I} d\Omega + (1\text{-}a) \boldsymbol{J}_a \tag{2.32}$$

where τ, the optical thickness, is defined as $\tau = \int \boldsymbol{\kappa}_e dl$ and a is the albedo defined as $a = \boldsymbol{\kappa}_s / \boldsymbol{\kappa}_e$.

The radiative transfer theory deals directly with the transport of energy through the medium which contains randomly distributed particles. Since it is assumed that there is no correlation between scattered fields from particles, as seen from Equation (2.31) and (2.32), theory holds the addition of the power but not scattered fields. As a result, the phase changing of the scattered wave is ignored [17,37]. Furthermore, since it is assumed that there is no correlation between scattered fields, the distance between scattered should be proper to apply the theory. There are various experimental studies focus on the applicability of the theory in terms of the spacing between scatterers [17]. Also, the dense medium radiative transfer theory is used to calculate the wave interaction between different particles by decomposed scattering field into coherent and an incoherent part [20,21]. Moreover, the well-known T-matrix approach for nonspherical scatterers or the Mie scattering calculation for closely packed spheres can be used inside the conventional radiative transfer theory to calculate volume phase scattering with included interaction between scatterers [37].

2.3 Scattering from an Inhomogeneous Layer with Irregular Boundaries

If a plane wave in the air is incident on an inhomogeneous layer which is above a ground surface, the scattering or reflection occurs at the boundary. Figure 2-3 shows the geometry of such a scattering problem [7,17].

In Figure 2-3, both incident and scattered intensities are needed to satisfy boundary condition. To solve this problem, it is necessary to split the intensity vector into *upward intensity* $\mathbf{I}^{+}$ and *downward intensity* $\mathbf{I}^{-}$ components [7,17]. Upward and downward intensities should satisfy the radiative transfer equation which is given by

$$\mu_s \frac{d\boldsymbol{I}^+(z,\mu_s,\varphi_s)}{dz} = -\boldsymbol{\kappa_e}\boldsymbol{I}^+(z,\mu_s,\varphi_s)$$

$$+\frac{1}{4\pi}\int_0^{2\pi}\int_0^1 \boldsymbol{\kappa_s}\boldsymbol{P_s}(\mu_s,\mu,\varphi_s-\varphi)\boldsymbol{I}^+(z,\mu,\varphi)\,d\mu d\varphi$$

$$+\frac{1}{4\pi}\int_0^{2\pi}\int_0^1 \boldsymbol{\kappa_s}\boldsymbol{P_s}(\mu_s,-\mu,\varphi_s-\varphi)\boldsymbol{I}^-(z,\mu,\varphi)\,d\mu d\varphi \quad (2.33)$$

$$\mu_s \frac{d\boldsymbol{I}^-(z,\mu_s,\varphi_s)}{dz} = +\boldsymbol{\kappa_e}\boldsymbol{I}^-(z,\mu_s,\varphi_s)$$

$$-\frac{1}{4\pi}\int_0^{2\pi}\int_0^1 \boldsymbol{\kappa_s}\boldsymbol{P_s}(-\mu_s,\mu,\varphi_s-\varphi)\boldsymbol{I}^+(z,\mu,\varphi)\,d\mu d\varphi$$

$$-\frac{1}{4\pi}\int_0^{2\pi}\int_0^1 \boldsymbol{\kappa_s}\boldsymbol{P_s}(-\mu_s,-\mu,\varphi_s-\varphi)\boldsymbol{I}^-(z,\mu,\varphi)\,d\mu d\varphi \quad (2.34)$$

where $\mu_s = \cos\theta_s$, $\mu = \cos\theta$; $\boldsymbol{I}^+$*and* $\boldsymbol{I}^-$ are column vectors containing the four Stokes parameters; $\boldsymbol{P_s}$ is the phase matrix, $\boldsymbol{\kappa_a}$ and $\boldsymbol{\kappa_s}$ are the absorption and scattering coefficient matrices, respectively; and the extinction coefficient is $\boldsymbol{\kappa_e} = \boldsymbol{\kappa_a} + \boldsymbol{\kappa_s}$. The first terms at the right hand side of the Equation (2.33) and (2.34) represent the lost due to absorption and scattering inside the layer. The second and third terms express the contribution of the upward and downward incident intensities to the upward and downward scattered intensities by the summation of the elements of the phase matrices over all the incident directions.

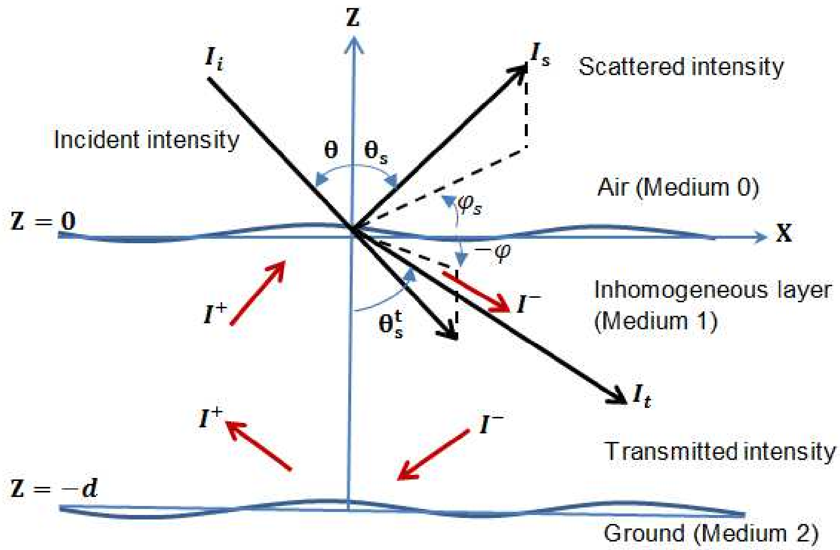

Figure 2-3 Scattering from an inhomogeneous layer [7]

To calculate the upward intensity due to an incident $\mathbf{I^i}$ which is

$$\mathbf{I^i} = \boldsymbol{I}_i \delta\left(\cos\theta - \cos\theta_i\right)\delta\left(\varphi - \varphi_i\right) \tag{2.35}$$

where , $\delta()$ is the Dirac delta function, and (θ_i, φ_i) is the direction of propagation of the incident wave. The VRT equations given by Equation (2.33) and (2.34) should be solved with respect to boundary conditions. At $z = -d$ the upward and downward intensities are related to through the ground scatter matrix $\mathbf{G}$ is

$$\mathbf{I}^+\left(-d, \mu_s, \varphi_s\right) = \frac{1}{4\pi}\int_0^{2\pi}\int_0^1 \mathbf{G}\left(\mu_s, \mu, \varphi_s - \varphi\right)\mathbf{I}^-\left(-d, \mu, \varphi\right) d\mu d\varphi \tag{2.36}$$

If the ground surface is plain, instead of $\mathbf{G}$, reflectivity matrix $\mathbf{R_g}$ can be used and it is given as

$$G = 4\pi\mathbf{R_g}\boldsymbol{\delta}\left(\mu_s - \mu\right)\boldsymbol{\delta}\left(\varphi_s - \varphi\right) \tag{2.37}$$

where $\mu = \cos\theta$. At the top boundary $z = 0$, surface-scattering and transmission-phase matrices $\mathbf{S_R}$ and $\mathbf{S_T}$ define the relation between upward and downward intensities as

$$\mathbf{I}^{-}\left(0,\mu_s,\varphi_s\right)=\frac{1}{4\pi}\int_0^{2\pi}\int_0^1 \mathbf{S_R}\left(\mu_s,\mu,\varphi_s-\varphi\right)\mathbf{I}^{+}\left(0,\mu,\varphi\right)d\mu d\varphi \tag{2.38}$$

$$+\frac{1}{4\pi}\int_0^{2\pi}\int_0^1 \mathbf{S_T}\left(\mu_s,\mu,\varphi_s-\varphi\right)\mathbf{I}^{i}\left(\mu,\varphi\right)d\mu d\varphi$$

After calculation of $\mathbf{I}^{+}(0,\mu_s,\varphi_s)$ within the inhomogeneous layer, the upward intensity transmitted from layer into the air can be determined by the forward-scattering matrix of the surface, $\mathbf{S_T}$, as;

$$\mathbf{I}^{+}\left(\mu_s,\varphi_s\right)=\frac{1}{4\pi}\int_0^{2\pi}\int_0^1 \mathbf{S_T}\left(\mu_s,\mu,\varphi_s-\varphi\right)\mathbf{I}^{+}\left(0,\mu,\varphi\right)d\mu d\varphi \tag{2.39}$$

The total scattering intensity in air $\mathbf{I}^{s}$ is given by the summation of two parts; the first part $\mathbf{I}^{+}(\mu_s,\varphi_s)$ is the intensity transferred from the layer to air and the second part $\mathbf{I}^{\boldsymbol{R}}$ is the intensity due to random surface scattering by the top layer boundary. The surface scattering matrices $\mathbf{S_R}$ and $\mathbf{S_T}$ can be calculated using surface scattering models.

The scattering coefficients are defined by the relation between incident and scattered intensities, and they are polarization depended. For instance, if the total scattered intensity for a p-polarized component is $\boldsymbol{I_p^s}$, the scattering coefficient for this component is defined relative to the incident intensity $\boldsymbol{I_q^i}$ of polarization q, and the scattering coefficient σ_{pq}^0 is defined as

$$\sigma_{pq}^0 = 4\pi\cos\theta_s \boldsymbol{I_p^s} \,/\, \boldsymbol{I_q^i} \tag{2.40}$$

Although there is no closed form analytical solution for VRT equations given by Equation (2.33) and (2.34), they can be solved exactly by using numerical techniques. One of these numerical techniques is the matrix doubling method explained in the following section.

2.4 Solution of VRT Equations by Matrix Doubling Method

In 1963, Hulst showed that the multiple scattering solution of parallel planes of atmosphere can be obtained by a doubling process, if a multiple scattering solution for one single layer is known [22]. Since then, doubling method has been investigated by many authors in various forms, mostly for computing multiple scattering effects in the atmosphere [23,24]. It has been improved by including the effect of plane layer boundaries and emission computations from a scattering layer without boundaries. Moreover, the method was generalized by taking into account irregular boundary and dense medium effects for small scatterers by Fung and Eom [39]. Besides, Tjuatja considered a multilayer inhomogeneous medium with irregular interfaces that consisted of sublayers with different physical properties and so, extended the model to include vertical variations and multilayer effects [17]. This method provides an alternative way to the radiative transfer method to calculate the effect of surface and volume scattering. It is based on the energy balance like radiative transfer method, and it has been shown by an equivalent formulation to the radiative transfer approach. It relies on ray tracing to describe the scattering process, and sums up all the scattered rays in a given direction like a geometric series. If an irregular inhomogeneous layer given by Figure 2-4 is considered, the relation between scattered and incident intensity is

$$\boldsymbol{I}^s\left(\theta_s,\varphi_s\right)=\frac{1}{4\pi}\int_{4\pi}\boldsymbol{S}_{T1}\left(\theta_s,\theta;\varphi_s-\varphi\right)\boldsymbol{I}^i\left(\theta,\varphi\right)d\Omega \tag{2.41}$$

where $\boldsymbol{S}_{T1}\left(\theta_s,\theta;\varphi_s-\varphi\right)$ is the total scattering phase matrix of the irregular layer. $\boldsymbol{S}_{T1}$ involves the volume and surface scattering as long as boundary-volume interactions and multiple scattering effects inside the layer. Therefore, it can be derived from the volume scattering phase matrix for an infinitesimal layer and surface phase matrix that characterizes the medium boundary interactions.

Let the single-scattering phase matrix represented by $\boldsymbol{P}(\theta_s, \theta, \varphi_s - \varphi)$. Then for the infinitesimal thin layer of optical depth $\Delta\tau$, the multiple-scattering phase matrices in the backward direction ***S*** and forward direction ***T*** are related to $\boldsymbol{P}$ as follows

$$\boldsymbol{S}\left(\theta_s, \theta, \varphi_s - \varphi\right) = a\,\boldsymbol{U}^{-1}\ \boldsymbol{P}\left(\theta_s, \pi-\theta, \varphi_s, \varphi\right)\Delta\tau \tag{2.42}$$

$$\boldsymbol{T}\left(\theta_t, \theta, \varphi_t - \varphi\right) = a\,\boldsymbol{U}^{-1}\ \boldsymbol{P}\left(\pi-\theta_t, \pi-\theta, \varphi_t - \varphi\right)\Delta\tau \tag{2.43}$$

When the incidence direction is reversed, a similar set of forward and backward multiple-scattering phase matrices can be defined for infinitesimal layer as follows

$$\boldsymbol{S}^*\left(\theta_s, \theta, \varphi_s - \varphi\right) = a\,\boldsymbol{U}^{-1}\ \boldsymbol{P}\left(\pi-\theta_s, \theta, \varphi_s - \varphi\right)\Delta\tau \tag{2.44}$$

$$\boldsymbol{T}^*\left(\theta_t, \theta, \varphi_t - \varphi\right) = a\,\boldsymbol{U}^{-1}\ \boldsymbol{P}\left(\theta_t, \theta, \varphi_t - \varphi\right)\Delta\tau \tag{2.45}$$

where ***U*** is the diagonal matrix containing the directional cosines of the scattered angle and a is the single-scattering albedo of the medium. ***S, T, S**** and ***T**** are shown in Fig.2-5.

In the case of two adjacent layers, as illustrated in Figure 2-6, the first layer of thickness $\Delta\tau_1$ characterized by $\boldsymbol{S_1}, \boldsymbol{T_1}, \boldsymbol{S_1^*}$ and $\boldsymbol{T_1^*}$ can be combined with another layer of thickness $\Delta\tau_2$ characterized by $\boldsymbol{S_2}, \boldsymbol{T_2}, \boldsymbol{S_2^*}$ and $\boldsymbol{T_2^*}$ to form a layer of thickness $\Delta\tau_1 + \Delta\tau_2$ characterized by ***S, T, S**** and ***T**** as follows;

$$\boldsymbol{S} = \boldsymbol{S_1} + \boldsymbol{T_1^*}\boldsymbol{S_2}\boldsymbol{T_1} + \boldsymbol{T_1^*}\boldsymbol{S_2}\boldsymbol{S_1^*}\boldsymbol{S_2}\boldsymbol{T_1} + \ldots = \boldsymbol{S}_1 + \boldsymbol{T_1^*}\boldsymbol{S_2}\left(1-\boldsymbol{S_1^*}\boldsymbol{S_2}\right)^{-1}\boldsymbol{T_1} \tag{2.46}$$

$$\boldsymbol{T} = \boldsymbol{T_2}\left[1+\boldsymbol{S_1^*}\boldsymbol{S_2} + \left(\boldsymbol{S_1^*}\boldsymbol{S_2}\right)^2 + \ldots\right]\boldsymbol{T_1} = \boldsymbol{T_2}\left(1-\boldsymbol{S_1^*}\boldsymbol{S_2}\right)^{-1}\boldsymbol{T_1} \tag{2.47}$$

$$\boldsymbol{S}^* = \boldsymbol{S_1^*} + \boldsymbol{T_1^*}\boldsymbol{S_2^*}\left(1-\boldsymbol{S_1^*}\boldsymbol{S_2}\right)^{-1}\boldsymbol{T_1^*} \tag{2.48}$$

$$\boldsymbol{T}^* = \boldsymbol{T_2^*}(1-\boldsymbol{S_1}\boldsymbol{S_2^*})^{-1}\boldsymbol{T_1^*} \tag{2.49}$$

where **1** represents the identity matrix. The superscript asterisk is used to indicate scattering phase matrices for incidence in +Z direction.

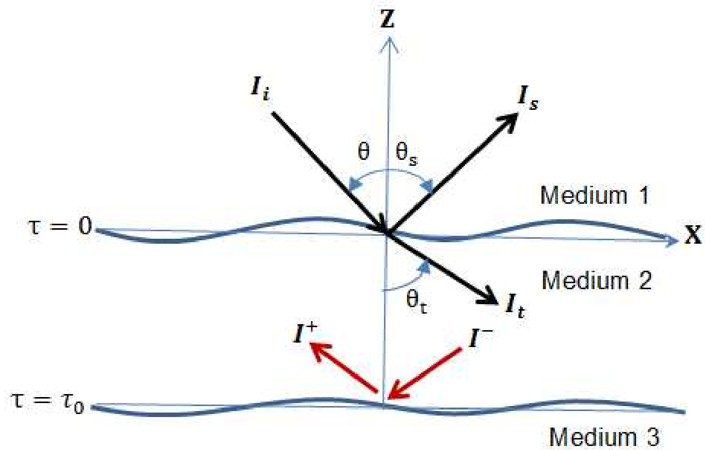

(a)

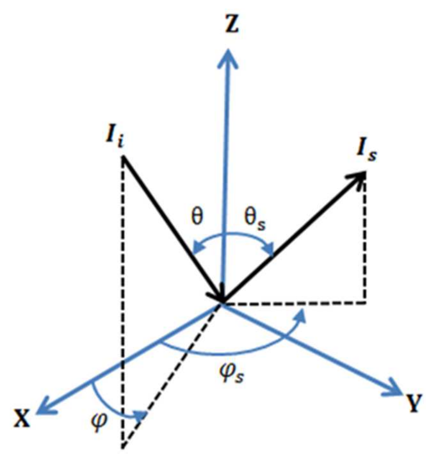

(b)

Figure 2-4 (a) Geometry of scattering from an irregular inhomogeneous layer, (b) The coordinate system [17]

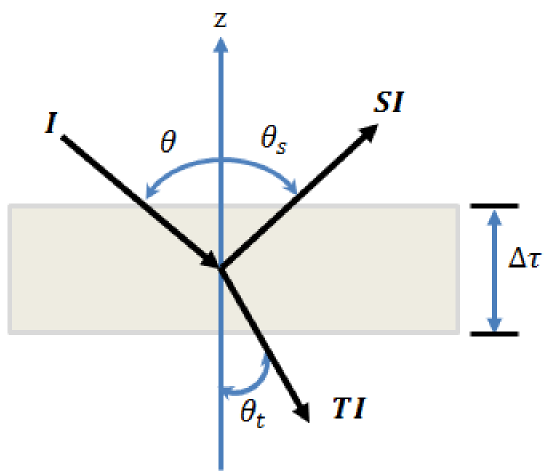

(a)

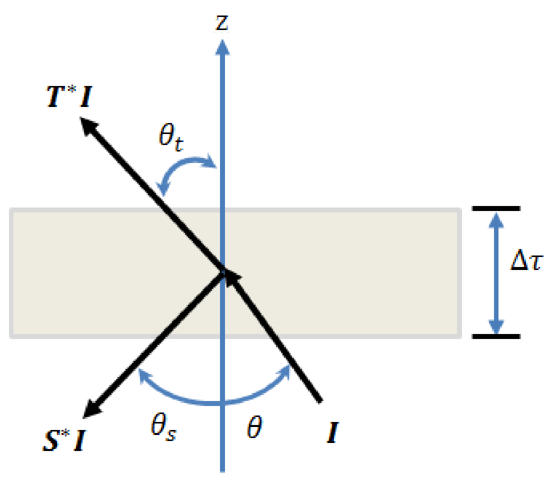

(b)

Figure 2-5 (a) Backward and forward scattering from the thin layer for downward incidence, (b) for upward incidence [7,17]

By repeating the process given in the Equations (2.46) through (2.49), the phase matrices for a layer of any desired thickness may be obtained. When the incident wave $\boldsymbol{I}$

goes through the layer, the single scattering phase matrix $\boldsymbol{T}$ in the forward direction consists of two parts; direct and diffuse component. Therefore, $\boldsymbol{T}$ can be expressed as

$$\boldsymbol{T} = \boldsymbol{E} + \boldsymbol{F} \tag{2.50}$$

where $\boldsymbol{E}$ is the extinction matrix and its diagonal elements are $exp(-\Delta\tau/\mu_i)$,where μ_i is the directional cosine [17].

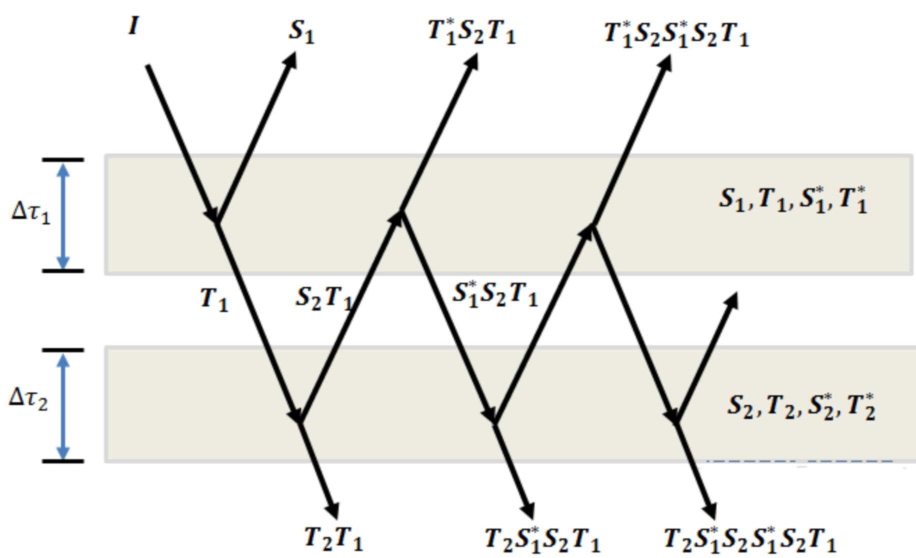

Figure 2-6 The scattering process for two adjacent layers [17]

2.5 Conversion to Fourier Components and Harmonic Phase Matrices

To solve the VRT equations, the integrals in the Equation (2.33) and (2.34) should be converted in to matrix product. To do that, the azimuthal dependence incident and scattering polar angles is needed to eliminate. This can be accomplished by expanding incident and scattering intensities in terms of Fourier series. Therefore, in the analysis calculations are simplified dealing with one Fourier component at one time. Hence,

$$\boldsymbol{I}(\theta,\varphi)=\sum_{m=0}\left[\boldsymbol{I}_a^m(\theta)\cos m\varphi+\boldsymbol{I}_b^m(\theta)\sin m\varphi\right] \tag{2.51}$$

$$\boldsymbol{I_s}(\theta_s,\varphi_s)=\sum_{m=0}\left[\boldsymbol{I}_{as}^m(\theta_s)\cos m\varphi_s+\boldsymbol{I}_{bs}^m(\theta_s)\sin m\varphi_s\right] \tag{2.52}$$

where the superscript m donates the m^{th} Fourier coefficients [7]. Similarly, backward and forward scattering phase matrices expanded in Fourier series can be written as

$$\boldsymbol{S}(\theta_s,\theta,\varphi_s-\varphi)=\sum_{m=0}\left[\boldsymbol{S}_a^m(\theta_s,\theta)\cos m(\varphi_s-\varphi)\right.$$
$$\left.+\boldsymbol{S}_b^m(\theta_s,\theta)\sin m(\varphi_s-\varphi)\right] \tag{2.53}$$

$$\boldsymbol{T}(\theta_s,\theta,\varphi_s-\varphi)=\sum_{m=0}\left[\boldsymbol{T}_a^m(\theta_s,\theta)\cos m(\varphi_s-\varphi)\right.$$
$$\left.+\boldsymbol{T}_b^m(\theta_s,\theta)\sin m(\varphi_s-\varphi)\right] \tag{2.54}$$

Doubling equations for two adjacent layer given by Equations (2.46) through (2.49) can be expressed by expanding of the Fourier coefficients and so, the harmonic multiple scattering phase matrices are given by [7]

$$\bar{\boldsymbol{S}}^m=\bar{\boldsymbol{S}}_1^m+\bar{\boldsymbol{T}}_{t1}^{m*}\bar{\boldsymbol{S}}_2^m\left(\boldsymbol{I}-f_m^2\bar{\boldsymbol{S}}_1^{m*}\bar{\boldsymbol{S}}_2^m\right)^{-1}\bar{\boldsymbol{T}}_1^m \tag{2.55}$$

$$\bar{\boldsymbol{T}}^m=\bar{\boldsymbol{T}}_2^m\left(\boldsymbol{I}-f_m^2\bar{\boldsymbol{S}}_1^{m*}\bar{\boldsymbol{S}}_2^m\right)^{-1}\bar{\boldsymbol{T}}_1^m \tag{2.56}$$

$$\bar{\boldsymbol{S}}^{m*}=\bar{\boldsymbol{S}}_1^{m*}+\bar{\boldsymbol{T}}_1^m\bar{\boldsymbol{S}}_2^{m*}\left(\boldsymbol{I}-f_m^2\bar{\boldsymbol{S}}_1^m\bar{\boldsymbol{S}}_2^{m*}\right)^{-1}\bar{\boldsymbol{T}}_{t1}^{m*} \tag{2.57}$$

$$\bar{\boldsymbol{T}}^{m*}=\bar{\boldsymbol{T}}_2^{m*}\left(\boldsymbol{I}-f_m^2\bar{\boldsymbol{S}}_1^m\bar{\boldsymbol{S}}_2^{m*}\right)^{-1}\bar{\boldsymbol{T}}_1^{m*} \tag{2.58}$$

where

$$\bar{\boldsymbol{S}}^m = \begin{bmatrix} \boldsymbol{S}_a^m & -\boldsymbol{S}_b^m \\ \boldsymbol{S}_b^m & \boldsymbol{S}_a^m \end{bmatrix}$$

$$\bar{\boldsymbol{T}}^m = f_m \begin{bmatrix} \boldsymbol{F}_a^m & -\boldsymbol{F}_b^m \\ \boldsymbol{F}_b^m & \boldsymbol{F}_a^m \end{bmatrix} + \begin{bmatrix} \boldsymbol{E} & 0 \\ 0 & \boldsymbol{E} \end{bmatrix}$$

$$f_m = \begin{cases} 1/2 & m = 0 \\ 1/4 & m > 0 \end{cases}$$

where $\boldsymbol{E}$ is the extinction matrix taken to be diagonal for isotropic media. Its diagonal elements are $\exp(-\Delta\tau/\mu_i)$, where μ_i is the directional cosine [7]. To include the full polarization effect $\boldsymbol{S}_a^m$, $\boldsymbol{S}_b^m$, $\boldsymbol{T}_a^m$ and $\boldsymbol{T}_b^m$ should be 4×4 matrices corresponding to the four stokes parameters. Hence in general, $\bar{\boldsymbol{S}}^m$ and $\bar{\boldsymbol{T}}^m$ becomes 8×8 matrix .

To calculation multiple scattering phase matrices N –incident and scattered polar angles are chosen. Hence, $\boldsymbol{S}_{apq}^m$, $\boldsymbol{S}_{bpq}^m$, $\boldsymbol{T}_{apq}^m$ and $\boldsymbol{T}_{bpq}^m$ are $4N \times 4N$ matrices while $\bar{\boldsymbol{S}}^m$ and $\bar{\boldsymbol{T}}^m$ are $8N \times 8N$.Since the integrations in the Radiative Transfer equations are evaluated numerically, Gaussian Quadrature method is used to calculate directional cosine μ as the integration variable [7]. Therefore, the scattering phase matrix for a specific i^{th} incident and jth scattering angle given by $s_{\alpha pq}^m$ the element of $\boldsymbol{S}_{\alpha pq}^m$ is

$$s_{\alpha pq}^m\left(\mu_i, \mu_j\right) = \omega \boldsymbol{S}_{\alpha pq}^m\left(\mu_i, \mu_j\right) \frac{\Delta\tau}{\mu_i} w_j \tag{2.59}$$

where the subscript α denotes either a or b , μ_i and μ_j are the Gaussian quadrature zeros, w_j is the weight at μ_j with $1 < i, j < N$. The, $t_{\alpha pq}^m$ the element of $\boldsymbol{T}_{\alpha pq}^m$ can be expressed as,

$$t_{\alpha pq}^m\left(\mu_i, \mu_j\right) = \omega \boldsymbol{T}_{\alpha pq}^m\left(\mu_i, \mu_j\right) \frac{\Delta\tau}{\mu_i} w_j \tag{2.60}$$

and the extinction matrix $\boldsymbol{E}$ can be expressed

$$\boldsymbol{E}_{pq}^{m}(\mu_i, \mu_j) = \delta(\mu_i, \mu_j)\exp(\frac{-\Delta\tau}{\mu_i}) \tag{2.61}$$

where $\delta()$ is the Kronecker delta function.

2.6 Boundary Medium Interactions and Surface Phase Matrix

When one attempts modelling the wave scattering from natural terrain, generally it is expected to combine surface and volume scattering as well as the boundary medium interactions. The theoretical calculation of rough surface scattering plays an important role in interpreting the backscattering data especially from sea or land surfaces. The roughness of the mediums and discontinuities over the boundary between two media is effective for defining scattering characteristics. In the past, several surface scattering models were studied.

Among these models, the Kirchhoff rough surface scattered model and Small Perturbation model can be applicable when the surface is either rough or smooth enough on the scale of the wavelength. On the other hand, the Integral Equation Model (IEM) proposed by Fung based on a more rigorous solution and verified by laboratory measurements of bistatic scattering coefficients of surfaces have small, intermediate and large scale roughness [16]. The single scattering bistatic scattering coefficients for the IEM model was summarized by Tjuatja and it was stated that IEM model is valid for continues surfaces of arbitrary roughness with rms slope less than 0.4 [17].

Since the radiative transfer equation is solved by considering the matrix doubling method, the boundary medium interaction is determined using the ray tracing technique. In this section surface scattering phase matrix and boundary interaction between homogeneous and inhomogeneous interface is explained.

Scattering intensity due to a rough surface is related with the incident intensity as

$$\boldsymbol{I}^s\left(\theta_s,\varphi_s\right)=\frac{1}{4\pi}\int_0^{2\pi}\int_0^{\pi/2}\left[\frac{\sigma^{\mathrm{o}}\left(\theta_s,\theta;\varphi_s-\varphi\right)}{\cos\theta_s}\right]\boldsymbol{I}\left(\theta,\varphi\right)\sin\theta d\theta d\varphi \tag{2.62}$$

where the quantity inside the bracket is defined as the phase function. By considering the Fourier expansion of the phase function and intensities, the azimuth dependence of Eq.(2.62) can be eliminated. Then, it can be expressed in Fourier component form as

$$\boldsymbol{I}^{sm}\left(\theta_s\right)=f_m\int_0^{\pi/2}\left[\frac{\sigma^m\left(\theta_s,\theta\right)}{\cos\theta_s}\right]\boldsymbol{I}^m\left(\theta\right)\sin\theta d\theta \tag{2.63}$$

By applying an *N*-point Gaussian quadrature technique and calculate the scattered intensities in *N* directions as given in Section 2.5, the following equation is obtained

$$\boldsymbol{I}^{sm}=f_m\Gamma^m\boldsymbol{I}^m, \qquad f_m=\begin{cases}1/2 & m=0\\ 1/4 & m>0\end{cases} \tag{2.64}$$

where Γ^m is a $4N\times4N$ matrix that consists of Fourier coefficients, and $\boldsymbol{I}^{sm}$ and $\boldsymbol{I}^m$ are $4N$ columns vectors. Note that the surface phase matrix Γ^m can be expressed as either the surface reflection phase matrix $\boldsymbol{R}_{ij}^m$ or the surface transmission phase matrix $\boldsymbol{Q}_{ij}^m$ with respect to θ_s as given follow

$$\Gamma^m=\begin{cases}\boldsymbol{R}_{ij}^m & ,\theta_s\le 90^\circ\\ \boldsymbol{Q}_{ij}^m & ,\theta_s\le 90^\circ\end{cases}=\frac{\sigma^m\left(\theta_s,\theta\right)}{\cos\theta_s}, \tag{2.65}$$

Consider the case where the scattering of incident intensity from the interface between the homogeneous upper half space and inhomogeneous lower half-space as depicted in Figure 2-7. If the incident intensity in medium 1 impinges upon medium 2, as seen from Figure 2-7(a), the effective reflection and transmission phase matrices, $\hat{\boldsymbol{R}}_{12}$ and $\hat{\boldsymbol{Q}}_{21}$, are given by

$$\hat{\boldsymbol{R}}_{12}=\boldsymbol{R}_{12}+\boldsymbol{Q}_{12}\boldsymbol{S}_2\left(\boldsymbol{I}-\boldsymbol{R}_{21}\boldsymbol{S}_2\right)^{-1}\boldsymbol{Q}_{21} \tag{2.66}$$

$$\widehat{\boldsymbol{Q}}_{21} = \left(\boldsymbol{I} - \boldsymbol{R}_{21}\boldsymbol{S}_{2}\right)^{-1} \boldsymbol{Q}_{21} \tag{2.67}$$

When the direction of the incident intensity is reversed as given in Figure 2-7(b), the effective reflection and transmission phase matrices, $\widehat{\boldsymbol{R}}_{21}$ and $\widehat{\boldsymbol{Q}}_{12}$, are given by

$$\widehat{\boldsymbol{R}}_{21} = \boldsymbol{R}_{21}\left(\boldsymbol{I} - \boldsymbol{S}_{2}\boldsymbol{R}_{21}\right)^{-1} \tag{2.68}$$

$$\widehat{\boldsymbol{Q}}_{12} = \boldsymbol{Q}_{12}\left(\boldsymbol{I} - \boldsymbol{S}_{2}\boldsymbol{R}_{21}\right)^{-1} \tag{2.69}$$

When the upper half-space is homogeneous and the lower half-space is inhomogeneous, effective reflection and transmission phase matrices are expanded in Fourier series as

$$\widehat{\boldsymbol{R}}_{12}^{\boldsymbol{m}} = \boldsymbol{R}_{12}^{\boldsymbol{m}} + f_m^2 \boldsymbol{Q}_{12}^{\boldsymbol{m}} \overline{\boldsymbol{S}}_2^{\boldsymbol{m}} \left(\boldsymbol{I} - f_m^2 \boldsymbol{R}_{12}^{\boldsymbol{m}} \overline{\boldsymbol{S}}_{12}^{\boldsymbol{m}}\right)^{-1} \boldsymbol{Q}_{21}^{\boldsymbol{m}} \tag{2.70}$$

$$\widehat{\boldsymbol{Q}}_{21}^{\boldsymbol{m}} = \left(\boldsymbol{I} - f_m^2 \boldsymbol{R}_{21}^{\boldsymbol{m}} \overline{\boldsymbol{S}}_2^{\boldsymbol{m}}\right)^{-1} \boldsymbol{Q}_{21}^{\boldsymbol{m}} \tag{2.71}$$

$$\widehat{\boldsymbol{R}}_{21}^{\boldsymbol{m}} = \boldsymbol{R}_{21}^{\boldsymbol{m}} \left(\boldsymbol{I} - f_m^2 \overline{\boldsymbol{S}}_2^{\boldsymbol{m}} \boldsymbol{R}_{21}^{\boldsymbol{m}}\right)^{-1} \tag{2.72}$$

$$\widehat{\boldsymbol{Q}}_{12}^{\boldsymbol{m}} = \boldsymbol{Q}_{12}^{\boldsymbol{m}} \left(\boldsymbol{I} - f_m^2 \overline{\boldsymbol{S}}_2^{\boldsymbol{m}} \boldsymbol{R}_{21}^{\boldsymbol{m}}\right)^{-1} \tag{2.73}$$

Similarly, when the upper half-space is inhomogeneous and lower half-space is homogeneous as given in Figure 2-8, the effective reflection and transmission phase matrices can be expended in Fourier series as

$$\tilde{\boldsymbol{R}}_{12}^{\boldsymbol{m}} = \boldsymbol{R}_{12}^{\boldsymbol{m}} \left(\boldsymbol{I} - f_m^2 \overline{\boldsymbol{S}}_1^{\boldsymbol{m}*} \boldsymbol{R}_{12}^{\boldsymbol{m}}\right)^{-1} \tag{2.74}$$

$$\tilde{\boldsymbol{Q}}_{21}^{\boldsymbol{m}} = \boldsymbol{Q}_{21}^{\boldsymbol{m}} \left(\boldsymbol{I} - f_m^2 \overline{\boldsymbol{S}}_1^{\boldsymbol{m}*} \boldsymbol{R}_{12}^{\boldsymbol{m}}\right)^{-1} \tag{2.75}$$

$$\tilde{\boldsymbol{R}}_{21}^{\boldsymbol{m}} = \boldsymbol{R}_{21}^{\boldsymbol{m}} + f_m^2 \boldsymbol{Q}_{21}^{\boldsymbol{m}} \overline{\boldsymbol{S}}_1^{\boldsymbol{m}*} \left(\boldsymbol{I} - f_m^2 \boldsymbol{R}_{12}^{\boldsymbol{m}} \overline{\boldsymbol{S}}_1^{\boldsymbol{m}*}\right)^{-1} \boldsymbol{Q}_{12}^{\boldsymbol{m}} \tag{2.76}$$

$$\tilde{\boldsymbol{Q}}_{12}^{\boldsymbol{m}} = \left(\boldsymbol{I} - f_m^2 \boldsymbol{R}_{12}^{\boldsymbol{m}} \overline{\boldsymbol{S}}_1^{\boldsymbol{m}*}\right)^{-1} \boldsymbol{Q}_{12}^{\boldsymbol{m}} \tag{2.77}$$

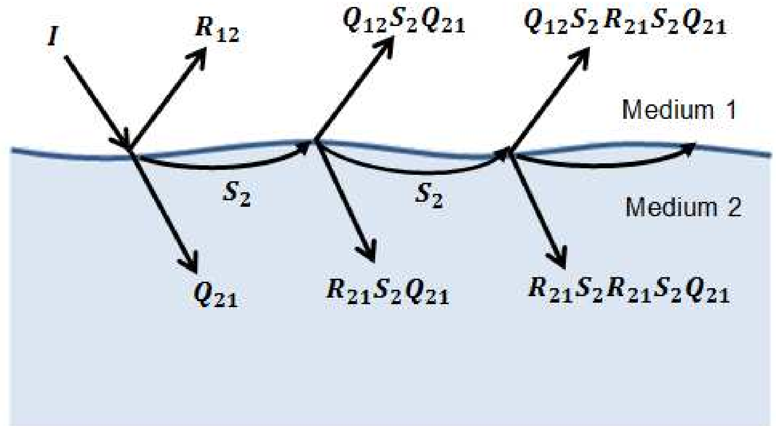

(a)

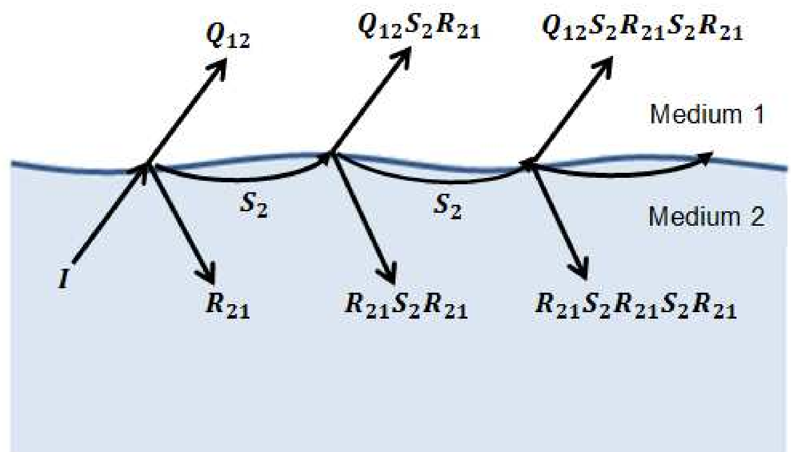

(b)

Figure 2-7 The scattering process at the interface between homogeneous upper half-space and inhomogeneous lower half space due to (a) downward incidence and (b) upward incidence. $\mathbf{S}_2$ is the backward scattering phase matrix of medium 2 for downward (-Z) incidence [17].

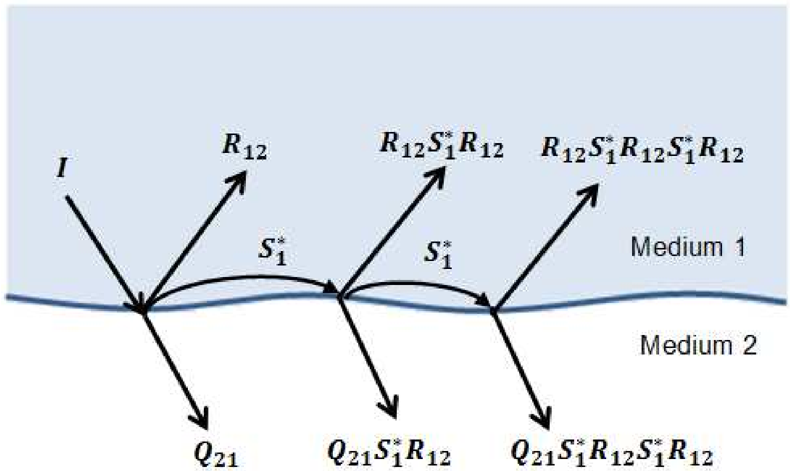

(a)

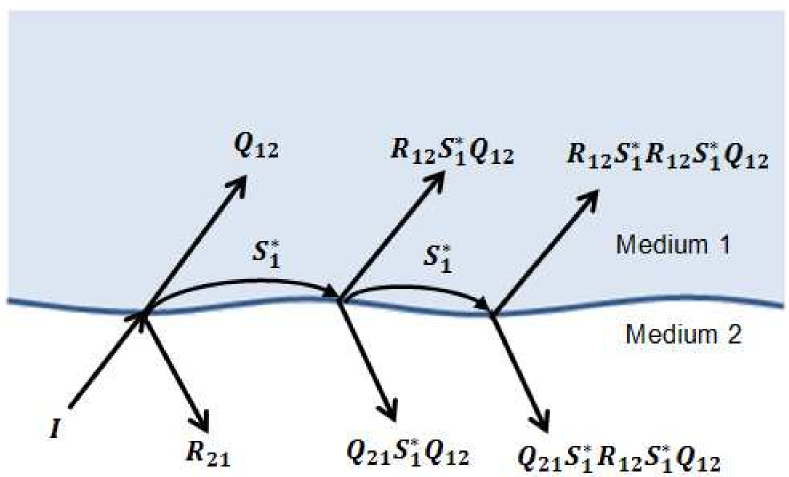

(b)

Figure 2-8 The scattering process at the interface between inhomogeneous upper half-space and homogeneous lower half space due to (a) downward incidence and (b) upward incidence. $\mathbf{S}_1^*$ is the backward scattering phase matrix of medium 1 for upward (+Z) incidence [17]

By considering the inhomogeneous medium which is characterized by backward volume-scattering phase matrices $\boldsymbol{S}$ and $\boldsymbol{S}^*$, and forward volume-scattering phase matrices $\boldsymbol{T}$ and $\boldsymbol{T}^*$ the total reflection and transmission scattering phase matrices $\boldsymbol{S}_{T1}$ and $\boldsymbol{T}_{T1}$ can be derived by using the ray tracing method (see Figure 2.9);

$$\boldsymbol{S}_{T1} = \hat{\boldsymbol{R}}_{12} + \hat{\boldsymbol{Q}}_{12}\left(\boldsymbol{I} - \boldsymbol{T}^*\tilde{\boldsymbol{R}}_{23}\boldsymbol{T}\hat{\boldsymbol{R}}_{23}\right)^{-1}\boldsymbol{T}^*\tilde{\boldsymbol{R}}_{23}\boldsymbol{T}\hat{\boldsymbol{Q}}_{21} \tag{2.78}$$

$$\boldsymbol{T}_{T1} = \tilde{\boldsymbol{Q}}_{32}\left(\boldsymbol{I} - \boldsymbol{T}\hat{\boldsymbol{R}}_{21}\boldsymbol{T}^*\tilde{\boldsymbol{R}}_{23}\right)^{-1}\boldsymbol{T}^*\hat{\boldsymbol{Q}}_{21} \tag{2.79}$$

The Fourier components of $\boldsymbol{S}_{T1}$ and $\boldsymbol{T}_{T1}$ are

$$\boldsymbol{S}_{T1}^{\boldsymbol{m}} = \hat{\boldsymbol{R}}_{12}^{\boldsymbol{m}} + f_m^2\hat{\boldsymbol{Q}}_{12}^{\boldsymbol{m}}\left(\boldsymbol{I} - f_m^2\bar{\boldsymbol{T}}^{m*}\tilde{\boldsymbol{R}}_{23}^{\boldsymbol{m}}\bar{\boldsymbol{T}}^{m}\hat{\boldsymbol{R}}_{21}^{\boldsymbol{m}}\right)^{-1}\bar{\boldsymbol{T}}^{m*}\tilde{\boldsymbol{R}}_{23}^{\boldsymbol{m}}\bar{\boldsymbol{T}}^{m}\hat{\boldsymbol{Q}}_{21}^{\boldsymbol{m}} \tag{2.80}$$

$$\boldsymbol{T}_{T1}^{\boldsymbol{m}} = f_m^2\tilde{\boldsymbol{Q}}_{32}^{\boldsymbol{m}}\left(\boldsymbol{I} - f_m^2\bar{\boldsymbol{T}}^{m}\hat{\boldsymbol{R}}_{21}^{\boldsymbol{m}}\bar{\boldsymbol{T}}^{m*}\tilde{\boldsymbol{R}}_{23}^{\boldsymbol{m}}\right)^{-1}\bar{\boldsymbol{T}}^{m}\hat{\boldsymbol{Q}}_{21}^{\boldsymbol{m}} \tag{2.81}$$

After applying the matrix doubling method, the total scattering matrix from an irregular inhomogeneous layer is related incident and scattering intensities as

$$\boldsymbol{I}^{sm} = f_m\boldsymbol{S}_T^m\boldsymbol{I}^m \tag{2.82}$$

The harmonic scattering coefficient of the irregular layer can be derived from Eq. (2.82) and (2.63) as follows

$$\sigma_{\alpha pq}^m\left(\theta_i,\theta_j\right) = 4\pi\cos\theta_i\left[\boldsymbol{S}_{T1}^m\left(\theta_i,\theta_j\right)\right]_{\alpha pq} \tag{2.83}$$

where p and q represent the incident and scattered wave directions, α can be either cosine or sine series coefficient. Finally, the total harmonic scattering coefficient of the irregular inhomogeneous layer is expressed as

$$\sigma_{pq}^{\circ}\left(\theta_i,\theta_j;\varphi_s-\varphi\right) = \sum_{m=0}^{\infty}4\pi\cos\theta_i\left[\left[\boldsymbol{S}_{T1}^m\left(\theta_i,\theta_j\right)\right]_{\alpha pq}\cos m\left(\varphi_s-\varphi\right)\right.$$

$$+\left[\boldsymbol{S}_{T1}^{m}\left(\theta_i,\theta_j\right)\right]_{bpq} \sin m\left(\varphi_s-\varphi\right)\Big] \tag{2.84}$$

In the case of Rayleigh or Mie medium with isotropic rough boundaries, its total scattering given by [14,17]

$$\sigma^{\circ}_{pq}\left(\theta_i,\theta_j;\varphi_s-\varphi\right)=\sum_{m=0}^{\infty}4\pi\cos\theta_i\left[\boldsymbol{S}_{T1}^{m}\left(\theta_i,\theta_j\right)\right]_{\alpha pq}\cos m\left(\varphi_s-\varphi\right) \tag{2.85}$$

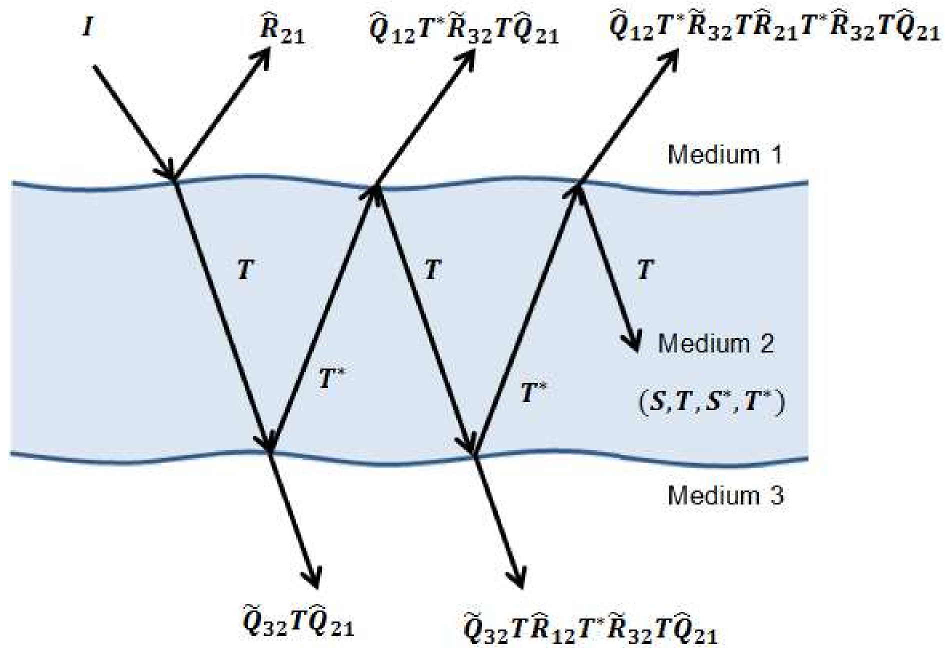

Figure 2-9 The scattering process due to an inhomogeneous layer with irregular boundaries. Medium 2 characterized by the volume scattering phase matrices $\boldsymbol{S}$, $\boldsymbol{T}$, $\boldsymbol{S}^*$, and $\boldsymbol{T}^*$ [17]

2.7 Solution of VRT Equations for Multilayered Inhomogeneous Medium

From Section 2.4 through 2.6, the solution of the radiative transfer equations for two adjacent layers is provided by the doubling method, and boundary medium interactions are explained. The solution of the vector radiative transfer model for an N –layered inhomogeneous medium was derived by Tjuatja which is summarized here [17].

To calculate the total backscattered phase matrix $\boldsymbol{S}_{TN}$ from the N –layered inhomogeneous medium, which is depicted in Figure 2-10, the first step is calculation of the backward and forward volume scattering phase matrices which are $\boldsymbol{S}_i$, $\boldsymbol{T}_i$, $\boldsymbol{S}_i^*$ and $\boldsymbol{T}_i^*$,where $1 \le i \le N$. Then, surface reflection and transmission phase matrices; $\boldsymbol{R}_{ji}$ and $\boldsymbol{Q}_{ji}$, where $1 \le j,i \le N$, for all of the interfaces between two half spaces are computed as described in Section 2.6. Therefore, by starting with the first layer, the total reflection phase matrix for the N layer medium is given by $\boldsymbol{R}_N^T$, where it is assumed that $(N-1)^{th}$ layer is a half-space above the N^{th} layer. By applying Eq. (2.77) to the N –layered inhomogeneous medium, $\boldsymbol{R}_N^T$ can be written as

$$\boldsymbol{R}_N^T = \boldsymbol{R}_{N-1,N} + \boldsymbol{Q}_{N-1,N} \left(\boldsymbol{I} - \boldsymbol{T}_N^* \boldsymbol{R}_{N,N+1} \boldsymbol{T}_N \boldsymbol{R}_{N,N-1} \right)^{-1} \boldsymbol{T}_N^* \boldsymbol{R}_{N,N+1} \boldsymbol{T}_N \boldsymbol{Q}_{N,N-1} \qquad (2.86)$$

Note that, $\boldsymbol{R}_N^T$ is a function of volume and surface phase matrices; therefore, it accounts for the volume scattering effect as well as the boundary–layer interactions. The total reflection phase matrix, $\boldsymbol{R}_{N-1}^T$, for the $N-1$ layered inhomogeneous medium is constructed by considering the upper half-space is the $N-2$ layer and the lower half-space is the N layer [17]. Therefore, since $\boldsymbol{R}_N^T$ is known from Eq. (2.86), the $\boldsymbol{R}_{N-1}^T$ is given by

$$\boldsymbol{R}_{N-1}^T = \boldsymbol{R}_{N-2,N-1} + \boldsymbol{Q}_{N-2,N-1}\left(\boldsymbol{I} - \boldsymbol{T}_{N-1}^{*}\boldsymbol{R}_N^T\boldsymbol{T}_{N-1}\boldsymbol{R}_{N-1,N-2}\right)^{-1}$$

$$\boldsymbol{T}_{N-1}^{*}\boldsymbol{R}_N^T\boldsymbol{T}_{N-1}\boldsymbol{Q}_{N-1,N-2} \tag{2.87}$$

If one continues to apply Eq. (2.86) from the $(N-2)^{th}$ layer up to the 1^{st} layer, the total reflected scattering phase matrix for the N layered inhomogeneous medium $\boldsymbol{S}_{TN}$ is

$$\boldsymbol{S}_{TN} = \boldsymbol{R}_1^T = \boldsymbol{R}_{0,1} + \boldsymbol{Q}_{0,1}\left(\boldsymbol{I} - \boldsymbol{T}_1^{*}\boldsymbol{R}_2^T\boldsymbol{T}_1\boldsymbol{R}_{1,0}\right)^{-1}\boldsymbol{T}_1^{*}\boldsymbol{R}_2^T\boldsymbol{T}_1\boldsymbol{Q}_{1,0} \tag{2.88}$$

and its Fourier transformation is written as [17]

$$\boldsymbol{S}_{TN}^m = \hat{\boldsymbol{R}}_{01}^m + f_m^2\hat{\boldsymbol{Q}}_{0,1}^m\left(\boldsymbol{I} - f_m^2\overline{\boldsymbol{T}}_1^{m*}\boldsymbol{R}_2^{Tm}\overline{\boldsymbol{T}}_1^m\hat{\boldsymbol{R}}_{1,0}^m\right)^{-1}\overline{\boldsymbol{T}}_1^{m*}\boldsymbol{R}_2^{Tm}\overline{\boldsymbol{T}}_1^m\hat{\boldsymbol{Q}}_{1,0}^m \tag{2.89}$$

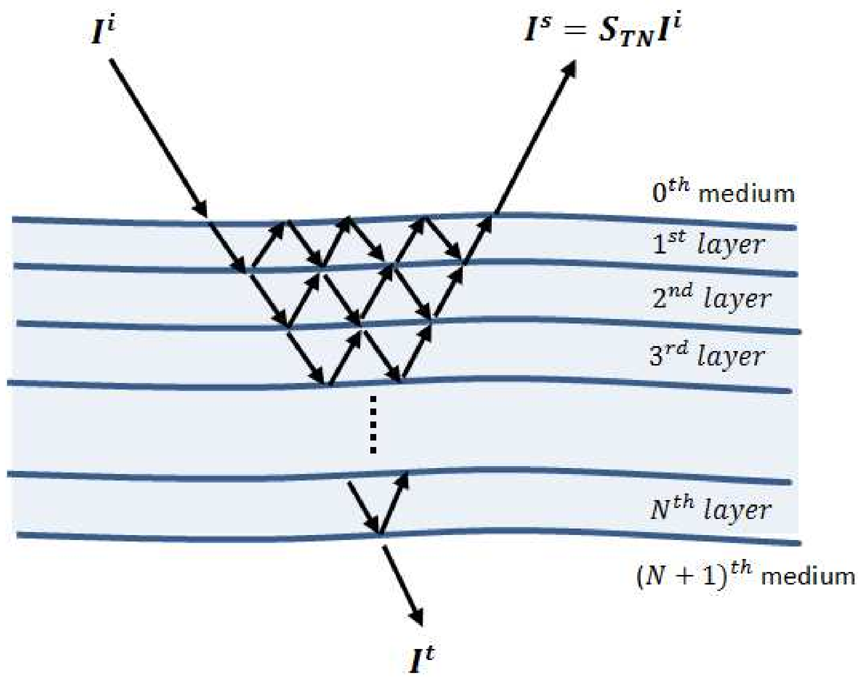

Figure 2-10 The illustration of scattering process through N –layered inhomogeneous medium [17]

2.8 Volume Scattering Phase Matrix

When an electromagnetic wave incident upon an inhomogeneous layer with irregular boundaries, surface scattering occurs due to boundary discontinuities and volume scattering generated due to inhomogeneities inside the layer. Therefore, the total scattering from a layer should be a function which involves boundary medium interactions as well as the surface and volume scattering phase matrices as described in Section 2.7. In the radiative transfer formulation, the relation between the incident and scattered intensities is given by the volume scattering phase matrix of the inhomogeneous layer. In most of the previous studies, the Mie scattering or T-matrix approach was performed by using the Rayleigh phase matrix approximation [28,30,40]. In these studies, it was assumed that the size of the scatterers is small with respect to wavelength, and the scatterer volume fraction was low. This assumption implies that the distance between scatterers is far and it can be applicable when the medium is sparse. For densely populated media, the modified Mie phase matrix was developed to take into account the effect of close spacing between spherical scatterers [37,39,41]. However, the restriction of the modified Mie phase matrix calculation is that it is valid for the spherical scatterers.

On the other hand, the phase matrix calculation can be carried out using the T-matrix approach for axially symmetric non-spherical scatterers. This is needed for the calculation of the scattering from the hydrometeors especially for those that have diameter larger than 1 mm. However, in the conventional T-matrix method, which is introduced by Waterman [27] and recently refined by Mishchenko [28], only independent scattering is considered so, the distance between scatterers are assumed to be far enough to ignore the phase interference effect between scatterers [40]. Therefore, the better way is to use the T-matrix approach instead of Mie scattering for the calculation of the expansion coefficients of the vector spherical harmonic functions to account both sphere or spheroid type scatterers. Then, the approximate distance between scatterers is considered in the derivation of the volume scattering phase matrix for a closely packed medium.

The modified Mie scattering phase matrix calculation is explained in the Section 2.8.1. The T-matrix approach which is substituted into the phase matrix calculation for densely populated medium is introduced in Section 2.8.2.

2.8.1 Mie Scattering Theory

Mie Scattering theory was developed by Gustav Mie in 1908 to calculate absorption and scattering by a sphere with arbitrary radius and refractive index. The geometry of the scattering problem by one single sphere is depicted in Figure 2-11 where the time-harmonic incident plane wave propagates along the z -axis, and the sphere has a radius a with relative dielectric permittivity, $\varepsilon_r = \varepsilon' + j\varepsilon''$. Also, it has been assumed that the permeability of the sphere and medium are the same and given by the symbol μ.

When the incident plane wave is x-polarized, then the electric and magnetic field components are given by

$$\mathbf{E}^i = \hat{x}\mathbf{E}_0 \mathrm{e}^{jkz} \tag{2.90}$$

$$\mathbf{H}^i = \hat{y}\frac{\mathbf{E}_0}{\eta} \mathrm{e}^{jkz} \tag{2.91}$$

where the time factor $e^{-j\omega t}$ is suppressed, the wave number is $k = \omega\sqrt{\mu\varepsilon}$ and the wave impedance is $\eta = \sqrt{\mu/\varepsilon}$ .According to Maxwell's Equations, the time-harmonic electromagnetic field $(\boldsymbol{E}, \boldsymbol{H})$ in a linear, isotropic, homogeneous medium must satisfy the wave equation

$$\nabla^2\mathbf{E} + \mathrm{k}^2\mathbf{E} = 0 \qquad \nabla^2\mathbf{H} + \mathrm{k}^2\mathbf{H} = 0 \tag{2.92}$$

where $k^2 = \omega^2 \varepsilon\mu$. $\boldsymbol{E}$ and $\boldsymbol{H}$ fields are assumed divergence free

$$\nabla.\mathbf{E} = 0 \qquad\qquad \nabla.\mathbf{H} = 0 \tag{2.93}$$

and they are not independent

$$\nabla\times\mathbf{E} = j\omega\mu\mathbf{H} \qquad\qquad \nabla\times\mathbf{H} = -j\omega\varepsilon\mathbf{E} \tag{2.94}$$

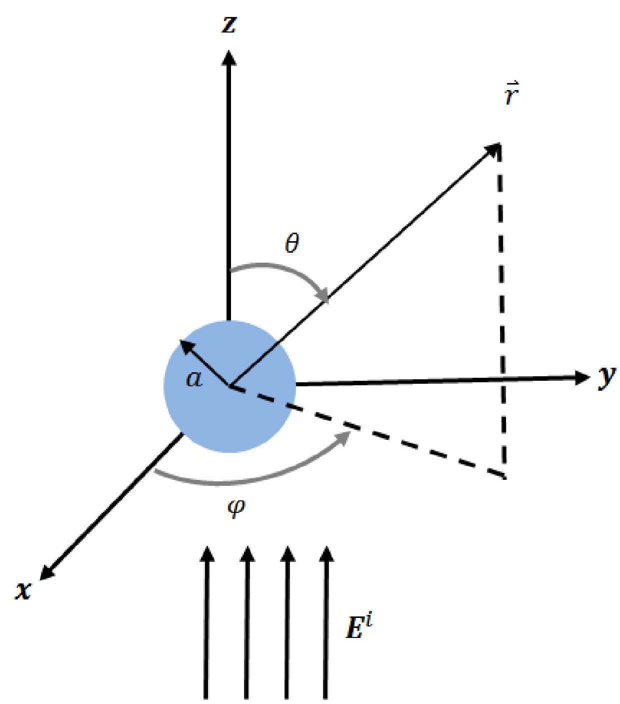

Figure 2-11 Scattering geometry in spherical coordinates centered on a sphere [25]

To calculate the scattered field from a sphere, a particular solution of the wave equation in spherical coordinates is needed. By using the separation of variables, the solution of the vector wave equation is provided by vector spherical harmonics $\mathbf{M}$ and $\mathbf{N}$ which have zero divergence, the curl of $\mathbf{M}$ is proportional to $\mathbf{N}$ and the curl of $\mathbf{N}$ is proportional to $\mathbf{M}$ given as [25]

$$\mathbf{M}_{emn} = \hat{\theta}\frac{-m}{\sin\theta}\sin m\varphi P_n^m(\cos\theta)z_n(\rho) - \hat{\varphi}\cos m\varphi\frac{dP_n^m}{d\theta}z_n(\rho)$$

$$\mathbf{M}_{omn} = \hat{\theta}\frac{m}{\sin\theta}\cos m\varphi P_n^m(\cos\theta)z_n(\rho) - \hat{\varphi}\sin m\varphi\frac{dP_n^m(\cos\theta)}{d\theta}z_n(\rho)$$

$$\mathbf{N}_{emn} = \hat{r}\frac{z_n(\rho)}{\rho}\cos m\varphi n(n+1)P_n^m(\cos\theta) + \hat{\theta}\cos m\varphi\frac{dP_n^m(\cos\theta)}{d\theta}\frac{1}{\rho}\frac{d}{d\rho}[\rho z_n(\rho)]$$

$$-\hat{\varphi}m\sin m\varphi\frac{P_n^m(\cos\theta)}{\sin\theta}\frac{1}{\rho}\frac{d}{d\rho}[\rho z_n(\rho)]$$

$$\mathbf{N}_{omn} = \hat{r}\frac{z_n(\rho)}{\rho}\sin m\varphi n(n+1)P_n^m(\cos\theta) + \hat{\theta}\sin m\varphi\frac{dP_n^m(\cos\theta)}{d\theta}\frac{1}{\rho}\frac{d}{d\rho}[\rho z_n(\rho)]$$

$$-\hat{\varphi}m\cos m\varphi\frac{P_n^m(\cos\theta)}{\sin\theta}\frac{1}{\rho}\frac{d}{d\rho}[\rho z_n(\rho)] \qquad (2.95)$$

where the subscripts o and e denote odd and even parts of vector spherical harmonics $\mathbf{M}$ and $\mathbf{N}$, $P_n^m(\cos\theta)$ is the Legendre functions of the first kind of degree n and order m, ρ is the size parameter i.e. $\rho = ka$ and $z_n(\rho)$ is the spherical Bessel functions [25]. The derivative of the Bessel function is calculated by recurrence relations.

By converting the plane wave coordinates to the spherical coordinates and considering the expansion of the incident field in spherical harmonics the scattered fields due to the sphere are

$$\mathbf{E}^s = \mathbf{E}_0\sum_{n=1}^{\infty} j^n\frac{(2n+1)}{n(n+1)}\left(-\mathbf{B}_n\mathbf{M}_{o1n}^{(3)} + j\mathbf{A}_n\mathbf{N}_{e1n}^{(3)}\right)$$

$$\mathbf{H}^s = \frac{\mathbf{E}_0}{\eta}\sum_{n=1}^{\infty} j^n\frac{(2n+1)}{n(n+1)}\left(\mathbf{A}_n\mathbf{M}_{e1n}^{(3)} + j\mathbf{B}_n\mathbf{N}_{o1n}^{(3)}\right) \qquad (2.96)$$

where the superscript, (3), appended to the vector spherical harmonics, denotes the spherical Bessel function of the third kind, also called Henkel function, denoted as $h_n^{(1)}$.

The Henkel function is the function of the radial dependence, and used instead of $z_n(\rho)$ in Eq. (2.95). Therefore, the vector spherical harmonic can be rearranged by considering $h_n^{(1)}$, order m as 1 and size parameter ρ as kr given by

$$\mathbf{M}_{e1n}^{(3)} = -\hat{\theta} h_n^{(1)}(kr)\sin\varphi \frac{P_n^1(\cos\theta)}{\sin\theta} - \hat{\varphi} h_n^{(1)}(kr)\cos\varphi \frac{dP_n^1(\cos\theta)}{d\theta}$$

$$\mathbf{M}_{o1n}^{(3)} = \hat{\theta} h_n^{(1)}(kr)\cos\varphi \frac{P_n^1(\cos\theta)}{\sin\theta} - \hat{\varphi} h_n^{(1)}(kr)\sin\varphi \frac{dP_n^1(\cos\theta)}{d\theta}$$

$$\mathbf{N}_{e1n}^{(3)} = \hat{r}\frac{n(n+1)}{kr} h_n^{(1)}(kr)\cos\varphi P_n^1(\cos\theta) + \hat{\theta}\frac{1}{kr}\frac{d}{d(kr)}\left[krh_n^{(1)}(kr)\right]\cos\varphi \frac{dP_n^1(\cos\theta)}{d\theta}$$

$$-\hat{\varphi}\frac{1}{kr}\frac{d}{d(kr)}\left[krh_n^{(1)}(kr)\right]\sin\varphi \frac{P_n^1(\cos\theta)}{\sin\theta}$$

$$\mathbf{N}_{o1n}^{(3)} = \hat{r}\frac{n(n+1)}{kr} h_n^{(1)}(kr)\sin\varphi P_n^1(\cos\theta) + \hat{\theta}\frac{1}{kr}\frac{d}{d(kr)}\left[krh_n^{(1)}(kr)\right]\sin\varphi \frac{dP_n^1(\cos\theta)}{d\theta}$$

$$-\hat{\varphi}\frac{1}{kr}\frac{d}{d(kr)}\left[krh_n^{(1)}(kr)\right]\cos\varphi \frac{P_n^1(\cos\theta)}{\sin\theta} \tag{2.97}$$

where r is the range from the center of the sphere [17]. Besides spherical vector harmonic functions $\mathbf{M}^{(3)}$ and $\mathbf{N}^{(3)}$, Mie coefficients, $\mathbf{A}_n$ and $\mathbf{B}_n$ should be known to calculate the scattering field given by Eq.(2.96). After incident, internal and scattering electric and magnetic fields are expanded in the vector spherical harmonics, by using the boundary condition for both theta and phi components of electric fields at the surface of the sphere, Mie coefficients, $\mathbf{A}_n$ and $\mathbf{B}_n$ are derived as

$$\mathbf{A}_n = \frac{m\Psi_n(mx)\Psi_n'(x) - \Psi_n(x)\Psi_n'(mx)}{m\Psi_n(mx)\zeta_n'(x) - \zeta_n(x)\Psi_n'(mx)} \tag{2.98}$$

$$\mathbf{B}_n = \frac{\Psi_n(mx)\Psi_n^{'}(x) - m\Psi_n(x)\Psi_n^{'}(mx)}{\Psi_n(mx)\zeta_n^{'}(x) - m\zeta_n(x)\Psi_n^{'}(mx)} \tag{2.99}$$

where the size parameter x is $x = ka$ and the relative refractive index m is $m = M_1 / M$ where M_1 and M are the refractive indices of particle and medium, respectively [17]. Since the surrounding medium is air, m can be simplified as $m = \sqrt{\varepsilon_r}$. In Eq. (2.98) and (2.99), the Ricatti Bessel functions Ψ_n and ζ_n are related to Bessel function j_n of the first kind and Bessel function $h_n^{(1)}$ of the third kind as

$$\Psi_n(\rho) = \rho j_n(\rho), \qquad \text{and} \qquad \zeta_n(\rho) = \rho h_n^{(1)}(\rho) \tag{2.100}$$

where ρ can be either mx or x as given in Eq.(2.98) and (2.99). By using spherical vector harmonic functions $\mathbf{M}^{(3)}$ and $\mathbf{N}^{(3)}$, the spherical vector functions are defined as functions of incident and scattering angles, the distance between scatterers, but the Mie coefficients are directly related to the size and relative permittivity of the sphere. Due to the small size of the scatterers in the microwave region, the Rayleigh approximation holds, and the spherical harmonics converge rapidly. Hence, the first two terms are needed to construct scattered electric and magnetic fields given in Eq.(2.96). The corresponding terms of the spherical vector wave functions are given in Tjuatja [17]. To construct the phase matrix, coordinate transformation is needed since the scattering field is calculated in the vertical (v) and horizontal (h) directions in Cartesian coordinates, whereas the incident field is decomposed in polar coordinates using spherical vector functions. The detailed description of coordinate transformation for v and h coordinates is given by Fung and Eom [19]. The phase matrix related to the first two Stokes parameters is constructed from the scattering field as [19,17]

$$\mathbf{P}_s = \frac{4\pi r^2 \eta n_o}{\boldsymbol{\kappa}_s |\mathbf{E}_0|^2} \mathrm{Re}\begin{bmatrix} \left(\mathbf{E}_v^s \mathbf{H}_h^{s*}\right)_{v-inc} & \left(\mathbf{E}_v^s \mathbf{H}_h^{s*}\right)_{h-inc} \\ \left(-\mathbf{E}_h^s \mathbf{H}_v^{s*}\right)_{v-inc} & \left(-\mathbf{E}_h^s \mathbf{H}_v^{s*}\right)_{h-inc} \end{bmatrix} \tag{2.101}$$

where $\boldsymbol{\kappa}_s$ is the effective volume scattering coefficient and n_o is the scatterer number density. The approximate distance between scatterers, r is related to the volume fraction of the scatterers v_f as [17]

$$r = \left(\frac{v_o}{v_f}\right)^{1/3} \tag{2.102}$$

where $v_o = (4/3)\pi a^3$. The extinction cross section, Q_e, and the scattering cross section, Q_s, of a sphere are calculated by using Mie coefficients as [25]

$$Q_e = \frac{2\pi}{k^2}\sum_{n=1}^{\infty}(2n+1)\mathrm{Re}(\mathbf{A}_n + \mathbf{B}_n) \tag{2.103}$$

$$Q_s = \frac{2\pi}{k^2}\sum_{n=1}^{\infty}(2n+1)\left(|\mathbf{A}_n|^2 + |\mathbf{B}_n|^2\right) \tag{2.104}$$

where k is the propagation constant in the host medium. For an inhomogeneous medium which contains randomly distributed scatterers such as snowfall or rainfall, dense layer effective permittivity can be calculated using empirical formulas or can be known from measurements. If the number of the particles is n_0, the volume extinction coefficient, $\boldsymbol{\kappa}_\mathbf{e}$ and the volume scattering coefficient, $\boldsymbol{\kappa}_\mathbf{s}$ for the infinitesimally thin dense medium is calculated as

$$\boldsymbol{\kappa}_\mathbf{e} = n_0 Q_e, \qquad \boldsymbol{\kappa}_\mathbf{s} = n_0 Q_s \tag{2.105}$$

2.8.2 T-matrix Approach

The T-matrix approach, also known as the extended boundary condition method, is a technique based on the Huygens principles to calculate the electromagnetic scattered field from axially symmetric non-spherical particles. It was introduced by Waterman [27] and today, the T-matrix approach seems to be widely used. It is a powerful tool for solving light scattering problems for nonspherical but axially symmetric particles with sizes not too large with respect to the wavelength [40,42,43,44]. For the computation of electromagnetic scattering by homogeneous, rotationally symmetric nonspherical particles, free public access to the T-matrix codes written in Fortran-77 is available at http://www.giss.nasa.gov. Like the Mie scattering calculation, in the T-matrix approach, the incident and scattered waves are expanded in vector spherical harmonics to calculate light scattering by a medium that contains independently scattering nonspherical particles.

By using x-polarized incident plane wave given in Eqs.(2.90) and (2.91), incident and scattered electric fields are expanded in vector spherical harmonics as follows

$$\mathbf{E^i}(\mathbf{r}) = \sum_{n=1}^{\infty}\sum_{m=-n}^{n}[a_{mn}\mathbf{RgM_{mn}}(k\mathbf{r}) + b_{mn}\mathbf{RgN_{mn}}(k\mathbf{r})] \tag{2.106}$$

$$\mathbf{E^s}(\mathbf{r}) = \sum_{n=1}^{\infty}\sum_{m=-n}^{n}\left[p_{mn}\mathbf{M}_{mn}(k\mathbf{r}) + q_{mn}\mathbf{N}_{mn}(k\mathbf{r})\right] \tag{2.107}$$

where k is the wave number of the surrounding medium and $\mathbf{r}$ is the distance from the center of the scatterer [28]. From the solution of vector Helmholtz equation, vector spherical harmonics; $\mathbf{RgM_{mn}}$, $\mathbf{RgN_{mn}}$, $\mathbf{M_{mn}}$ and $\mathbf{N_{mn}}$ are defined as follows [28]

$$\begin{matrix}\mathbf{M}_{mn}(k\boldsymbol{r},\theta,\varphi) \\ \mathbf{RgM}_{mn}(k\boldsymbol{r},\theta,\varphi)\end{matrix} = \gamma_{mn}\begin{matrix}h_n^{(1)}(kr) \\ j_n(kr)\end{matrix}\mathbf{C}_{mn}(\theta,\varphi) \tag{2.108}$$

$$\begin{matrix}\mathbf{N}_{mn}(k\boldsymbol{r},\theta,\varphi)\\ \mathbf{Rg}\mathbf{N}_{mn}(k\boldsymbol{r},\theta,\varphi)\end{matrix}=\gamma_{mn}\left(\frac{n(n+1)}{kr}\begin{matrix}h_n^{(1)}(kr)\\ j_n(kr)\end{matrix}\mathbf{P}_{mn}(\theta,\varphi)\right.$$

$$\left.+\frac{1}{kr}\frac{d}{d(kr)}\left(kr\begin{matrix}h_n^{(1)}(kr)\\ j_n(kr)\end{matrix}\right)\mathbf{B}_{mn}(\theta,\varphi)\right) \tag{2.109}$$

where j_n and $h_n^{(1)}$ are the first and third kind of Bessel functions and functions γ_{mn}, $\mathbf{C}_{mn}$, $\mathbf{B}_{mn}$ and $\mathbf{P}_{mn}$ are

$$\gamma_{mn}=\left[\frac{(2n+1)(n-m)!}{4\pi n(n+1)(n+m)!}\right]^{1/2} \tag{2.110}$$

$$\boldsymbol{B}_{mn}(\theta,\varphi)=\left(\hat{\theta}\frac{dP_n^m(\cos\theta)}{d\theta}-\hat{\varphi}\frac{jm}{\sin\theta}P_n^m(\cos\theta)\right)e^{jm\varphi} \tag{2.111}$$

$$\boldsymbol{C}_{mn}(\theta,\varphi)=\left(\hat{\theta}\frac{jm}{\sin\theta}P_n^m(\cos\theta)-\hat{\varphi}\frac{dP_n^m(\cos\theta)}{d\theta}\right)e^{jm\varphi} \tag{2.112}$$

$$\boldsymbol{P}_{mn}(\theta,\varphi)=\hat{r}P_n^m(\cos\theta)e^{jm\varphi} \tag{2.113}$$

$P_n^m(\cos\theta)$ is the Legendre functions of the first kind of degree n and order m [28]. Due to linearity of Maxwell's equations and boundary conditions, the expansion coefficients of the incident and scattered wave given in Eqs.(2.106) and (2.107) are related through a transition matrix, $\mathbf{T}$ as [28]

$$p_{mn}=\sum_{n'=1}^{\infty}\sum_{m'=-n'}^{n'}\left[\boldsymbol{T}_{mnm'n'}^{11}a_{m'n'}+\boldsymbol{T}_{mnm'n'}^{12}b_{m'n'}\right]$$

$$q_{mn}=\sum_{n'=1}^{\infty}\sum_{m'=-n'}^{n'}\left[\boldsymbol{T}_{mnm'n'}^{21}a_{m'n'}+\boldsymbol{T}_{mnm'n'}^{22}b_{m'n'}\right] \tag{2.114}$$

Equation (2.114) can be expressed in matrix notation as

$$\begin{bmatrix} p \\ q \end{bmatrix} = \boldsymbol{T} \begin{bmatrix} a \\ b \end{bmatrix} = \begin{bmatrix} \boldsymbol{T}^{11} & \boldsymbol{T}^{12} \\ \boldsymbol{T}^{21} & \boldsymbol{T}^{22} \end{bmatrix} \begin{bmatrix} a \\ b \end{bmatrix} \tag{2.115}$$

Equation (2.115) is the key point for the T-matrix computation. A fundamental property of the T-matrix approach is that the elements of the T-matrix are independent of the incident and scattering fields, and it only depends on the shape, size parameter and refractive index of the scattering particle. When an incident field is expanded in vector spherical harmonics, the expansion coefficients a_{mn} and b_{mn} are

$$a_{mn} = 4\pi(-1)^m j^n d_n \mathbf{C}^*_{mn}(\theta_i)\mathbf{E}^i exp(-jm\varphi_i) \tag{2.116}$$

$$b_{mn} = 4\pi\left(-1\right)^m j^{n-1} d_n \mathbf{B}^*_{mn}\left(\theta_i\right)\mathbf{E}^i exp(-jm\varphi_i) \tag{2.117}$$

where $\left(\theta_i, \varphi_i\right)$ indicates the direction of incident wave since a_{mn} and b_{mn} are directly related to the incident direction [28]. Also, $\mathbf{B}^*_{mn}$ and $\mathbf{C}^*_{mn}$ are the complex conjugate of the functions given in Eqs. (2.111) and (2.112), respectively and d_n is given as

$$d_n = \left[\frac{2n+1}{4\pi n(n+1)}\right]^{1/2} \tag{2.118}$$

If the elements of the T-matrix and expansion coefficients for the incident wave are given in Eqs. (2.116) and (2.117) have known, the scattering wave can be calculated by using vector spherical harmonics given by Eq. (2.108) through (2.113). The complete mathematical derivation of the elements of the T-matrix is based on the extended boundary condition method (EBCM) developed by Waterman [27].

The T-matrix is a more general method than Mie scattering because it is used to calculate scattering field for axially symmetric particles i.e. spheres, and spheroids. Therefore, the common practice is to validate the T-matrix method with the Mie scattering by set the chord ratio $\left(cr\right)$ of the spheroid to 1. The chord ratio is the ratio of the horizontal axis to the vertical axis of the spheroid scatterers and so, for an oblate spheroid, the chord ratio is larger than 1 and for a prolate spheroid it is smaller than 1 as given in Figure 2-12.

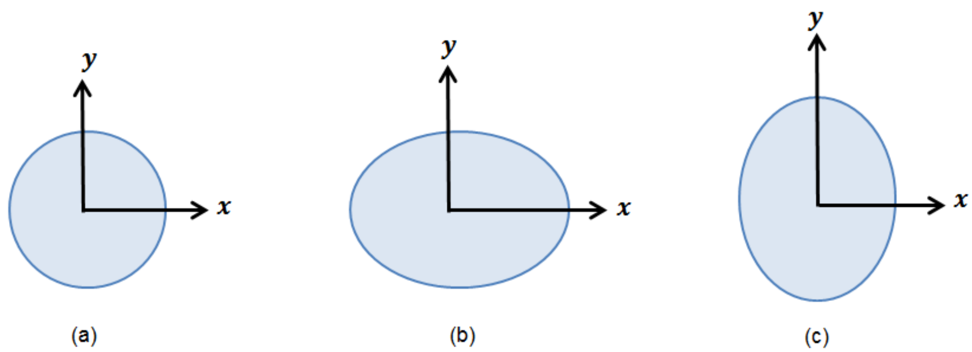

Figure 2-12 The illustration of geometry for (a) sphere with $cr = 1$ (b) oblate spheroid with $cr > 1$ and (c) prolate spheroid $cr < 1$

To build the connection between the set of vector spherical harmonic functions for Mie scattering, $\mathbf{M}_{e1n}^{(3)}, \mathbf{M}_{o1n}^{(3)}, \mathbf{N}_{e1n}^{(3)}$ $\mathbf{N}_{o1n}^{(3)}$ given by Eq.(2.97) and for T-matrix approach $\mathbf{M}_{mn}, \mathbf{N}_{mn}$ expressed by Eqs. (2.108) and (2.109) the following relations are considered

$$\mathbf{M}_{mn}(\theta,\varphi) = (-1)^m \gamma_{mn}\left(\mathbf{M}_{emn}^{(3)}\left(k\mathbf{r},\theta,\varphi\right) + j\mathbf{M}_{omn}^{(3)}\left(k\mathbf{r},\theta,\varphi\right)\right) \tag{2.119}$$

$$\mathbf{N}_{mn}(\theta,\varphi) = (-1)^m \gamma_{mn}\left(\mathbf{N}_{emn}^{(3)}\left(k\mathbf{r},\theta,\varphi\right) + j\mathbf{N}_{omn}^{(3)}\left(k\mathbf{r},\theta,\varphi\right)\right) \tag{2.120}$$

Since m is set to 1 in Eqs.(2.119) and (2.120), and the orthogonality property of the Legendre function for the particles have spherical symmetry, the expansion coefficients and the scattering fields calculated by the Mie scattering and the T-matrix approach are the same [28].

Chapter 3

Backscattering Model of Precipitation for Spaceborne Radar

Remote sensing of precipitation by ground-based or spaceborne remote sensors has become a popular subject in many areas such as hydrology, agriculture, meteorology or climatology. Especially, in the second half of the 20th century, spatial and temporal the knowledge of precipitation was expended by taking advantage of technologically sophisticated devices located either on the Earth’s surface (e.g., ground-based radars, disdrometers) or aboard space platforms (e.g., spaceborne radars, microwave sensors) [46].

Spaceborne precipitation radars aim to record long term precipitation data including vertical profile information. This information is used to calculate approximately the total amount of global precipitation which is a major component of the water cycle, primary source of the fresh water on the planet and crucial for climate changing or global warming studies [46,47].

On the other hand, it is important to understand the scattering and absorption process of the earth surface and hydrometeors particles to analyze remotely sensed data. In this respect, various theoretical models were developed to calculate scattered wave from the surface of the earth or hydrometeors [7,8]. The overall idea behind modelling studies is to provide an effort to help meteorologists and hydrologists by explaining how physical properties of hydrometeors, i.e. the size, morphology, and dielectric, are related to the optical properties. Numerical models based on a forward modelling scheme have aimed to explain the interaction between hydrometeors, i.e. rain or hail drops, snow, cloud droplets, and the scattering field. In this study, we focused on a physical microwave backscattering model to calculate backscattering from precipitation.

In Section 3.1, the geophysical model of precipitation and rain layer parameters is explained. In Section 3.2, a computational model which is used to calculate the backscattering wave from precipitation is described. Finally, in Section 3.3 model validation with the TRMM (Tropical Rainfall Measuring Mission) data will be stated.

3.1 Geophysical Model of Precipitation

Modelling of precipitation over oceans or the earth's land surfaces and calculating scattering data using known geophysical parameters relates different precipitation types is important to interpret the measurement data. In general, such a model which is used to calculate backscattering wave from precipitation should be a combination of volume scattering due to medium inhomogeneities and surface scattering due to boundary discontinuities [7,8,14].

Before preceding discussion with details relates microwave scattering model, it is useful to explain the vertical profile of precipitation. When a spaceborne precipitation radar sends out the electromagnetic waves of near-constant power in very short pulses concentrated into a narrow beam in the vertical direction with a certain incident angle, the wave first interacts with clouds mostly located at the top part of the troposphere. An illustration of precipitation observed by spaceborne radar is given in Figure 3-1. The height of the troposphere extends from the sea level up to 32,800 feet (10 km) at the high altitudes and 47,570 feet (14.5 km) in the tropics. It is the part of the atmosphere where most temperature variances and storms occur. In troposphere, temperature increases at a rate of about 2 °Celsius (C) every 1,000 feet of altitude from the sea level and pressure decreases at a rate about one inch every 1,000 feet of altitude from the sea level. The temperature is around -50 °Celsius (C) at the top part of the troposphere and around 0 °Celsius (C) around 16,400 feet (5 km) from the sea level. Therefore, the amplitude is higher than 16,400 feet (5 km) is known as the freezing layer and this is where mostly dry snow or dry hail occurs around. At the lower altitudes, hail or snow drops start melting if the surface temperature is higher than 0 °Celsius (C). By depending on the melted water content, it is possible to observe wet hail, spongy hail, wet snow or pure rain precipitation by radar. As a result, the vertical profile of precipitation characterizes the changing related physical parameters of the hydrometeors such as size, shape, composition or water content with respect to height. It is important to construct microphysical model of precipitation to calculate accurately backscattered signal [47].

As an example, in Figure 3-2, overpass of NAMMA (The NASA African Monsoon Multidisciplinary Analyses) experiment 20060901-142310 case published by Matthew, Chandrasekar and Lim in 2011 was shown [48]. NAMMA mission was based in the Cape Verde Islands, 350 miles off the coast of Senegal in west Africa to observe the structure and evolution of Mesoscale Convective Systems over continental western Africa and to examine the impact to water content and energy budget. In Figure 3-2, the reflected power Z (dBZ) at Ku and Ka band was shown with respect to height (km) and distance (km). The dashed lines labelled as the profiler A, B and C, for different horizontal distance the reflectivity profile with respect to height is seen more clearly in Figures 3-3 and 3-4 where the melting layer (ML) located approximately between 4 and 5 km [48]. In Fig. 3-3 for profiles A and B, and in Fig. 3-4 for profile C, above the melting layer, the low reflectivity, Z, and differential reflectivity, DFR, are due to low dielectric constant of ice particles. When ice particles passing over the melting layer, water content increases due to melting, but at the same time, the presence of the ice particles causes the low extinction loss, and therefore, the highest reflectivity occurs. After the melting layer, the reflectivities slightly increase around 1 or 2 dB near the ground level mainly because of the aggregation of rain drops and increasing drop size.

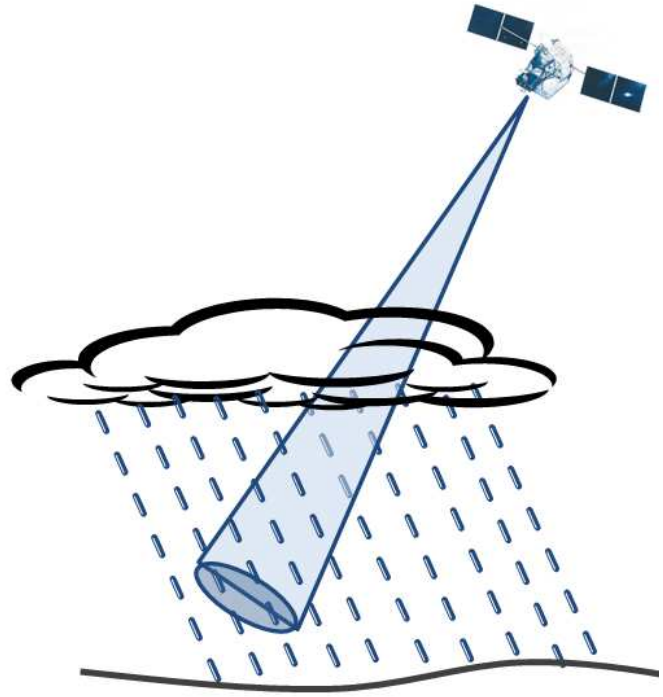

Figure 3-1 Rain type precipitation observed by space borne radar

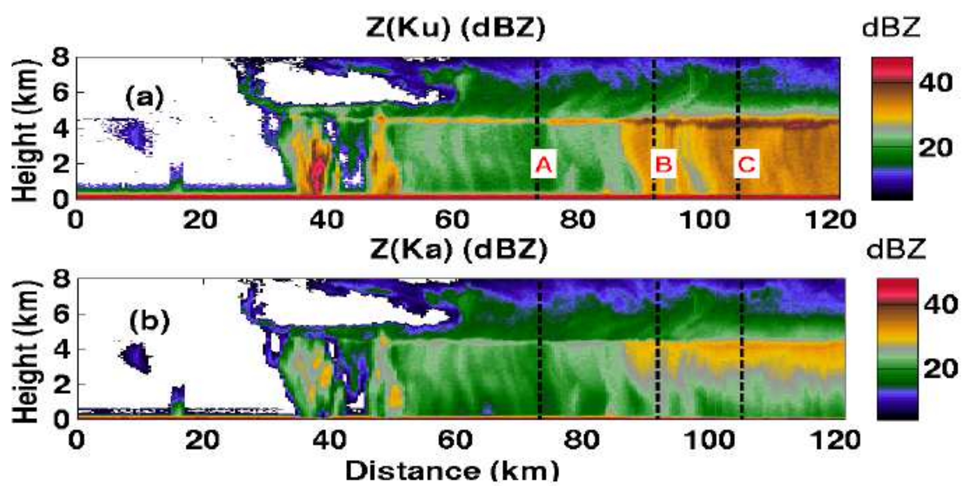

Figure 3-2 Vertical reflectivity profile relates NAMMA experiment for the case

20060901-142310 [48]

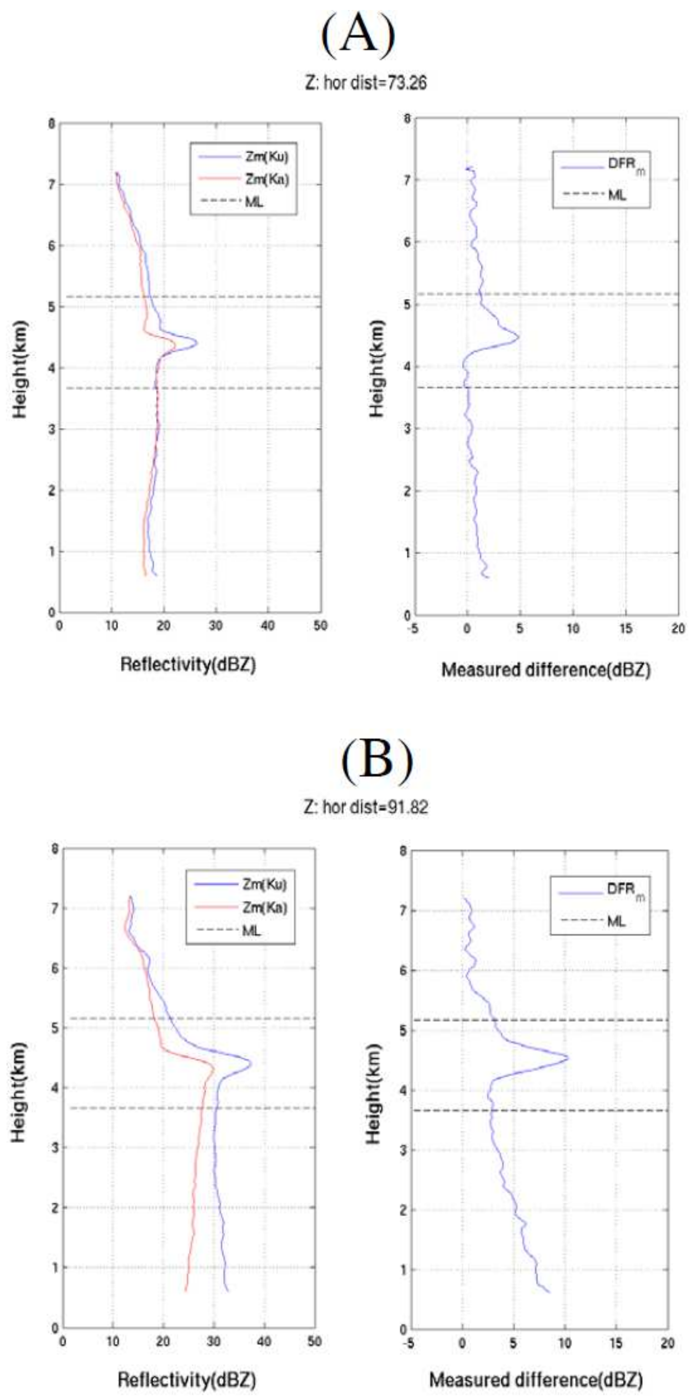

Figure 3-3 Vertical reflectivity and differential reflectivity profile for profiler A and B relates NAMMA experiment for the case 20060901-142310 [48]

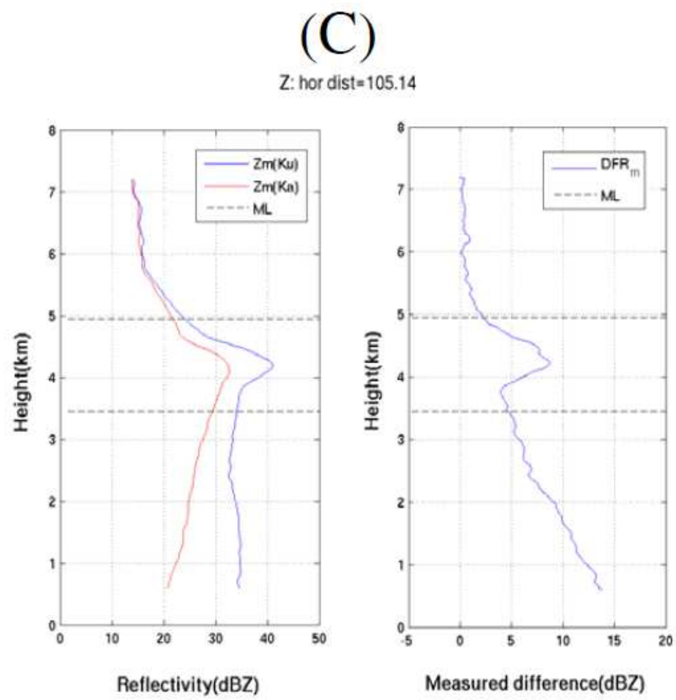

Figure 3-4 Vertical reflectivity and differential reflectivity profile for profiler C relates NAMMA experiment for the case 20060901-142310 [48]

To take into account vertical profile of precipitation, one way is to partition inhomogeneous precipitation column i.e. rain column into the sublayers. In this case, since the measurement system is a space-borne radar and the radar beam is pointing on the vertical direction, the back scattered wave from each sublayer directly relates the parameters chosen to be characterized vertical profile of precipitation.

By considering pure rain type precipitation, the physical structure of the rain column and its multilayered model representation is shown in Figure 3-5. The top layer is designated as aerosol droplets or cloud drops which can be characterized as a group of ice or water droplets [41,62]. On the other hand, the bottom layer which is ground surface can be modelled in various forms such as vegetation, land or sea. Between the top and bottom layers, the inhomogeneous rain layer is partitioned into sublayers to take into account its vertical profile, as well as, the interaction between rain and clouds and also, between rain and the ground surface.

The space-based weather radar transmits electromagnetic waves through the rain column. Since the rain column is represented by a multilayered model, while the wave travels along the vertical direction with a certain incident angle, the part of the energy is scattered from each sublayer, some part is transmitted through to the next layer, and the rest is absorbed inside the layer. Although the scattered wave from each sublayer is in all directions, the some part of it is on the backward direction called reflected wave which is measured by the radar. To calculate accurately all the interactions i.e. absorption, scattering, the physical parameters of rainfall for each sublayer should be chosen properly with respect to the rain rate. In the following section, the estimation of rainfall parameters are explained since they will be used in model as known physical parameters for each sublayer to simulate vertical profile.

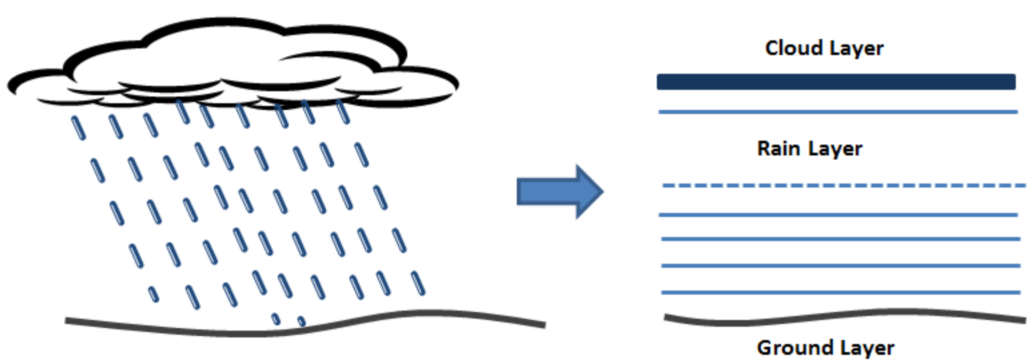

Figure 3-5 Layered model structure to simulate vertical profile of precipitation [62]

3.2 Radar Rainfall Estimation

The studies based on the estimation of rainfall from radar measurements are aimed at extracting rainfall parameters directly from backscattered energy using inverse modelling techniques. In most studies based on inverse modelling technique, rainfall rate, size or drop size distribution is retrieved from measured data using empirical methods. Empirical models mostly use the regression analyses to find the best fit between measured microwave backscattering data and direct measurements by rain gauges or disdrometers [4,34,32]. They have simpler calculations and easier implementation than computational modelling studies but the major problem is their applicability. In another word, the correctness of the empirical model can be questionable for the situation which has not been considered as a case in the algorithm.

On the other hand, methods based on the forward modelling technique provide an alternate way to calculate measured scattered data by considering given physical rainfall parameters and certain assumptions in calculations [5,7,8]. Therefore, the estimated physical parameters using inverse models can be used in the forward computational models to calculate measured data. The aim of the forward models is to improve inversion technique and to provide better understanding the effects of physical parameters of precipitation to the backscattering data. Since this study is based on a forward model, the estimation of rainfall characteristics is important to calculate backscattered energy accurately.

The estimation of rainfall from microwave remote sensing is related understanding of the microphysics of rainfall. The overall aim of radar rainfall rate retrieval algorithms is to provide accurate information for raindrop shape, fall velocity and raindrop size distribution (DSD) from the radar measurements.

The most desired characteristic of rainfall is the rain rate which is also known rainfall intensity, designated by the symbol R given theoretically as [36]

$$R = 6\pi 10^{-4} \int_{D_{min}}^{D_{max}} D^3 N(D)\, v_t(D)\, dD \tag{3.1}$$

where D is the raindrop diameter, $N(D)$ is the drop size distribution (DSD) and $v_t(D)$ is the terminal fall velocity of the raindrops. The units for R, D, $N(D)$ and $v_t(D)$ are mmh^{-1}, mm, m^{-3}mm^{-1}, and msec^{-1}. Equation (3.1) can be also applied to calculate precipitation rate for any type of precipitation. The terminal velocity $v_t(D)$ for hydrometeors is strongly related to the size and density of particles. It also depends on the shape and ambient air density [36]. Theoretical studies show that it can be approximately calculated with a power-law relation as

$$v_t(D) = aD^b \tag{3.2}$$

where the typical range for the value a is between 3.6 and 4.2 while b is varying from 0.6 to 0.67 to provide best fit with measurements [36]. In most studies, the terminal velocity is $v_t(D) \cong 3.78D^{0.67}$ given by Atlas and Ulbrich [34,35]. If this relationship is applied to Eq. (3.1), the rainfall intensity changes the 3.67th moment of DSD. Thus, the rainfall intensity is sensitive to the number of concentration for relatively medium and small size drops but not for large size.

3.2.1 Gamma Drop Size Distribution

Drop size distribution (DSD) defines the total number of raindrops $N(D)$ per unit volume. Exponential, lognormal, and gamma parametric forms have been used as DSD functions in former studies. Exponential form distribution also known as Marshall Palmer distribution was originally introduced by Marshal and Palmer in 1948 [32]. Moreover, further improvement in terms of measurement accuracy was achieved by gamma distribution provided by Ulbrich in 1983 [34]. Today, gamma form DSD which involves also exponential type distribution is representative of a wide range of naturally occurring DSDs, and it is the most commonly used in literature [49,50]. The gamma distribution can be represented by three parameters N_0, μ, and Λ as

$$N(D) = N_0\, D^{\mu} e^{-\Lambda D}, \qquad 0 \le D \le D_{max} \tag{3.3}$$

where the unit of $N(D)$ is m^{-3} cm^{-1} if drop diameter D is given in unit of cm. The exponent, μ, called the distribution shape parameter can have any positive and negative value. Note that for $\mu = 0$, gamma function is simplified to the exponential form. The coefficient N_0 has the unit $\mathrm{m}^{-3}\mathrm{cm}^{-1-\mu}$ and Λ, known as slope term, has unit cm^{-1}. These three parameters define the number distribution for varying drop sizes and all of them are related to the rain rate. It has been shown by Ulbrich, the slope term Λ is approximately

$$\Lambda = \frac{3.67 + \mu}{D_o} \tag{3.4}$$

where D_o (cm) is the median volume diameter. Equation (3.4) is accurate within 0.5% for all $\mu > -3$ [34]. The median volume diameter, D_o is calculated using mass water content, M as

$$D_o = (3.67 + \mu)\left[\frac{6M}{\pi N_o \Gamma(4+\mu)}\right]^{\frac{1}{(4+\mu)}} \tag{3.5}$$

where Γ is the complete gamma function [34]. The theoretical calculation of M is

$$M = \frac{\pi}{6}\rho_w \int_{D_{min}}^{D_{max}} N(D) D^3 dD \tag{3.6}$$

where M has unit gm^{-3} and ρ_w has unit of gcm^{-3}, if the unit of a drop diameter D is given as cm. The three parameters given in Eq. (3.3) are directly related to the rain rate. However, due to extremely large space-time variability of the rainfall, it is not possible to have one standard DSD equation with certain parameters to apply to all possible rainfalls. For the same median drop diameter D_o, and mass water content M, the effect of the shape parameters μ to the gamma drop size distribution is demonstrated by Ulbrich and given in Figure 3-6 where the rain rates are 22-23 mm/h, M is 1 g/m^3, and drop diameters are between 0.1 mm to 4.5 mm. The gamma DSD given in Fig. 3-6 is constructed using Eqs. (3.3), (3.4) and (3.5).

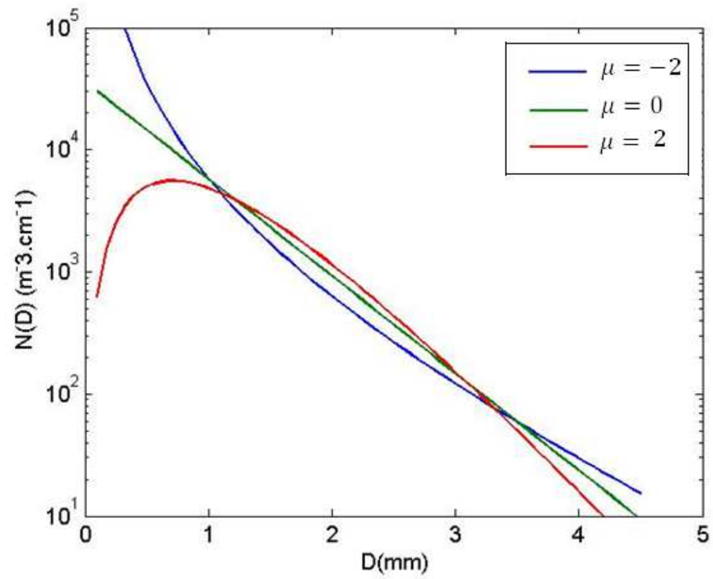

Figure 3-6 The effect of shape parameter, μ to the gamma rain drop size distribution [34]

3.2.2 Rain Parameters for Different Rainfall Types

In general, for different types of rainfall i.e. showers, stratiform or thunderstorm rain, various empirical equations are given in literature to construct direct relation between rainfall intensity R and reflectivity Z or median drop diameter D_o. One classification of the type of the rainfalls with respect to rain rate intervals was given by Malinga and Owolawi in 2013 which is summarized in Table 3-1 [51].

The empirical relation between D_o and R for various types of rain and DSDs was studied and published by many researches. This relation is given in the form of

$$D_o = \alpha R^{\beta} \tag{3.7}$$

where the range for α is 0.031< α <0.130 and for β is 0.11< β <0.80 [36]. D_o is estimated by considering the drizzle and widespread types of rainfall data with the rain rate up to 10 mm h^{-1} by Fujwara [52] given in Figure 3-7. In this work, gamma DSD was used with the shape parameters μ =0.18 and $N_o = 1.96\times10^5$. Moreover, α and β are estimated as 0.082 and 0.21, respectively [52]. Moreover, since μ and N_o are known, the $N(D)$ for the chosen rain rates and size ranges can be calculated (see Fig.3-8).

Table 3-1 Classification of type of the rainfalls with respect to rain rate [51]

Rain Types	Rainfall Rate
Drizzle (very light, light rain)	0.1 mm h^{-1} < R < 5 mm h^{-1}
Widespread (moderate – heavy rain)	5 mm h^{-1} < R < 10 mm h^{-1}
Shower (heavy – very heavy)	10 mm h^{-1} < R < 40 mm h^{-1}
Thunderstorm (extreme)	R > 40 mm h^{-1}

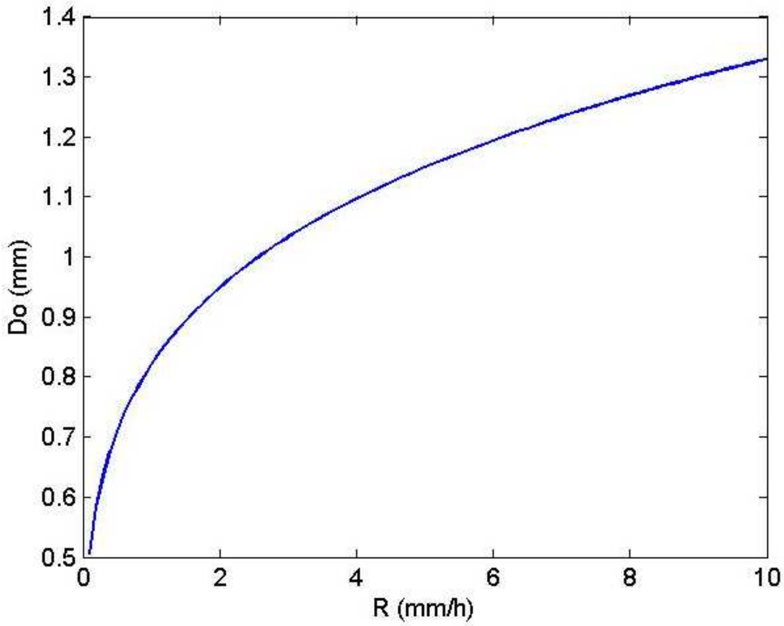

Figure 3-7 Estimated D_o for the drizzle and widespread rainfall with the R up to 10 mm/h by Fujwara [52]

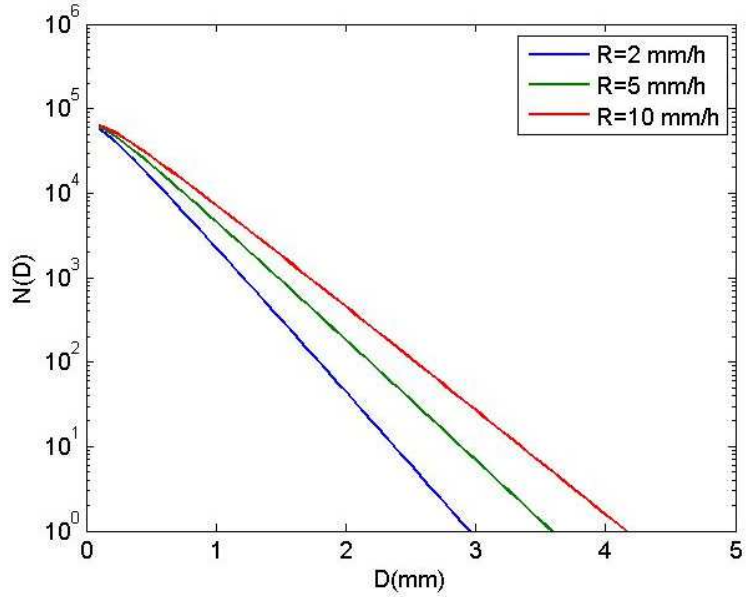

Figure 3-8 $N(D)$ for the drizzle and widespread rainfall with the rates are 2, 5 and 10 mm/h [52]

To consider shower type of rain with the rain rate from 1.0 mm h^{-1} to 40 mm h^{-1}, α and β are estimated as 0.106 and 0.16, to estimate approximately D_o as given in Fig.3-9 [34,52]. $N(D)$ for chosen rain rates and size range is calculated using related gamma DSD parameters; μ=1.63 and N_o=7.54×10^6^, as given in Fig.3-10. Similarly, for the thunderstorm type of rain, the calculated D_o and $N(D)$ are found by the empirical relation can be seen from Fig.3-11 and 3-12 [34,52].

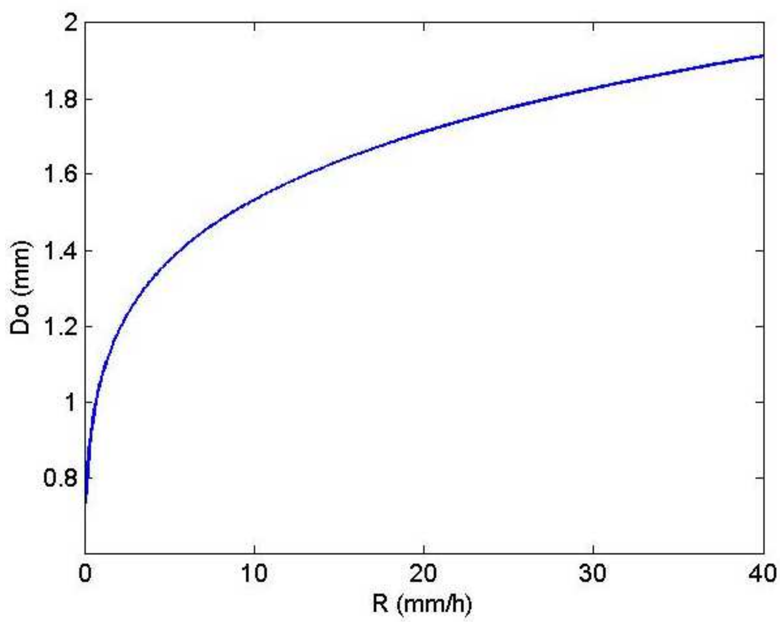

Figure 3-9 Estimated D_o for the shower type rainfall with R up to 40 mm/h [52]

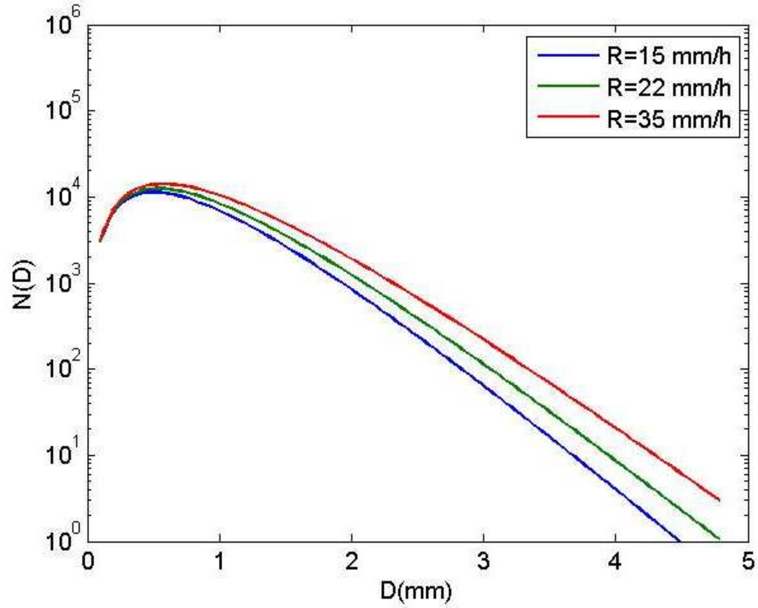

Figure 3-10 $N(D)$ for the shower rainfall with the rates are 15, 22 and 35 mm/h [52]

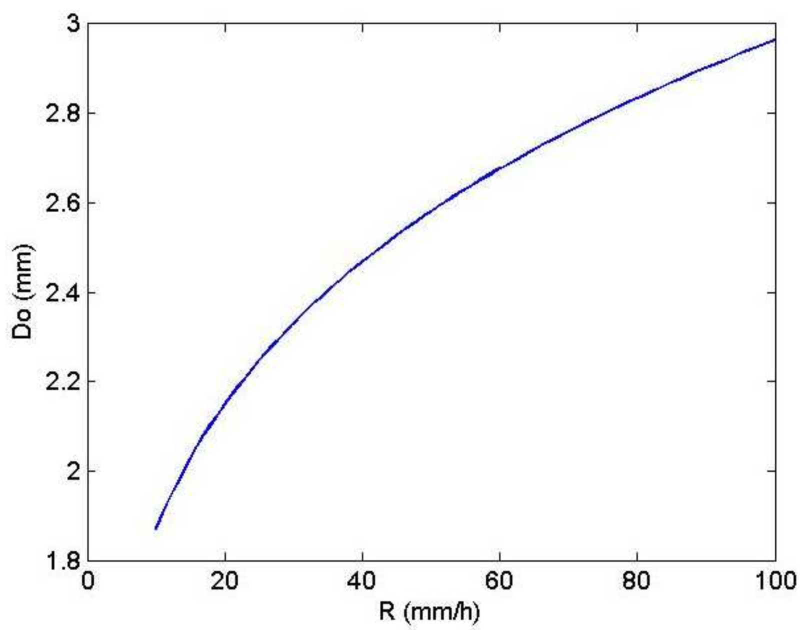

Figure 3-11 Estimated median drop sizes for the thunderstorm type rain [52]

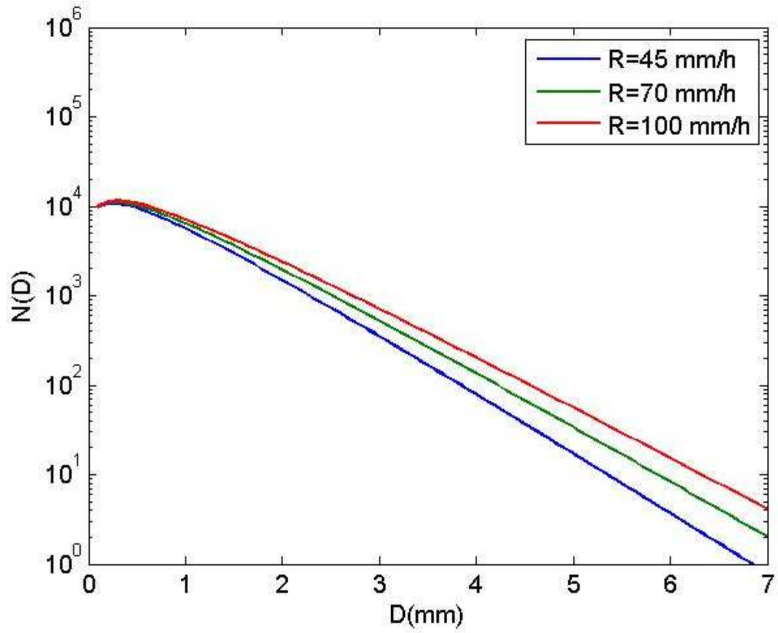

Figure 3-12 $N(D)$ for thunderstorm with the rates are 45, 75 and 100 mm/h [52]

3.2.3 The Shape of the Raindrops and Chord Ratio

Raindrops keep their perfect spherical shape in the absence of external and internal forces. However, while raindrops are descending, their shape is altering due to not only by the external and internal forces but also by collision between drops. During free fall, raindrops reach their equilibrium shape resembling a flattened sphere with wide horizontal base and smoothly curved upper surface by increasing size [1]. This shape can be characterized by a chord ratio, CR, which is the ratio of the horizontal axes, a, to the vertical axes, b, given by

$$CR = \frac{a}{b} \tag{3.8}$$

For a spherical drop, CR is equal to 1, for an oblate spheroid it is bigger than 1 and for a prolate spheroid it is less than 1. The plot given in Figure 3-13 shows changing of the shape with increasing raindrop diameters calculated by the numerical model given by Beard and Chuang [1987] to characterize the relation between raindrop shape and drop diameter [53]. As seen from Figure 3-13, the shape of the raindrop with the diameter up to 1 mm can be characterized as sphere or slightly oblate spheroid and raindrops with larger diameter have more oblate shape. Similarly, the laboratory observations performed by Pruppacher and Pitter classified raindrop shape with three distinct diameter ranges. Class I raindrops have diameter less than 0.25 mm are represented by spherical shape. Class II raindrops have diameter between 0.25 mm and 1 mm exhibit slight distortion and their shape is slightly aspherical. Class III raindrops have diameter more than 1 mm marked as oblate spheroids [54].

The fundamental reason behind of the estimation chord ratio is to calculate rain water content accurately. Several observations from Brandes indicates that the most correct determination of aspect ratio, which is defined as $1/CR$, of the rain drops can be approximated by [55]

$$\begin{aligned} \begin{matrix} aspect \\ ratio \end{matrix} = \frac{1}{CR} = \frac{b}{a} &= 0.9951 + 2.51\times10^{-2}\left(D\right) - 3.644\times10^{-2}\left(D^{2}\right) \\ &+ 5.303\times10^{-3}\left(D^{3}\right) - 2.492\times10^{-4}\left(D^{4}\right) \end{aligned} \tag{3.9}$$

Where D is equal spherical volume diameter in mm. By considering equal spherical volume diameters of the raindrops are varying from 0.1 mm to 5 mm, the implementation of the Eq. (3.9) for the calculation of the chord ratio (CR) is given in Figure 3-14.

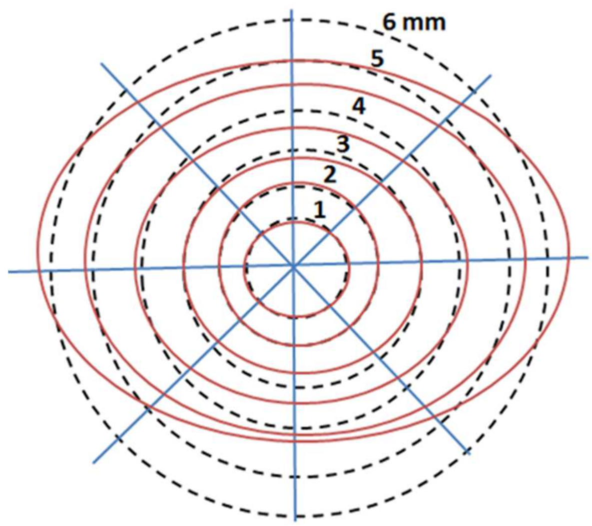

Figure 3-13 Changing of the rain drop shape with increasing raindrop diameters calculated by the numerical model given by Beard and Chuang [53]

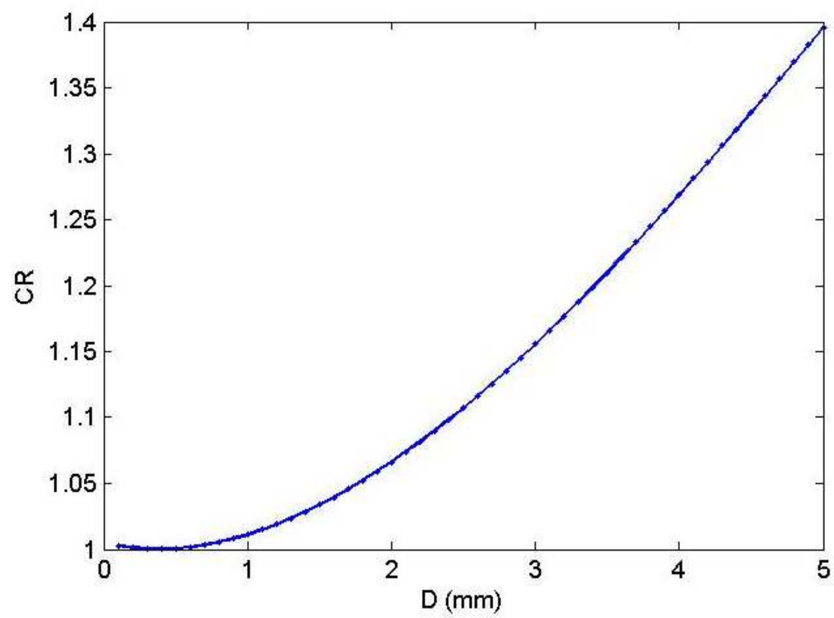

Figure 3-14 The relation between CR and drop diameters calculated by the formula published by Brandes in 2002 [55]

3.3 Computational Model of Precipitation for Spaceborne Radar

The rainfall environment can be described as an inhomogeneous medium consisting of randomly distributed particles with various shapes and random orientation. So, it is not possible to perform exact simulation of such a complex natural environment and take account all the wave particle interactions without any assumption. To simplify the problem, model assumptions based on measured data are applied.

Weather radars send out several independent pulses through the inhomogeneous medium with several randomly distributed scatters. During receiving time, the return pulses are averaged to calculate reflected mean power. Then, it is possible to model inhomogeneous random media by approximating scatterers as spheres or spheroids with effective size and chord ratio. However, since the main objective of this study is calculation of scattered intensity for a whole precipitation column from the top i.e. clouds to the bottom i.e. sea surface, changing of the physical parameters through the vertical direction is taken into account by multilayered model.

The inhomogeneous rain column observed by spaceborne radar, its physical model structure and scattering process through the rain column to calculate scattering intensities are shown in Figure 3-15. In the multilayered model, each sublayer is characterized by a set of parameters to calculate the volume scattering phase matrix for a sphere or a spheroid scatterer. The drop size and water volume fraction change with altitude within a sublayer is assumed to be negligible. In another word, each sublayer is statistically homogeneous.

In the conventional T-matrix approach and Mie scattering theory, only independently scattering particles are assumed. This means that the distance between scatterers is wide enough to scatter waves in exactly the same way as if all other particles did not exist [40]. This assumption holds when the volume fraction of scatterers is low, and the size of the scatterers is small with respect to wavelength. The volume scattering phase matrix calculated under these approximations is called Rayleigh phase matrix. As an example, if rain is considered as an inhomogeneous medium with randomly positioned scatterers, this approximation is accurate for light to medium rain rates with small drop diameters relative to the wavelength. However, since the independent scattering assumption does not meet for media consisting of densely populated scatterers, a modified Mie and T-matrix phase matrix can be used to account the effects of close spacing between scatterers. The construction of the volume scattering phase matrix, and the calculation of the single scattering volume extinction and scattering coefficients for closely spacing scatterers by the Mie scattering or T-matrix approach is explained in Chapter.2 under Section 2.8.

After calculation of the single scattering volume scattering phase matrices for infinitesimal layers, the solution of the vector radiative transfer (VRT) model is performed numerically by the matrix doubling method for the multiple scattering effect. The matrix doubling method was introduced in Section 2.4. By assuming the rain column is bounded with rough boundaries which are clouds at the top and sea surface at the bottom; the interface between cloud and rain as well as the interface between sea surface and rain are all analyzed by using integral equation model (IEM). The effect of interface discontinuities is accommodate by the multilayered VRT model through boundary conditions explained in Section 2.6. Then, the phase matrix for the entire rain column is calculated by combining the volume and surface scattering phase matrices in the solution of the VRT equations for multilayered inhomogeneous medium as given in Section 2.7.

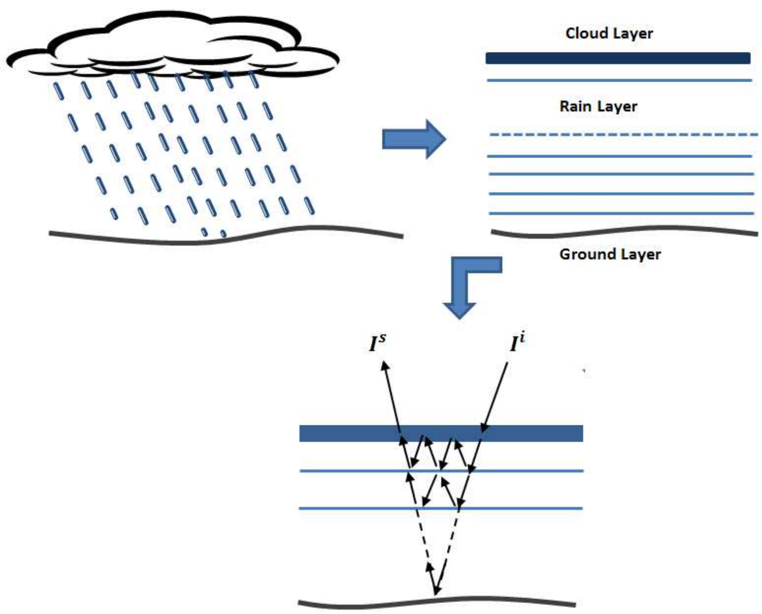

Figure 3-15 Geometry of the inhomogeneous rain column, its physical model structure and scattering process through sublayers

3.4 Multilayered VRT Model Validation with TRMM Data

To validate multilayered VRT model with TRMM (The Tropical Rainfall Measuring Mission) data, an inhomogeneous rain column is partitioned into 12 sublayers to simulate its vertical profile. In previous studies, the volume scattering phase matrices for differential layers were performed by considering Mie scattering for closely spaced scatterers and the multilayered VRT model predictions published by Li, Tjuatja and Dong in 2012 [41]. Model validation of this study with TRMM measurements under $10\sim11$ $\mathrm{mm\,h^{-1}}$ is given in Fig. 3-16 and related model parameters can be seen from Table 3-2 where $k\sigma$ is the sea surface rms height multiplied by propagation constant, k, and kL is the sea surface correlation length multiplied by propagation constant, k.

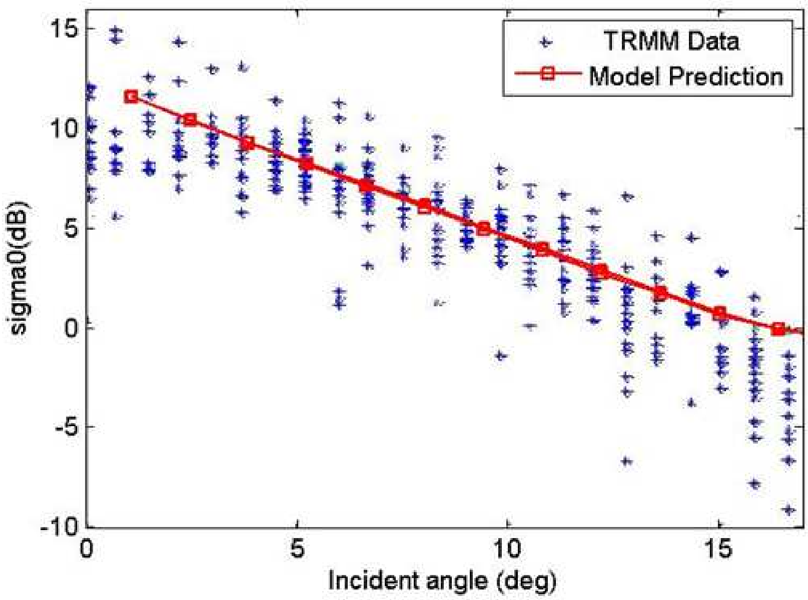

Figure 3-16 VRT multilayered model validation with TRMM measurements for 10-11 mm/h published by Li [41]

Table 3-2 Parameters for TRMM data comparison [41]

Parameter	Frequency (GHz)	Rain rate (mm/h)	Sea surface
Mie VRT-Model	13.8	10.45	$k\sigma = 1.1$, $kL = 15.0$
TRMM	13.8	10~11 (mm/h)	N/A

In this study, the calculation of volume scattering expansion coefficients for nonspherical particles is performed by taking advantage of the T-matrix approach and so, rain drops can be modelled as spheres or oblate spheroids with different chord ratios (CR). To validate the VRT layered model, volume scattering expansion coefficient for each sublayer is calculated using T-matrix approach by setting the chord ratio, CR to 1.

Thus, spherical scatterers are used in T-matrix approach to perform comparison with the VRT model based on Mie scattering theory. Expansion coefficients calculated in T-matrix approach is simplified to the Mie scattering expansion coefficient for the same size spherical scatterers.

For the drizzle and widespread rain with the rain rate around 8 mm/h, median drop diameter is approximately calculated, and it can be seen from Fig. 3-7, in Section 3.2.2. In the VRT multilayered model, small variations around the median drop diameter with altitude is accommodate with the average number of drops calculated by gamma DSD model explained in Section 3.2.1 and 3.2.2. Vertical radius profile of raindrops considered for the comparison between multilayered VRT models is given by Fig. 3-17, and model parameters are given in Table 3-3. Note that the VRT model is based on the mks (meter kilogram second) unit system, therefore, in the calculation of the volume fraction of drops, in the Eq. (3.6), the unit of radius of raindrops should be converted to meters. Then, the volume fraction of water, Vf, for each sublayer is a dimensionless quantity since it is equal to the volume of drops multiplied by the average number of drops within the unit volume. It is given as

$$Vf = \frac{\pi}{6}\int_0^\infty D^3 N\left(D\right) dD \tag{3.10}$$

A comparison is made between two multilayered VRT models. One uses Mie scattering, and the other one uses the T-matrix approach for the calculation of volume scattering expansion coefficients for each sublayer as given in Fig. 3-18. It can be seen from the Fig 3-18, two models completely match for the same size spherical shape scatterers, as expected. Further analysis of the multilayered VRT model to analyze the effect of the physical parameters of the precipitation particles i.e. drop size, drop shape or precipitation rate to the scattered data is presented in Chapter.5.

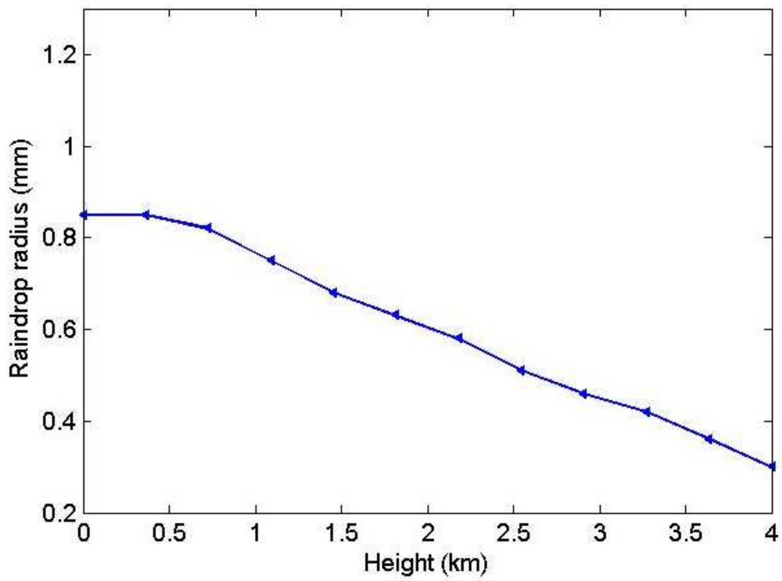

Figure 3-17 Vertical radius profile of raindrops considered for the comparison between multilayered VRT models based on T-matrix approach and Mie scattering theory

Table 3-3 Model parameters for the comparisons between VRT multilayered models given in Fig 3-18

Rain rate (mm/h)	Volume fraction	Frequency (GHz)	Median drop diameter (m)	Sea surface
8.00	0.55e-5	13.6	1.1e-3	$k\sigma = 1.1$, $kL = 15.0$

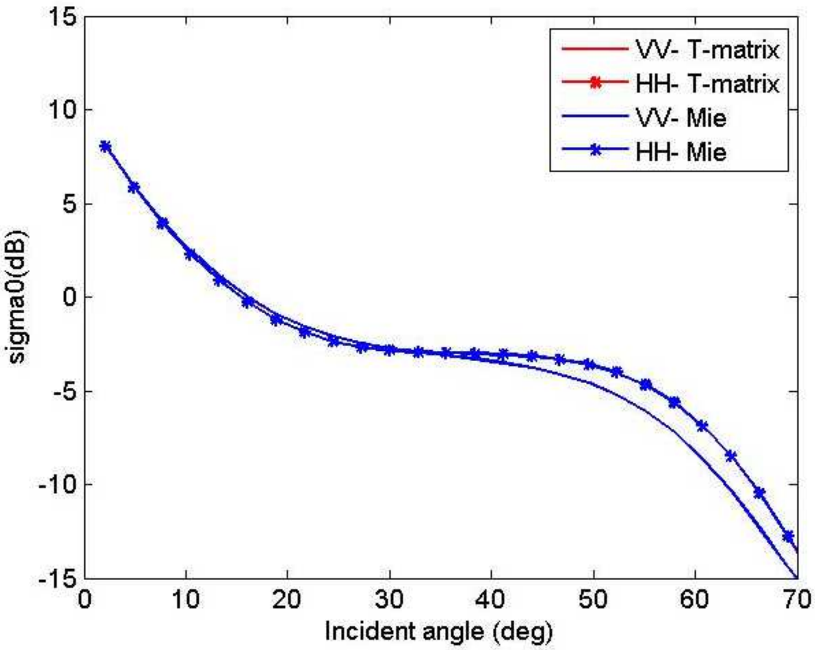

Figure 3-18 The comparison between multilayered VRT models based on T-matrix approach and Mie scattering theory considering same size spherical shape drops.

Chapter 4

Backscattering Model of Precipitation for Ground-Based Radar

Since the low level of atmosphere is the part of most convective storms are occurred, the accurate analyses of measured data by ground-based radars and estimation and forecasting of weather conditions have high importance to reduce the number of traffic accident, death, and delay due to weather-related problems.

According to report published by National Research Council (NRC) in 2004, nearly 1.5 million vehicular accidents with consequences 7,000 deaths, 800,000 injuries and over $42 billion costs are associated with weather impairs. Moreover, snow, ice, and fog cause an additional 500,000 hours of delays annually for drivers [56]. Therefore, using ground-based radar systems for the quantitative estimation of precipitation has played a crucial role and the number of surface measurement systems are increasing to improve weather analysis and prediction. Today, dual-polarized ground-based weather radars such as NEXRAD, CASA, or CSU-CHILL which have more potential than traditional single polarized radars are used for detection of precipitation type and determination of its size. In this chapter, the microwave backscattering model is introduced for dual-polarized ground-based weather radar system to analyze back scattering from rain and snow.

4.1 Measurement Geometry

In this section, a geophysical microwave scattering model is constructed by considering ground-based radar (GR) systems to provide accurate quantitative estimation of precipitation. To construct such a model, first, the measurement geometry of a GR should be introduced.

Unlike space borne radar, GRs are stationary and they can be deployed as fixed on a top of a building or a radar tower. A GR has to measure rain from a lateral direction and so, it is pointing a small elevation angle off the ground surface. As seen from Fig.4-1, the radar beam of a GR lies in the nearly horizontal direction. However, because of the curvature effect of Earth, the radar beam reaches up to higher altitudes for the farther distances. The height of the radar beam h, is measured from the center of the beam to the ground surface as illustrated in Fig.4-1. The two parameters that control h are radar elevation angle, Φ_e and maximum radar range, R_{max}. Under standard atmospheric conditions, the approximate calculation of h by including the earth's curvature effect is given as

$$h = h_r + \sqrt{R^2 + \left(\frac{4}{3}a\right)^2 + 2R\frac{4}{3}a\sin\Phi_e} - \frac{4}{3}a \tag{4.1}$$

where h_r (km) is the height of the radar antenna, which can be estimated as the height of the radar tower or the building that the antenna is fixed on, R (km) is the radar range, Φ_e (deg) is the radar beam elevation angle, also known as tilt angle, and a (km) is the Earth's radius which is given approximately 6371 km [36]. In Fig.4-2, the illustration of the range-height relation of a GR for elevation angles 4, 6, 8, 10 and 12 degrees is given for the radar range of 1-100 km. In this calculation h_r is ignored.

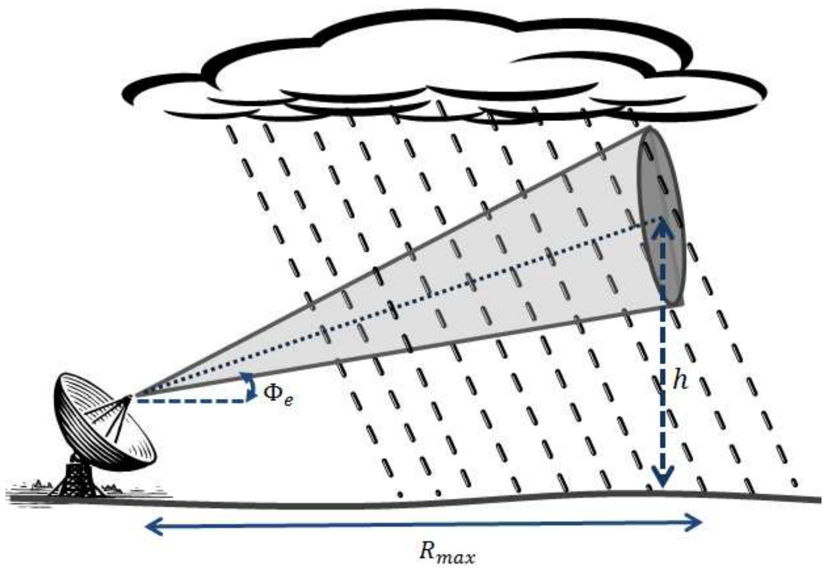

Figure 4-1 Geometry of a GR

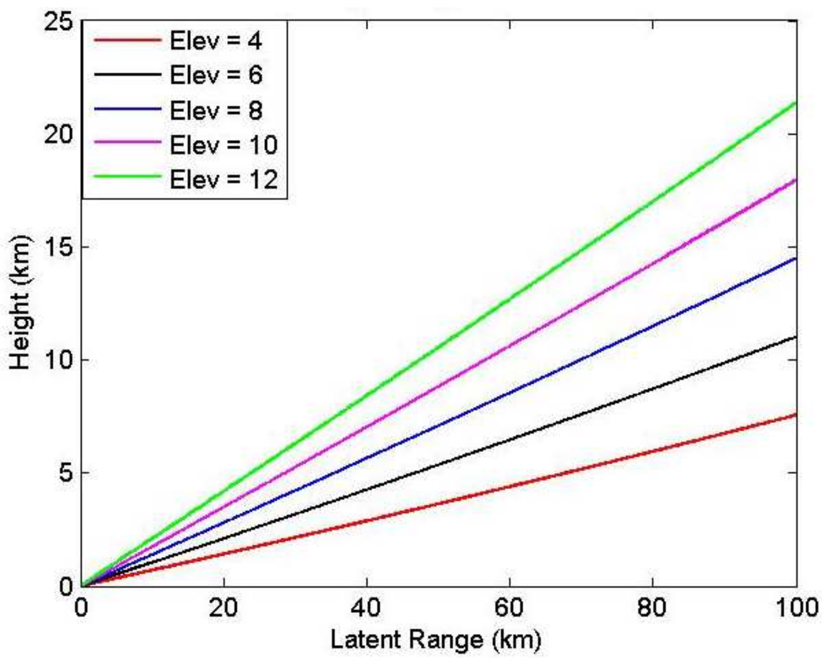

Figure 4-2 Range-height relation of a GR for five elevation angles

For a pulse-type radar set, GR sends out several independent pulses through the radar beam and illuminates a large number of particles at the same time. Since meteorological targets such as fog, rainfall, hail or snowfall composed of a larger number of hydrometeors, the pulse radar seems them as a distributed target within a sample volume which is also known as contribution volume, V_c. Within the radar range, the transmitted signal is first scattered from the closest contribution volume and some part of the energy returns to the radar. The remaining energy is transferred to next contribution volume and the same process repeats itself until the signal is completely attenuate. Therefore, a radar beam consists of i number of contributing volumes of particles located at different ranges. The height of the contributing volumes can be calculated by using the total elapsed time for the received signal, the length of the contribution volumes, the radar dwell time, the curvature effect of the earth, and the radar range. Fig.4-3 shows the illustration of multiple contributions volumes in the radar beam at the different altitudes for a GR.

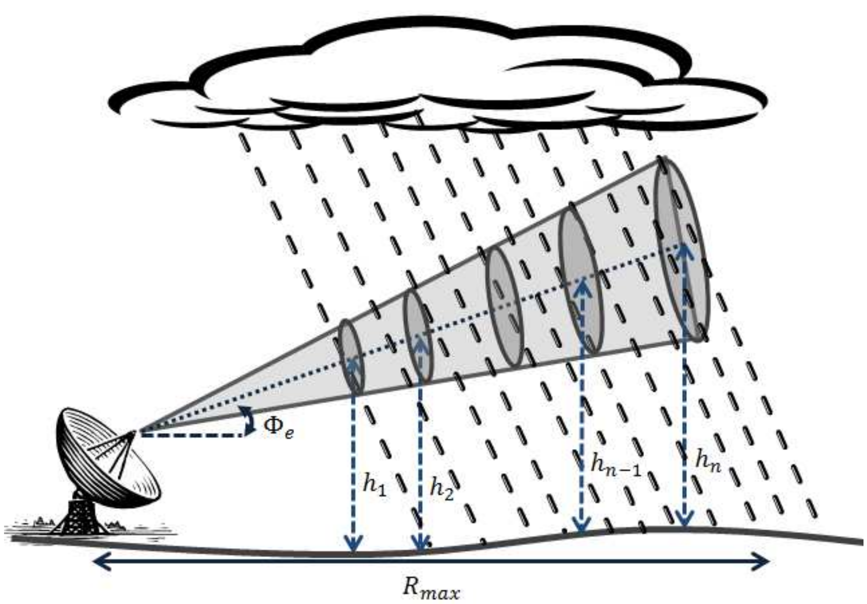

Figure 4-3 Multiple contribution volumes in the radar beam

The volume of contribution in the radar beam is approximated by the radar's vertical beam width, $R\theta$ and horizontal beam width, $R\varphi$, as follows

$$V_c = \pi \frac{\Delta l}{2} \left(\frac{R\theta}{2} \right) \left(\frac{R\varphi}{2} \right) \tag{4.2}$$

where $\Delta l/2 = c\tau/2, c$ is the speed of light, and τ is pulse width [4]. In Fig.4-4, the geometry of a contribution volume is depicted.

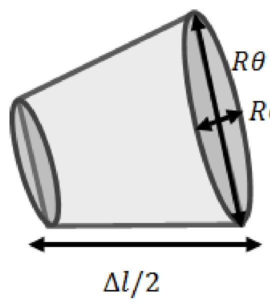

Figure 4-4 Geometry of a contribution volume in radar beam

A GR measures precipitation from a very close distance to a few hundred kilometers, however, for large distances the radar beam spreads out significantly. It can be seen from Eq.(4.2), that the contribution volumes spread widely by the square of the radar range which is also known beam spreading. Therefore, contribution volumes at the long distance cover much more of the precipitation from the lower to the higher level of the atmosphere. For example, if the elevation angle of radar is around 6°, within the 45-50 km radar range, the radar beam reaches the frozen level of atmosphere which is around 5 km altitude. Commonly the upper part of the convective storm around frozen level mostly consists of ice, or dry hail type of precipitation, while the middle level of precipitation contains pure rain or wet hail/snow due to increasing of temperature and air pressure with decreasing altitude. Therefore, the size, shape or composition of the hydrometeors may change significantly due to the vertical profile of the convective storm.

This is true especially within the contribution volumes located around the melting layer as seen from Fig.4-5. For the approximate calculation of effective permittivities of the contribution volumes containing a mixed type of precipitation, the proper mixing rule should be chosen. Calculation of the effective dielectric permittivity calculation for a unit volume in the radar beam is explained in the following section.

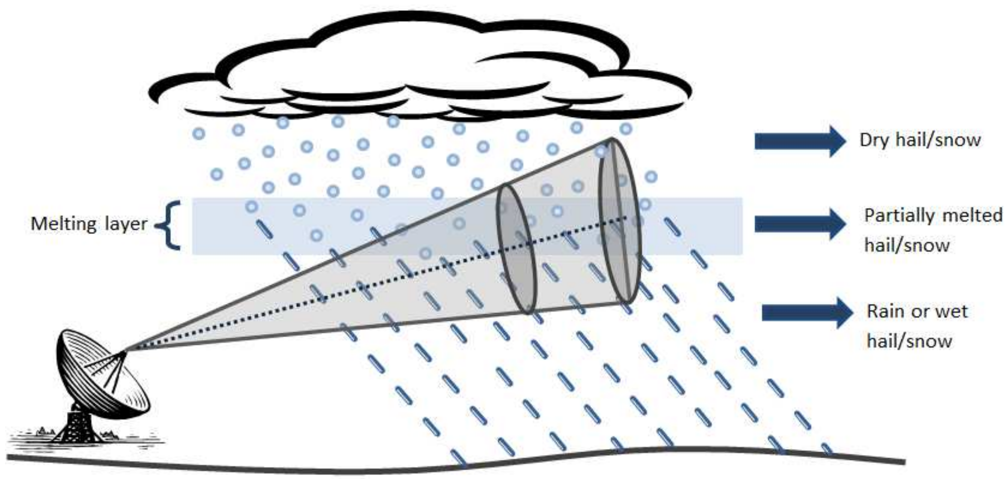

Figure 4-5 Illustration of a contribution volume filled with different type of precipitation

4.2 Geophysical Parameters for Rain, Hail and Snow

To calculate backscattered power from each range interval, contribution volumes should be characterized by a set of parameters such as volume fraction of precipitation, size, or effective permittivity of hydrometeors. In Chapter 3, under Section 3.2, the geophysical parameters for different types of rainfall are described. However, for space borne radar, since the radar beam is pointed out nearly vertical direction, the layers in the model are characterized by a set of parameters which are directly matched with the vertical profile of the precipitation. On the other hand, a ground-based radar system measures return power from precipitation in the lateral direction with an expanding radar beam for long distances. Therefore, for the heterogeneously filled unit volumes with different precipitation hydrometeors, effective permittivity calculation for the mixtures need to be performed as explained in following section.

4.2.1 Calculation of Effective Permittivity for Rain and Wet/Dry Hail

Precipitation hydrometeors that form in clouds and fall to the ground, change their geophysical structure and so, in practice the radar beam illuminates a mixture which have constituents water, ice and air with different fraction of volumes. To calculate scattered intensities from such a microscopically complicated mixture, the common way to represent the mixture is by an effective permittivity and treat it as macroscopically homogeneous. Several dielectric formulas developed in the past to calculate effective permittivities of the mixture from known dielectric constant, volume fraction and shape of the constituents [7,13,57].

To calculate effective permittivity for rain and hail, microwave dielectric properties of pure water and ice should be known. Previous studies show that they are well understood by means of the Debye relaxation equation [7]. According to the Debye formulation, the dielectric permittivity of pure water, ε_w at microwave frequencies is

$$\varepsilon_w = \varepsilon_{w\infty} + \frac{\varepsilon_{w0} - \varepsilon_{w\infty}}{1 + j2\pi f \tau_w} \tag{4.3}$$

where ε_{w0} is the dimensionless static dielectric constant of pure water, $\varepsilon_{w\infty}$ is dimensionless high-frequency limit of dielectric constant of water, τ_w is relaxation time of pure water in seconds and f is the frequency in Hertz [7]. Lane and Saxton determined the $\varepsilon_{w\infty}$ as 4.9 [7] and the relaxation time of pure water τ_w is obtained by Stogryn as

$$2\pi\ \tau_w(T) = 1.1109\times10^{-10} - 3.824\times10^{-12}T$$

$$+6.938\times10^{-14}T^2 - 5.096\times10^{-16}T^3 \qquad (4.4)$$

where T is in ℃ [7]. Also, after several experiments to constructed of an empirical relation by Klein and Swift for ε_{w0} is [7]

$$\varepsilon_{w0}(T) = 88.045 - 0.4147T + 6.295\times10^{-4}T^2 + 1.075\times10^{-5}T^3 \qquad (4.5)$$

Using Eqs.(4.3), (4.4) and (4.5) dielectric permittivity of pure water is given in 1-20 GHz for 0 and 20 ℃, in Fig. 4-6. Although, the dielectric constant for pure water is known and well understood, when precipitation occurs, water particles are took placed in the air with various fraction of volumes for different rain rates. To model such a heterogeneous medium, mixing rules are needed to calculate dielectric constant of the medium approximately by considering inclusions shape, volume fractions, spatial distribution and orientations relative to the direction of the incident electric field vector. The fundamental assumption of the mixing rules is the host and inclusion materials are used to have isotropic dielectric constants. This assumption simplifies the problem significantly and it is usually valid for remote sensing problems.

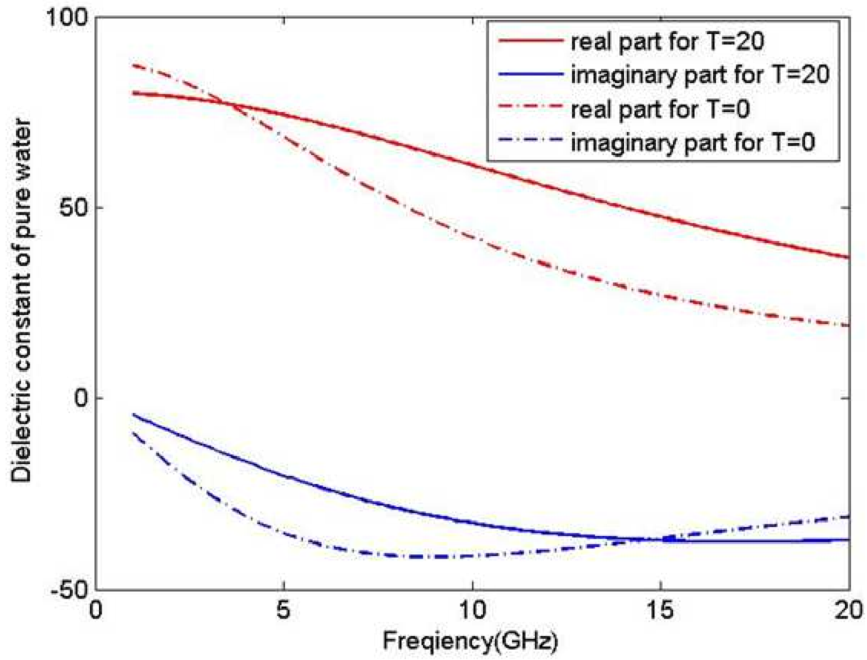

Figure 4-6 Dielectric permittivity of pure water in 1-20 GHz for 0 and 20 ℃

One mixing rule used in the remote sensing community is the Polder-van Santen/de Loor formulation defined the relation between volume average electric field and flux density by weighting with the corresponding volume fractions [13]. Also, it is supposed that the ratio of the internal and external fields inside and outside of the inclusions is given by the fractions of the dielectric constants of the inclusion and host medium. Originally, the formula is derived for a two phase mixture and spheroid inclusions are randomly dispersed in the host medium. Then, the effective dielectric constant is given as

$$\varepsilon_{eff} = \varepsilon_e + \frac{f_i}{3}(\varepsilon_i - \varepsilon_e)\sum_{u=a,b,c}\left[\frac{1}{1 + A_u\left(\frac{\varepsilon_i}{\varepsilon^*} - 1\right)}\right] \tag{4.6}$$

where ε_e is the permittivity of the environment, ε_i is the permittivity of the inclusions, f_i is the volume fraction of inclusions, and ε^* is the effective dielectric constant for the region immediately around the inclusion. If the fraction of volumes of the inclusions is small enough i.e. $f_i \leq 0.01$, then ε^* can be taken as equal to ε_e, since it is possible to ignore short range particle interactions. In Eq.(4.6), A_u is the depolarization ratio of the ellipsoids along its u axis. In this study, we consider spherical shape scatterers. Therefore, the depolarization ratio, A_u is $A_a = A_b = A_c = 1/3$ for $a = b = c$.

The geometry of the contribution volume is shown in Fig.4-7 where spherical inclusions with permittivity ε_i are randomly positioned in the environment of permittivity ε_e. For instance, in the case of rainfall, to calculate the effective dielectric constant for a unit volume, the host medium should be considered as air and the inclusions are water drops modeled as spheres.

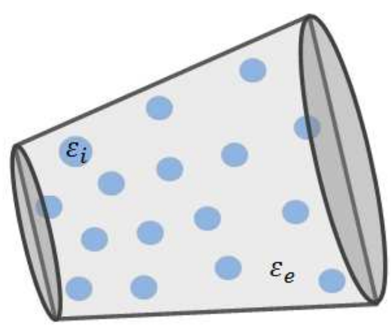

Figure 4-7 A contribution volume with raindrop inclusions in the air

Besides the rain type precipitation, the contribution volumes may involve melting particles or ice and rain particles in the same volume around the melting layer. The real part of the dielectric constant of pure ice particles in microwave region is 3.15. It is independent of both frequency and temperature since the relaxation of pure ice takes place in the kilohertz region [7]. Experimental results show that the imaginary part of the dielectric constant of ice particles changes slope around 1 GHz and then, it is increasing with higher frequency values. However, it is very small number relative to the real part of the dielectric constant for ice particles. For instance, at 0℃ the imaginary part of dielectric constant for pure ice is calculated as 6.4×10^{-5} at 10 GHz by Auty and Cole [7].

For the calculation of effective permittivity for melting particles, the hydrometeor is considered as the ice core covered with a water shell as seen from Fig.4-8 to apply Tinga-Voss-Blossey (TVB) formulation [13]. In the TVB formula, randomly dispersed confocal spheres are consisting of the ice core as an inner sphere with dielectric permittivity ε_i and a water shell surrounded around ice core with dielectric permittivity ε_h. The TVB formula is given by

$$\varepsilon_{eff} = \varepsilon_h + \frac{3v_i\varepsilon_h\left(\varepsilon_i - \varepsilon_e\right)}{\left(2\varepsilon_e + \varepsilon_i\right) - v_i\left(\varepsilon_i - \varepsilon_e\right)} \tag{4.7}$$

where v_i is the ratio of the volume of the inner sphere to the outer sphere. After calculation of the effective permittivity of the melting particles from Eq.(4.7), since the total volume fraction; f_i of particles in the contribution volume, Eq.(4.6) is applied to calculate effective permittivity for entire unit volume.

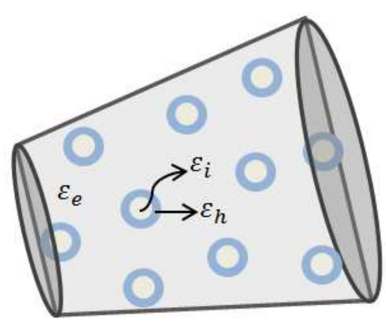

Figure 4-8 The geometry for melting particles

4.2.2 Geophysical Parameters and Effective Permittivity Calculation for Snow

Warm moist air rises, cools and condenses into cloud droplets. When droplets reach to the freezing layer, which is around 5-6 km from the ground, and there is a minimum amount of moisture in the air, ice crystals start forming. Snow crystals grow fast and increase in size due to collision and aggregation. Finally, when heavy enough they start to fall as snowflakes. If the ground temperature is at or below freezing, snowflakes reach to the surface. But this is not a certain condition for snow fall because even if the ground temperature is above the freezing temperature snowflakes can reach the surface before melting completely. Snow particles i.e. snow crystals, snowflakes or low density graupel particles are typically have 1 to 5 mm diameter with a density between 0.05 and 0.89 g cm^{-3} [6]. High density snow is expected for wet particles or solid ice structures.

Snow crystals have a large variety of shapes and can be modelled as needles, plates, dendrites spheres, or spheroids scatterers to calculate reflectivity. In previous studies, as similar to the rain fall, exponential or gamma size distributions with proper slope and shape parameters were applied for snow fall to give direct relation between reflectivity (Z) and snow rate (R). Gunn and Marshal modified exponential drop size distribution (DSD), which was introduced originally for rainfall by Marshall and Palmer, for snow fall and ice crystals and results fit well with snow data especially for the snow drops that had diameters above 1 mm [58]. The proposed exponential form DSD by Gunn and Marshal, for snow fall is

$$N\left(D\right) = N_0\, e^{-\Lambda D} \tag{4.8}$$

where $N_0 = 3.8 \times 10^3 R^{-0.87}$ [58]. $N\left(D\right)$ and N_0 have unit of m^{-3} mm^{-1}. The slope term Λ, has unit cm^{-1} and snow diameter D has unit cm. The slope term is changed with the snowfall rate of melted water, in mm/h as Λ=25.5$R^{-0.44}$. The changing of the median drop sizes of snow drops, D_0 with respect to rain rates is calculated by the empirical relation given as

$$D_0 = 0.14R^{0.48} \tag{4.9}$$

Finally, by using exponential type DSD the constructed $Z-R$ relation for snow type precipitation developed by Gunn and Marshal is [58]

$$Z = 2000R^{2.0} \tag{4.10}$$

Similar emprical relations were found and reported by Sekhon and Srivastava as Z=1780$R^{2.21}$ and D_0=0.14$R^{0.45}$ [59]. In Equations (4.9) and (4.10), the snow rate is given in terms of melted water content of snow which is the product of snow depth and snow bulk density. However, in general, NWS (National Weather Service) reports the snowfall rate in terms of the depth of accumulated snowflakes in per hour. Since it is known that around 2 inch (50.8 mm) per hour snowfall rate actually indicates a snow storm and the fresh snow has a density around 8% of water, the equivalent melted water content of snow is 3 mm/h indicates a strong snow storm which is not seen frequently. By considering up to 4 mm/h snow rate in terms of melting water content, estimated reflectivities and median snow drop diameters by Gun and Marshall and also, by Sekhon and Srivastava are given in Figure 4-9 and in Figure 4-10, respectively.

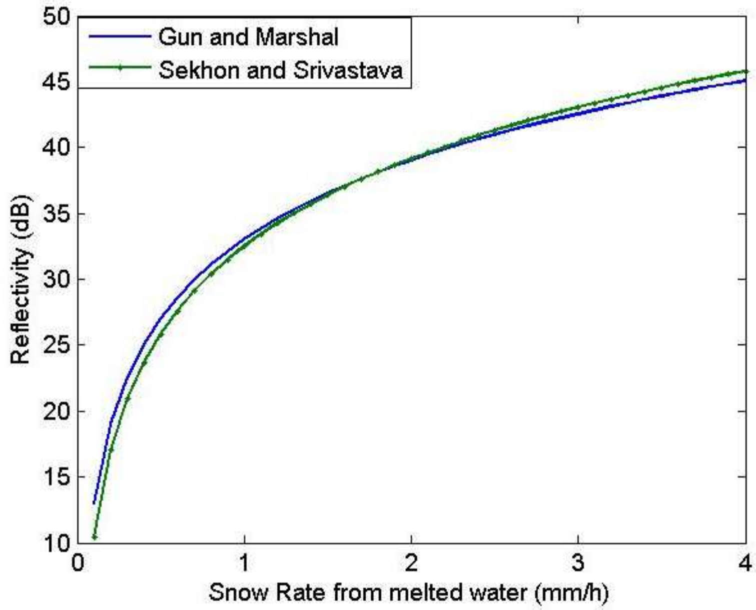

Figure 4-9 Empricial snow rate reflectivity relation

Regardless of crystal shapes, snow fall measurements in the Rayleigh regime show that the typical Z for dry snow is up to 35 dB whereas for wet snow it can be as high as 45 dB due to increasing reflectivity and high dielectric constant of water [6].

Snow fall is assumed to be a random inhomogeneous medium with the scatterers of various shape and random orientation, and size. To measure backscattering from such a medium, a pulse radar sends out several pulses and averages them to estimate the mean power. Therefore, due to random orientation of particles, snow or ice particles can be modelled as spheres.

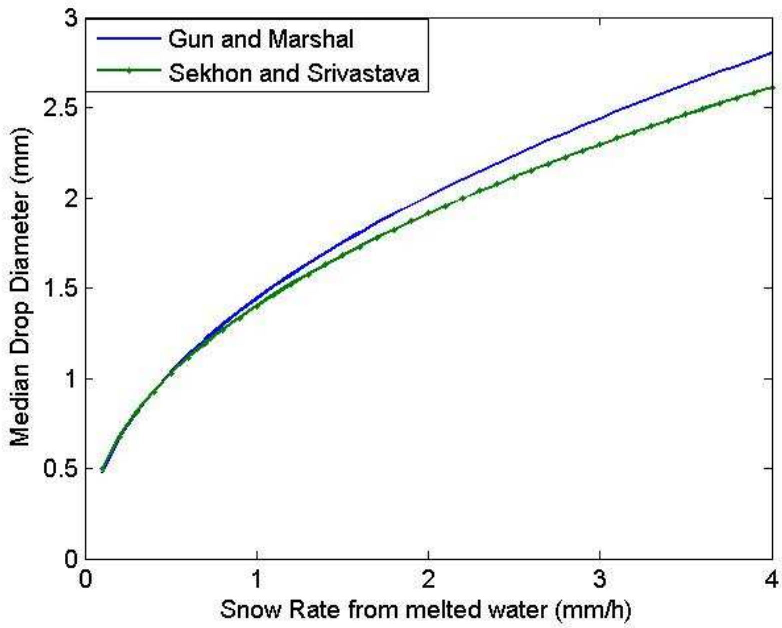

Figure 4-10 Median snow drops diameter changing with reflectivity

Effective permittivity for each contribution volume in the case of pure ice precipitation i.e. dry hail can be calculated by the Polder-van Santen/de Loor formula given by Eq.(4.6) by using the total volume fraction of ice. However, snow drops are a mixed form of air and ice. The most important parameter of the dry snow is its density, ρ_s . Also, the volume fraction of snow, f_s can be uniquely determined from its density by the ratio given as

$$f_s = \frac{\rho_s}{\rho_{ice}} \tag{4.11}$$

where ρ_{ice} is the density of the pure ice and it is 0.9167 g/cm^3. Therefore, the volume fraction and also, the effective permittivity of the snow particles are controlled by the snow density. By considering the spherical shape geometry, the snow density is calculated by the Bruggeman formula since it gives closer results to the experimental measurements especially for higher snow densities according to Sihvola [57]. Bruggeman mixing rule is given as

$$(1-f_s)\frac{(\varepsilon_e-\varepsilon_{eff})}{(\varepsilon_e+2\varepsilon_{eff})}+f_s\frac{(\varepsilon_i-\varepsilon_{eff})}{(\varepsilon_i+2\varepsilon_{eff})}=0 \qquad (4.12)$$

where f_s volume fraction of snow, ε_e is the effective permittivity of the host medium and ε_i is the dielectric constant for inclusion. For calculation of the effective dielectric constant of snow drops, air inclusion in the pure ice must be known. For the density value between 0.05 and 0.89 g/cm^3 of the dry snow calculated relative permittivities are given in Figure 4-11.

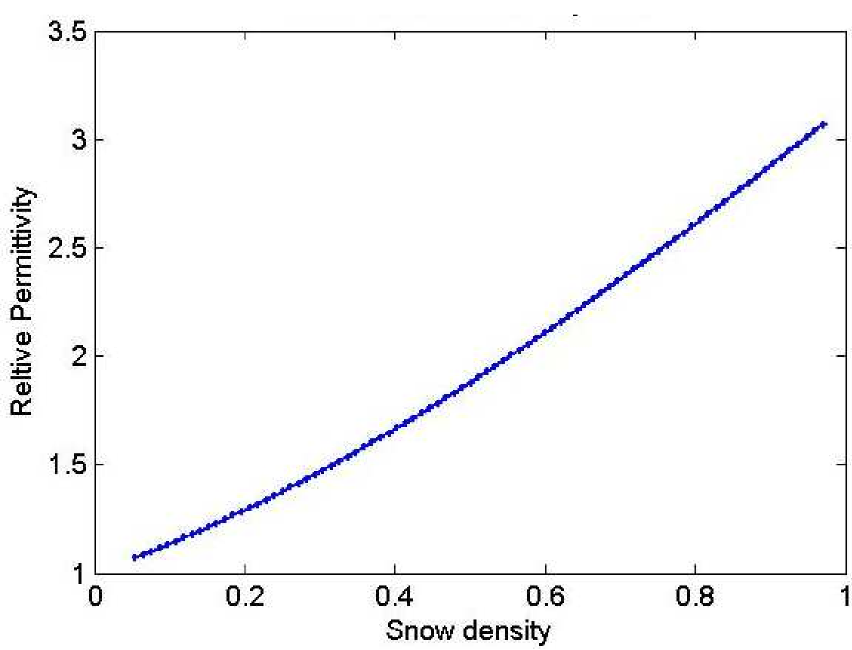

Figure 4-11 Dielectric constant of dry snow with respect to snow density

4.3 Computational Model Description

The aim of this study is calculation of backscattering from the entire radar beam accurately by constructing a geophysical model. For this purpose, the backscattering wave from each contributing volume which represent in the model by a set of parameters should be calculated. Calculation of scattering intensities from the entire radar beam consists of multiple contribution volumes is performed by multilayered VRT equations which is explained in Chapter 2 Section 2.2 and 2.3. In Chapter 3, multilayered VRT model is applied to calculation of the scattered phase matrix which is the combination of volume and surface scattering phase matrices for the entire precipitation column from the clouds to the ground observed by space-borne radar. However, by using the geometry of a GR, the volume phase matrix is only accommodated in the model since the radar beam does not encounter a rough boundary aloft. The volume scattering phase matrices for individual unit volumes is calculated by the Mie scattering theory which is given in Chapter 2 Section 2.8.1 and so, precipitation hydrometeors are modelled as spheres with the complex permittivity.

In this study, the number of sublayers in the model is defined as the same with the number of range gates in the measurement GR system. Let the total number of the sublayer is N and the phase matrix for i^{th} sublayer is $\mathbf{P_i}$, $1 \leq \mathbf{i} \leq N$. By starting with the first sublayer in the radar beam, $\mathbf{P_i}$ is calculated as follows [63];

$$\mathbf{P_i} = \mathbf{P}_{1,2,\ldots.\mathbf{i}} - \mathbf{P}_{1,2,\ldots..(\mathbf{i}-1)} \qquad 1 \leq \mathbf{i} \leq N \tag{4.13}$$

where $\mathbf{P}_{1,2,\ldots.\mathbf{i}}$ is the volume back scattering phase matrix for the entire volume consist of i sublayers and similarly, $\mathbf{P}_{1,2,\ldots..(\mathbf{i}-1)}$ is the volume back scattering phase matrix for totally i-1 sublayers (see Figure 4.12). $\mathbf{P}_{1,2\ldots i}$ and $\mathbf{P}_{1,2,\ldots(i-1)}$ are both calculated by the matrix doubling method which is explained in Chapter 2 Section 2.4 to take into account attenuation and multiple scattering effects. Therefore, the difference between $\mathbf{P}_{1,2....i}$ and $\mathbf{P}_{1,2,....(i-1)}$ is the contribution of the i^{th} sublayer to the backscattering wave. The same calculation is performed for each range unit to simulate entire radar range.

The element of the phase matrix given in Chapter.2 by Eq.(2.20) can be expressed in terms of normalized backscattered radar cross-sections σ^0 as

$$\boldsymbol{I}^s = \frac{1}{4\pi} \int_{4\pi} \boldsymbol{P} \boldsymbol{I}^i d\Omega = \sigma^0 / \cos\theta_s \tag{4.14}$$

where the phase matrix $\boldsymbol{P}$ should be replaced by $\mathbf{P_i}$ for the calculation of scattered intensities $\boldsymbol{I}^s$ for each range gate. In Eq. (4.14), normalized backscattering cross section σ^0 is defined as

$$\sigma^0_{pq} = \frac{\left(4\pi R^2\right)}{A} \frac{\left\langle \left| E_p^s \right|^2 \right\rangle}{\left\langle \left| E_q^i \right|^2 \right\rangle} \tag{4.15}$$

where E_p^s is the p-polarized scattered field, E_q^i is the q-polarized incident electric field, A is the illuminated area by radar, and R is the range from the observation point. Since the scattered intensities are defined in terms of spherical waves and incident intensities are given in plane wave coordinates i.e. v and h, they differ by a normalized solid angle $\left(A cos\theta_s\right)/R^2$. Thus phase matrix which is the relation between scattered and incident intensities is expressed in terms of σ^0 as [63]

$$\mathbf{P_i} = \frac{\sigma_i^o}{cos\theta_s} \tag{4.16}$$

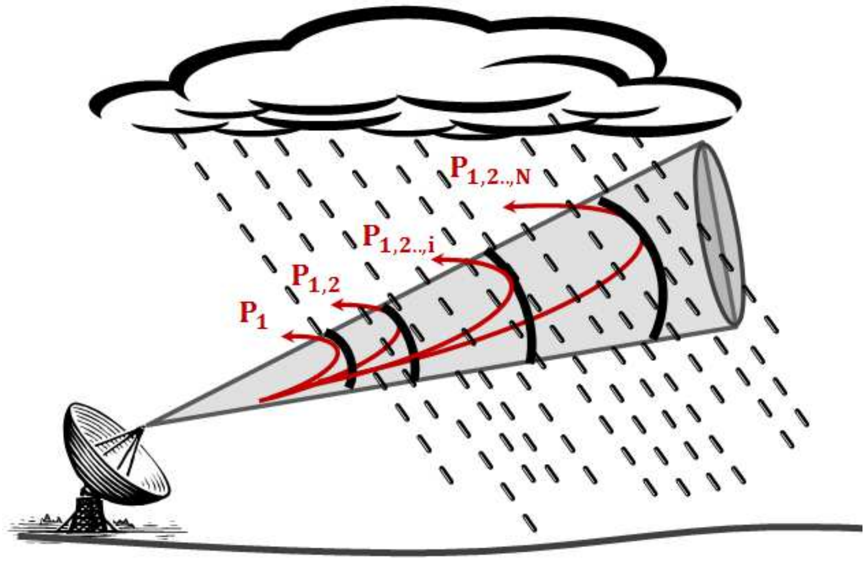

Figure 4-12 Scattering from different range intervals

4.3.1 Model Interpretation with Radar Parameters

To validate the multilayered VRT model with the measurement backscattered power, the relation between the calculated backscattered normalized radar cross-section for each range interval and the measured backscattered power should be explained.

The fundamental relation between the radar parameters, range and target characteristics are given by the radar equation. The scattering geometry for a single target is depicted in Figure 4-13 where $\mathbf{T_x}$ is the transmitter, and $\mathbf{R_x}$ is receiver. When the transmitter, $\mathbf{T_x}$ sends out the power, P_t, with gain, G_t, to the target, the total power per unit solid angle intercepted by the target is given as

$$S_t = \frac{P_t G_t}{4\pi R_t^2} \tag{4.17}$$

where S_t is the incident power density intercepted with the scatterer also known as Poynting vector and $1/4\pi R_t^2$ is the spreading loss related to the range between transmitter and scatterer. The effective area of the target illuminated incident power density is A_{eff} . As seen from Figure 4-13, the total power intercepted by the target is

$$P_{rt} = S_t A_{eff} \tag{4.18}$$

When power illuminates the target, some part of the incident power is absorbed by the target while the rest of it is reradiated. If the fraction of powered is absorbed by scatterer is given by f_a then scattered power is should be

$$P_{st} = P_{rt}\left(1 - f_a\right) \tag{4.19}$$

The power reradiated by scatterers is related to its geometric shape, orientation and also its formation. Some part of the reradiated power, P_{st} is detected by the receiver through its effective area. Therefore, the received power density at the $\mathbf{R_x}$ is given by

$$S_r = \frac{P_{st} G_{st}}{4\pi R_r^2} \tag{4.20}$$

where G_{st} is the gain of scatterer in the direction of receiver and receive power can be written as

$$P_r = A_r S_r \tag{4.21}$$

If Equations (4.17), (4.18), (4.19) and (4.20) are substituted in the Eq.(4.21), P_r is given

$$P_r = A_{eff} \frac{P_t G_t}{4\pi R_t^2} A_r \frac{\left(1 - f_a\right) G_{st}}{4\pi R_r^2} \tag{4.22}$$

where the terms A_{eff} , $\left(1 - f_a\right)$, and G_{st} are directly connected with the target characteristics and can be combined into one term; the radar backscattering cross-section (or backscattering cross-section) with unit of m^2 denoted by the symbol σ as

$$\sigma = A_{eff}\left(1 - f_a\right)G_{st} \tag{4.23}$$

where the term G_{st} is related to the incident and scattering directions of the beam, f_a depends on the dielectric properties of the target and A_{eff} is contingent upon the shape of the target as well as its orientation with respect to direction of the incident wave.

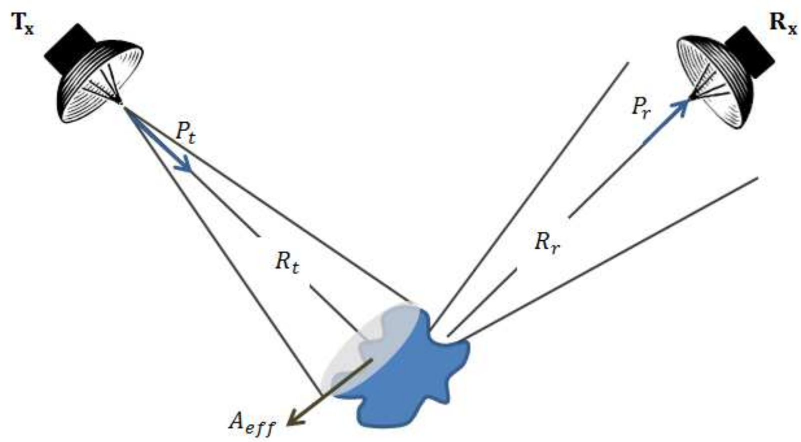

Figure 4-13 Geometry for bistatic radar equation

Equation (4.22) is known as bistatic radar equation and implies that receiver and transmitter antennas are separated. However, the most common situation in remote sensing is for the radar system to use the same antenna as receiver and transmitter i.e. monostatic radar. Therefore following simplifications can be considered

$$R_r = R_t = R, \qquad G_t = G_r = G, \qquad A_t = A_r = A \tag{4.24}$$

By using Eqs. (4.22), (4.23) and (4.24), the monostatic radar equation can be written as

$$P_r = \frac{P_t G A}{\left(4\pi R^2\right)^2}\sigma \tag{4.25}$$

Theoretical studies show that the radar gain is related its area by $A = G\lambda^2 / 4\pi$ where λ is wavelength. If this relation is substituted in Eq. (4.25), the radar range equation becomes

$$P_r = \frac{P_t G^2 \lambda^2}{(4\pi)^3 R^4} \sigma \tag{4.26}$$

Equation (4.26) is the general form of monostatic radar equation for any single target; however, it should be modified to apply meteorological targets since the radar beam illuminates a large number of randomly distributed scatterers i.e. raindrops or snowflakes at the same time. Pulse radar sends out several pulses through the medium which contains many scatterers and average them to find the average receive power. Therefore, an ensemble average of the receive power $\overline{P_r}$ over all space and time is expressed as

$$\overline{P_r} = \frac{P_t G^2 \lambda^2}{(4\pi)^3 R^4} \sum_k \sigma_k \tag{4.27}$$

where P_t and G is out of the summation because they are assumed to be same for each scatterer over the illuminated area. Also, since scatterers are in the far field, the distance from the radar for each individual scatterer is assumed to be same So, the distance between scatterer and measurement point R is taken out of the summation.

If Eq. (4.23) is normalized by the effective area, then it is called normalized backscattering cross-section, denoted by the symbol σ^0, and expressed as

$$\sigma^0 = \frac{\sigma}{A_{eff}} \tag{4.28}$$

If the radar beam illuminates M number of scatterers and each has the effective area ΔA_k, then Eq. (4.27) can be written in terms of σ^0 for multiple scatterers as

$$\overline{P_r} = \frac{P_t G^2 \lambda^2}{(4\pi)^3 R^4} \sum_{k=1}^{M} \sigma_k^0 \Delta A_k \tag{4.29}$$

where the summation implies that phase interference effect between scatterers is ignored. On the other hand, in the VRT model, which is explained in Section 4.2, the normalized cross-section for each contributing volume σ_i^o , $1 \leq i \leq N$ where N is the total number of range gate, is calculated by solving the VRT equation using the matrix doubling method to incorporate multiple scattering and attenuation effects. Then, the calculation σ_i is performed by multiplying σ_i^o with the cross sectional area of the beam A_i which relates to i^{th} contributing volume. Therefore, for each volume of range, the average power received by radar is calculated in the model as

$$\overline{P_{ri}} = \frac{P_{ti} G_i^2 \lambda^2}{(4\pi)^3 {R_i}^4} A_i^{eff} \sigma_i^0 \tag{4.30}$$

where the term σ_i^o is calculated from phase matrix $\mathbf{P_i}$ for each layer by Eq.(4.16) and the A_i^{eff} is calculated by the beam width on azimuth and elevation direction as

$$A_i^{eff} = \pi \left(\frac{R_i \theta}{2} \right) \left(\frac{R_i \varphi}{2} \right) \tag{4.31}$$

where R_i is the range of the corresponding volume from the radar.

4.3.2 Rayleigh Approximation and Reflectivity Factor Calculation

In most studies, since the size of the scatterers is much smaller than wavelength and the distances between scatterers are far enough, back scattering cross-section for each contribution volume, V_c , is derived as the sum of the backscattered cross section for individual particles. By assuming several independent pulses send by radar are averaged to estimate mean power $\overline{P}_r$, the radar equation for multiple scatterer as similar to the Eq.(4.27) is given by

$$\overline{P}_r = \frac{P_t G^2 \lambda^2}{(4\pi)^3 R^4} V_c \sum_{i=1}^{N} \sigma_{iv} \tag{4.32}$$

where the summation is given for the N number of particles in the contribution volume V_c (m^3) by assuming that scatterers are uniformly distributed over the volume i.e. individual back scattering cross-section of scatterers are the same. The term σ_{iv} is the cross-section of each particle per unit volume given with the unit m^2/m^3. In this equation, V_c is defined as the contribution volume given by Eq.(4.2) and if its definition is plugged in the Eq.(4.32), the resulting equation is

$$\overline{P}_r = \frac{P_t G^2 \lambda^2 \theta\varphi h}{512\pi^2 R^2} \sum_{i=1}^{N} \sigma_{iv} \tag{4.33}$$

The more applicable form of the radar equation was derived by Probert-Jones who used Gaussian function to represent power per unit area within the main lobe of the radar beam [4]. The Gaussian shape function causes a reduction of the beam by the factor of $2\ln(2)$ and so, the more exact form of the radar equation is given as

$$\overline{P}_r = \frac{P_t G^2 \lambda^2 \theta\varphi h}{1024\ln(2)\pi^2 R^2} \sum_{i=1}^{N} \sigma_{iv} \tag{4.34}$$

where the term $\sum_{i=1}^{N} \sigma_{iv}$ is called the radar reflectivity and designated by the symbol η (m^2/m^3).

In general, since scatterers are not uniformly distributed over the volume, and the number of scatterers per unit volume is given by a number density N_i (m^{-3}), then the term reflectivity is expressed by

$$\eta = \sum_i N_i \ \sigma_i \tag{4.35}$$

For spherical scatterers, Mie scattering theory can be applied to calculate backscattering coefficient as [4]

$$\sigma = \frac{\lambda^2}{4\pi}\left|\sum_{n=1}^{\infty}(-1)^n \left(2n+1\right)\left(a_n - b_n\right)\right|^2 \tag{4.36}$$

where a_n and b_n are the Mie coefficients. If size parameter, α for spherical particles is much smaller than 1, i.e. $\alpha = 2\pi r / \lambda \ll 1$, where r is radius of the scatterer, by neglecting higher order terms than the fifth order of α, σ_i for small size spherical scatterers can be simplified as,

$$\sigma_i = \frac{\pi^5}{\lambda^4}\left|K\right|^2 D_i^6 \tag{4.37}$$

where the term K is used to designate $(m^2-1)/(m^2+2)$ and D_i is the particle diameter. Equation (4.37) is derived by assuming small size scatterers in unit volume. This is Rayleigh approximation and if it is substituted in Eq.(4.34), the radar equation with Rayleigh approximation is

$$\overline{P}_r = \frac{P_t G^2 \theta\varphi h \pi^3}{1024\ln(2)\lambda^2} \ \frac{\left|K\right|^2}{r^2}\sum_{V_c} D_i^6 \tag{4.38}$$

where the term $\sum_{V_c} D_i^6$ is called reflectivity factor represented by the symbol Z with unit m^6/m^3.

In general, the drop size distributions are used with proper parameters for different precipitation rates to calculate the reflectivity factor Z. If the number of drops within the contribution volume is given by a drop size distribution $N(D)$, then Z is calculated as

$$Z = \sum N(D) D^6 \delta D \tag{4.39}$$

where δD is the drop diameter interval and $N(D)$ has unit of $m^{-3}m^{-1}$ if drop diameter D is given in unit of m. Equation (4.39) is valid for small size sphere scatterers with respect to wavelength, since it has ignored phase interactions. Moreover, for scatterers do not have spherical symmetry, the backscattering cross-section σ_i depends on the direction of incident and scattering angles. Since raindrops especially those that have diameter larger than 1 mm are more oblique in shape, as explained in Chapter 3, instead of Mie scattering T-matrix approach is used. In this case backscattering cross-section is calculated as

$$Q_{back} = 4\pi \sum_{D=D_{min}}^{D_{max}} \left| f_{v,h}\left(\pi, D\right) \right|^2 N\left(D\right) dD \tag{4.40}$$

where the coefficient 4π comes from the integration over the solid angle. Due to random orientation of scatterer, the function $f_{v,h}\left(\pi, D\right)$ is the scattering amplitude function at vertical or horizontal polarization. Parameters π and D inside the scattering amplitude function indicate the backward scattering direction i.e. $\pi = 180°$ and diameter of the drops respectively. Conceptually Q_{back} given in Equation (4.40) can be used instead of the summation of σ_i over the contribution volume by using drop size distribution. Then, since the reflectivity factor for each scatterer is defined as $Z_i = D_i^6$, it will be polarization dependent due to the function $f_{v,h}\left(\pi, D\right)$, and it can be expressed by

$$Z_{v,h} = \frac{4\lambda^4}{\pi^4 \left|K\right|^2} \sum_{D=D_{min}}^{D_{max}} \left| f_{v,h}\left(\pi, D\right) \right|^2 N\left(D\right) dD \tag{4.41}$$

Therefore, $Z_{v,h}$ is depends on polarization, incident and scattering wave direction, as well as particle shape, size and dielectric properties. In general, $Z_{v,h}$ has the unit of mm^6/m^3 and so if the scattering amplitude function $f_{v,h}$ and wavelength λ is calculated in unit of m, $Z_{v,h}$ should be multiplied by the factor of 10^{18} due to unit conversion. Usually it is given in dB form. The ratio of Z_h to Z_v is defined as the differential reflectivity Z_{dr} which is

$$Z_{dr} = \frac{Z_h}{Z_v} \tag{4.42}$$

The term Z_{dr} reveals information about the shape and size of hydrometeors. However, the scattering amplitude function $f_{v,h}$ is calculated in most studies defined in the far field, and the interaction between scatterers are ignored. So, it is also assumed independent scattering in general.

In this study, T-matrix approach is also used for calculation of backscattering cross-section for each contribution volume. However, since in the calculation of scattering amplitude function all the scattering and incident directions are used to account for all the interaction between scatterers, the computed Z_{dr} values are relatively lower than that given in previous studies. Another disadvantages of using the T-matrix approach for ground-based model is that it significantly increases the computational time since it has to do summation over all the θ_{inc} and ϕ direction for each scattering angle to calculate the cross section for each unit cell.

4.4 Model Validation

In this study, model results are compared with measured data obtained from the X-band dual polarization Phase Tilt Weather Radar (PTWR) for snow and rain type precipitation. In Section 4.4.1, the PTWR specification and measurement system explanation is given and in Section 4.4.2 and 4.4.3, model validation for rain and snow type precipitation and estimated geophysical parameters are presented.

4.4.1 Measurement System: Phase Tilt Weather Radar (PTWR) Specification

An X-band dual polarization Phase Tilt Weather Radar (PTWR) shown in Figure 4-14 was developed by The Microwave Remote Sensing Laboratory (MIRSL) at the University of Massachusetts and deployed as a fixed roof installation on a building at the University of Texas Arlington, during the Spring of 2014 [60]. The aim of this effort is to improve the dual polarized, low-cost weather radar network and provide more accurate detections of low altitude wind, tornado, hail, ice, and flash flood hazards [60]. One basic advantage of the PTWR is electronic scanning in the azimuth plane and mechanical scanning in the elevation plane.

The PTWR measurement data for an evening severe thunderstorm passing over Fort Worth, TX area was taken on 3 April 2014. The PTWR is positioned in the northwest direction and illuminates a $90°$ sector. For this measurement the maximum radar range is 45 km. It used a 20 μs/3 MHz non-linear frequency modulated waveform that gave 60 m range resolution with 3 km blind range [60]. Table 4-1 shows the PTWR system specifications given by Orzel [61]. The PTWR system operated in the volume scan mode, and collected data at five different elevation angles 2, 6, 8, 10 and 12°. Since the PTWR was installed in proximity to the CASA XUTA X-band radar, the radar outputs of these two ground–based radars were compared to see PTWR observational capabilities [61].

Published results by Orzel showed that PTWR, which is a low-power low-cost radar, provided good performance in the detection of severe weather observation at close range.

Figure 4-14 PTWR set up on a roof in Spring 2014 [60].

Table 4-1 PTWR system specifications

Peak Power	60 W
Frequency	9.36 GHz
Beam width (azimuth/elevation)	1.8-2.6° /3.6°
Range resolution	60 m
Range coverage	45 km
Radar elevation angle	2° -18°
Sector	90°
PRF	2000-3000Hz
Pulse width	20 μs
Blind Range	3 km

4.4.2 Model Validation with Rain Data

The measured reflectivities by PTWR for the thunderstorm passing over Fort Worth, TX area on April 3th, 2014 is given in Fig. 4-15 [60,61,63]. On the azimuth plane, PTWR used 91 beams, from 285° to 15°. For model validation purpose the chosen beam 345° shown as profiler A (see Fig.4-15).

To construct the latent range reflectivity profile for profiler A, totally 2048 range gates were used. After remove the range gates for blind zone and transmit wave form, remaining 1765 range gates were used to construct the profile from 3 km to 45.36 km for each beam. Therefore, each gate length is equal to 24 m which means that every pixel of data in Fig. 4-15 corresponds to reflected power from the volume of length equal to 24m. For profiler A, as seen from Fig. 4-15, precipitation only occurs between 15 and 30 km since the range gates are 10 km apart,

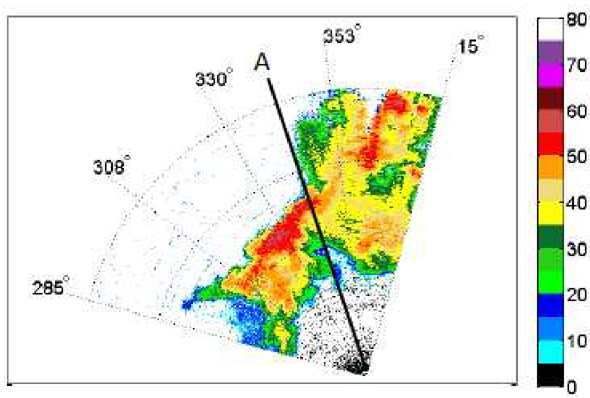

Figure 4-15 The measured reflectivities by PTWR for the thunderstorm passing over Fort Worth, TX area on April 3th, 2014 published by Orzel [60]

Since data has taken for the 6° radar elevation angle, and the melting layer is around 5 km from the ground, the radar beam barely reach the frozen layer within the maximum coverage range 45 km according to the range height relation given by Eq.(4.1). This is seen from Fig. 4-16. However, for profiler A, there is no precipitation detected beyond the 30 km range as seen from Fig.4-15. So, in the validation, melting layer is not taken in to account, and pure rain precipitation is used in the calculation of reflectivities. To decrease simulation time, each range gate is approximated as a sublayer with the length was 40 m in the simulations. To cover the range from 15 to 30 km totally 375 sublayers are used. Each sublayer is characterized by a set of parameters based on the geophysical parameters of precipitation with respect to the rain rate. Within the each sublayer raindrops are modelled as spheres, and Mie scattering theory for closely packaging medium is applied for calculation of the individual phase matrix for each sublayer. Then, the matrix doubling method is used to solve VRT equation to account for multiple scattering and the attenuation effect. Finally, calculation of the normalized backscattered cross-section for each sublayer is explained in Section 4.2 in this chapter.

By following measured data, for closer ranges, parameters are constructed with respect to low rain rates. Gradually increasing of the drop size and volumetric water fraction causes higher reflectivities at the range gates located at the core of the precipitation column. For the range gates located at the farther distances, we start to decrease the drop size with increasing altitude. Also, we decrease the dielectric constant of rain for higher parts of the beam due to water permittivity at 20℃ is 62.84-i31.61 while it is 55.89-i37.84 at 10℃ temperature (See Figure 4-16).

Estimated parameters for pure rain precipitation is summarized in Table 4-2 and model validation is shown in Fig. 4-17. Moreover, instead of the pure rain precipitation, if melting hail is considered estimated parameters to fit model results with the measure data are presented in Table 4-3.

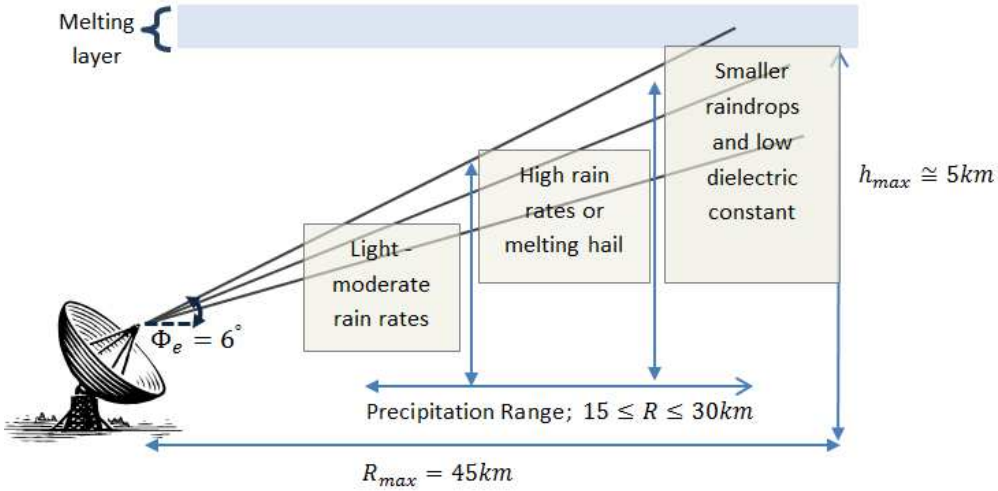

Figure 4-16 Modelling of the radar beam considering range, height and measured reflectivity profile by PTWR

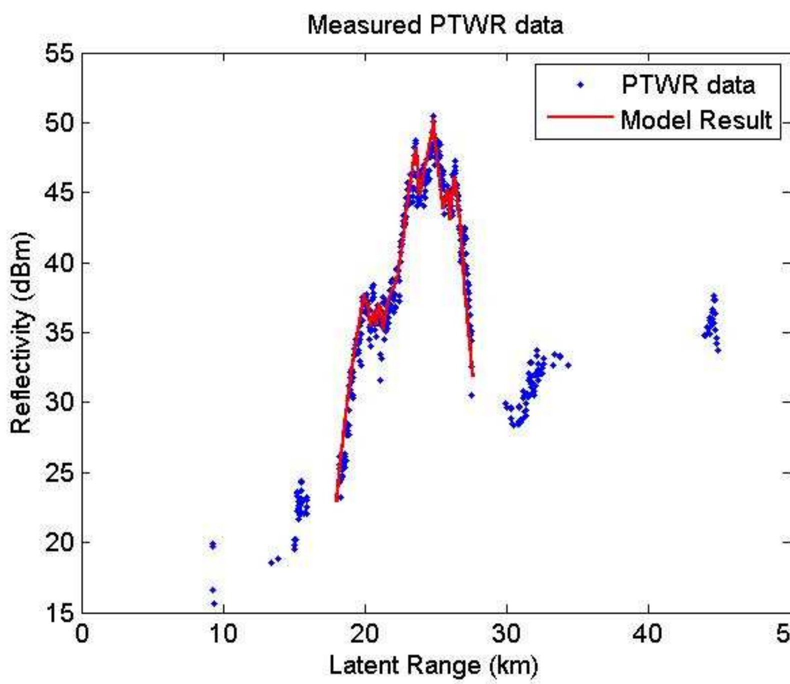

Figure 4-17 Model validation with PTWR data taken on April 3th, 2014 [63]

Table 4-2 Estimated parameters considering pure rain type precipitation

Frequency (GHz)	Rain drop diameter (mm)	Average volume fraction of water	Dielectric Permittivity
9.36 GHz (X Band)	D_{R_min}=0.4 mm D_{R_max}=2 mm	0.050e-5 < Vf < 1.5e-5	$\epsilon_w \approx$ 58.47+i36.09

Table 4-3 Estimated parameters considering rain/wet hail mixed precipitation

Frequency	Rain drop diameter	Wet hail drop diameter	Water fraction of hail	Hail dielectric permittivity
9.36 GHz (X Band)	D_{R_min} =0.4 mm D_{R_max} =2 mm	D_{H_min} =1.25 mm D_{H_man}= 3.4 mm	f_w =0.4-0.8	various values between $\epsilon_h \approx$ 36.40+i29.74 and $\epsilon_h \approx$17.41+i12.59

4.4.3 Model Validation with Snow Data

Model validation for snow type precipitation is provided by comparing model predictions with data collected by the PTWR on 02/13/2014 in Hadley, Massachusetts. The PTWR system is transportable dual polarized weather radar, and it is fixed on a truck to perform snow measurement.

In the measurement system, the total range is 20.85 km and each range gate is 24 m, but in the model, 50 m range gate is used to decrease computational time; a total of 400 range interval is used to simulate 20 km range for the elevation angles 4, 6, 8, 10 and 12°. Measured reflectivities are shown in Fig. 4-18(a), (b), (c), (d), (e) for five elevation angles. Snow drops are modelled as spherical scatterers and volume scattering phase matrices for each range interval is calculated by Mie scattering. Figure 4.19 (a), (b), (c), (d) show calculated reflectivities for 4, 6, 8 and 10° elevation angles respectively. For a lower elevation angle, in Fig.4-19 (a) and (b), reflectivities first increase up to 25 dB in the 0-5 km range, and then, at around 10 km radar range, the slight curve indicates increasing volume fraction and snow densities with smaller size around 1 km altitude. For the higher elevation angle, in Fig.4-19 (c) and (d), the radar beam reaches up to same altitude in closer range and maximum reflectivities occur around the 5-7 km radar range. Increasing elevation angle decreases the radar range from 20 km to 15 km, because the signal is completely attenuate after 2 km altitude due to the higher extinction coefficient.

The model parameters that give the best fit with measurements are summarized in Table 4-4. For the snow reflectivities around 30 dB, snow rate from melted water content is estimated around 1 to 1.5 mm/h by the empirical Z-R relations derived from geophysical parameters of snow, explained in Section 4.2.2. Moreover, according to records of National Weather Service (NWS), a winter storm warning for this event has been issued and stated that snowfall rates could reach as high as 1 to 2 inches per hour. For 1 inch snowfall actually means 1.2 mm /h snow rate in terms of melted water content and for this rate, estimated drop diameters values up to 1.64 mm are reasonable and agree well with the previous studies as given in Figure 4-10.

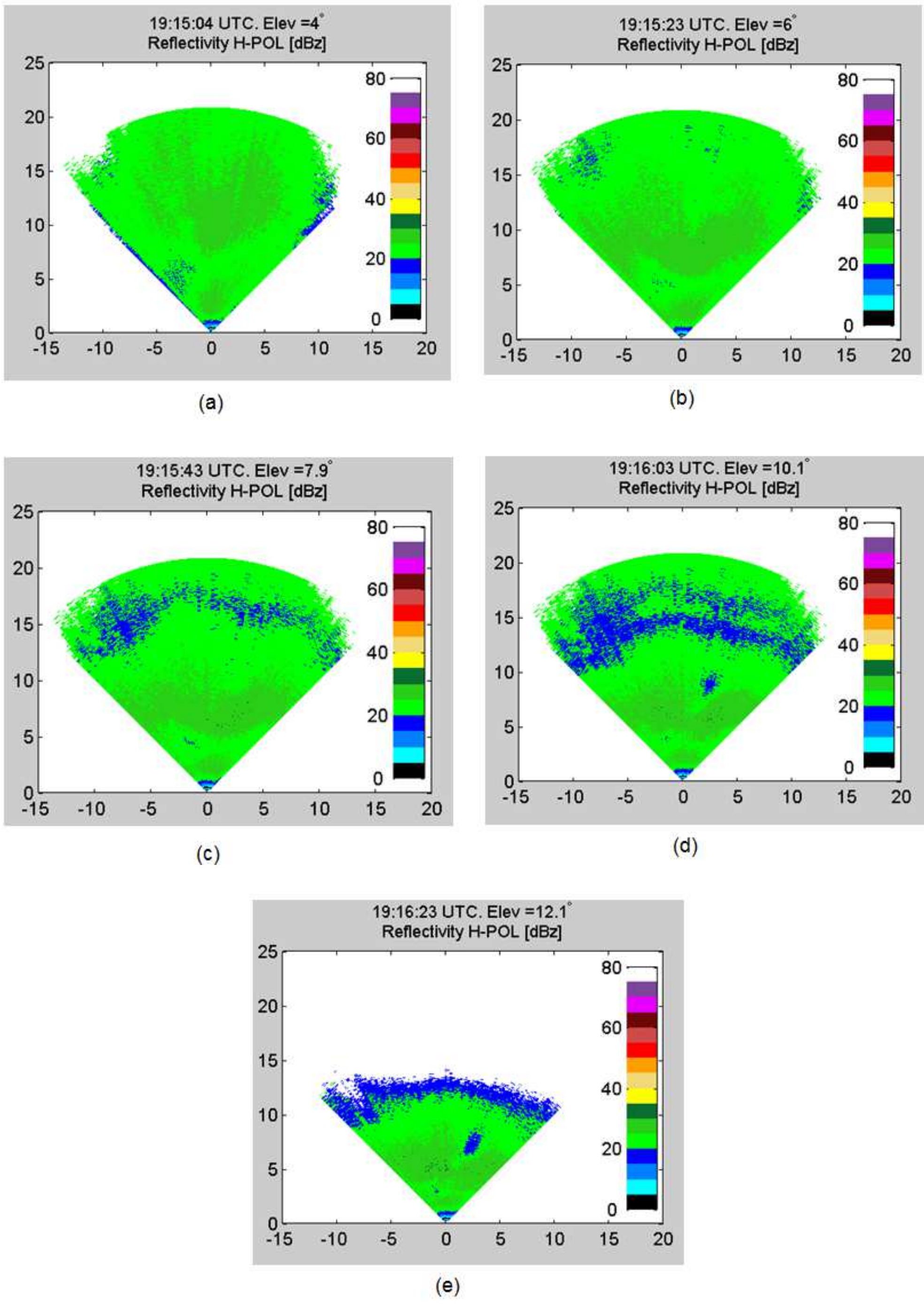

Figure 4-18 Measured data by PTWR on 02/13/2014 in Hadley, Massachusetts

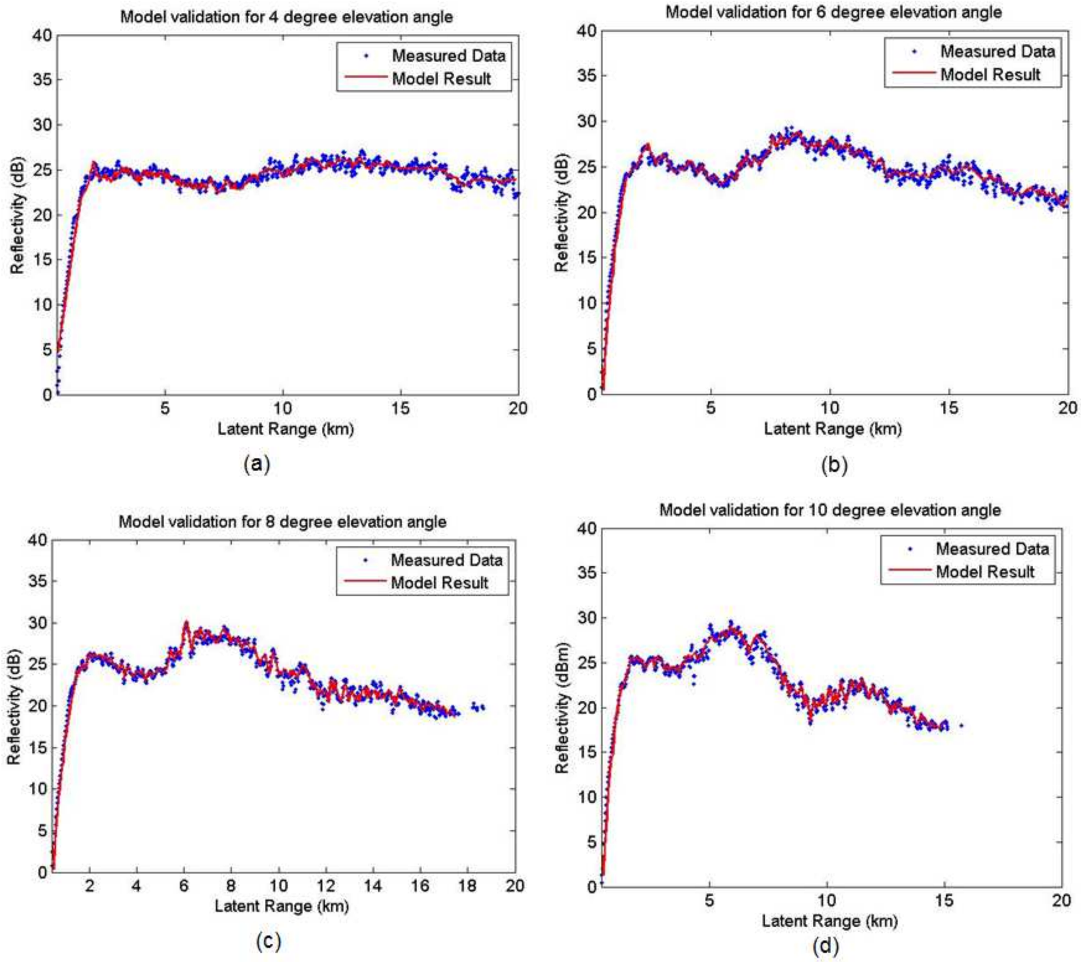

Figure 4-19 Model validation with PTWR snow measurements on 02/13/2014 in Hadley, Massachusetts [63]

Table 4-4 Estimated parameters for snow validation

Frequency	Snow drop diameter	Snow density	Snow fraction of volumes
9.36 GHz (X Band)	D_{s_min}=0.7 mm D_{s_max}=1.62 mm	ρ_w =0.3-0.6 gr/cm^3	0.40e-6 < Vf_s < 1.08e-6

Chapter 5

Multilayered VRT Model Analyses

The multilayered VRT backscattering model analyses for rain, hail and snow type of precipitation using ground-based and spaceborne radar system is important to understand the connection between geophysical parameters of precipitation and backscattering measurements. In this chapter, the VRT model is analyzed in terms of the geophysical parameters of precipitation considering space borne and ground-based measurement systems.

5.1 VRT Model Analyses for Spaceborne Remote Sensing Data

Backscattering from an inhomogeneous rain column is calculated by a multilayered VRT model with respect to surface roughness, drop size, drop shape and volume fraction. Pure rain type precipitation from the ground up to 4 km height is used. In the multilayered VRT model, the rain column is partitioned into 12 sublayers to simulate its vertical profile, and each sublayer is characterized by a set of parameters. Sublayer volume scattering phase matrices are constructed using either Mie scattering or the T-matrix approach to show the effect of the shape of the drops.

Three different types of rain are analyzed; 10 mm/h (widespread), 20 mm/h (shower), 50 mm/h (thunderstorm). The average volume fraction and vertical profile of raindrop radius are calculated using the gamma DSD, as explained in Chapter.3, and given in Table 5-1 and Figure 5-1, respectively.

Table 5-1 Chosen rain rates and average volume fractions

Rain Type	Rain Rate	Average volume fraction
Widespread	10 mm/h	0.65 e-5
Shower	20 mm/h	0.80e-5
Thunderstorm	50 mm/h	1.20e-5

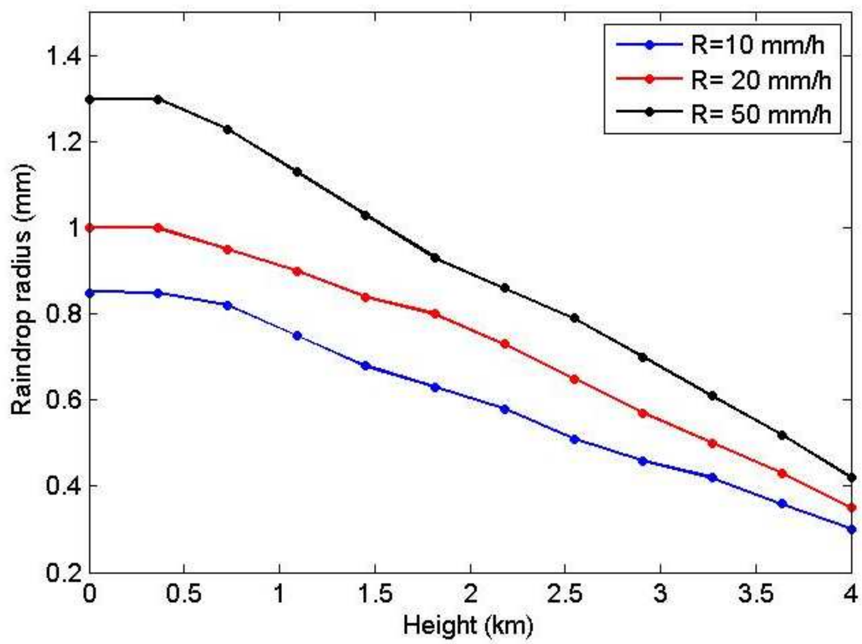

Figure 5-1 Vertical profiles of the raindrops for 10, 20 and 50 mm/h rain rates

As a first case, the effect of sea surface roughness to the backscattered data is investigated by using 4 different combinations of $k\sigma$ and kL as given in Table 5-2. All other analyses parameters are the same, as given in Table 5-2. Figure 5-2 shows VV and HH polarized normalized radar cross (NRCS) sections for rain. In Fig.5-3, direct surface scattering from the sea surface is plotted.

Table 5-2 Surface analyses parameters for VRT model

Rain rate (mm/h)	Volume fraction	Sea surface parameters	Frequency (GHz)	Raindrop permittivity	Chord Ratio (CR)
20	0.80e-5	(a) $k\sigma$=0.3, kL=3.8 (b) $k\sigma$=0.9, kL=3.8 (c) $k\sigma$=0.3, kL=6 (d) $k\sigma$=0.9, kL=6	13.6 (Ku-Band)	ε =51-i36.6	$CR = 1$

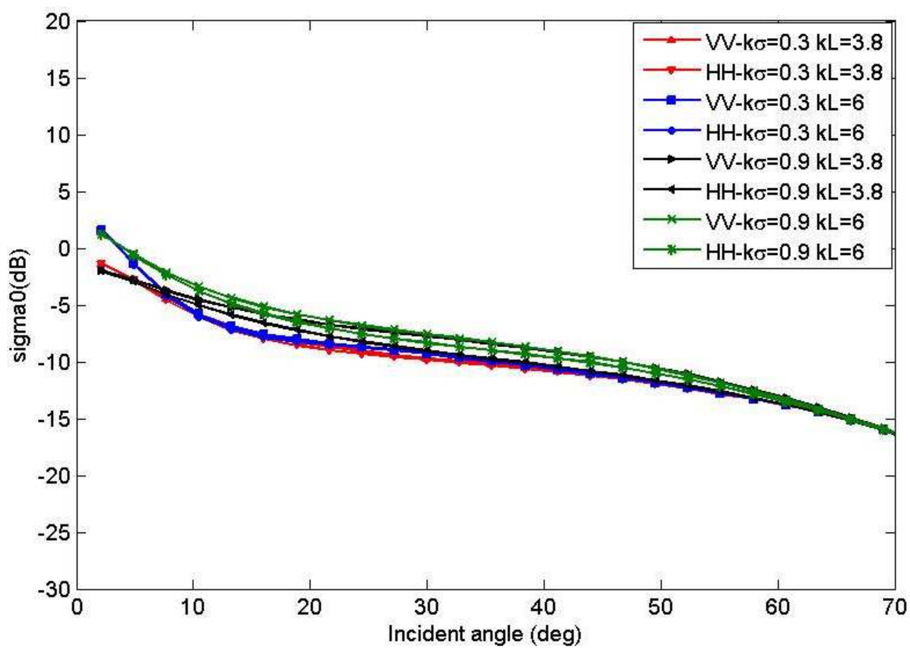

Figure 5-2 VV and HH normalized backscattering cross sections in the case of rain

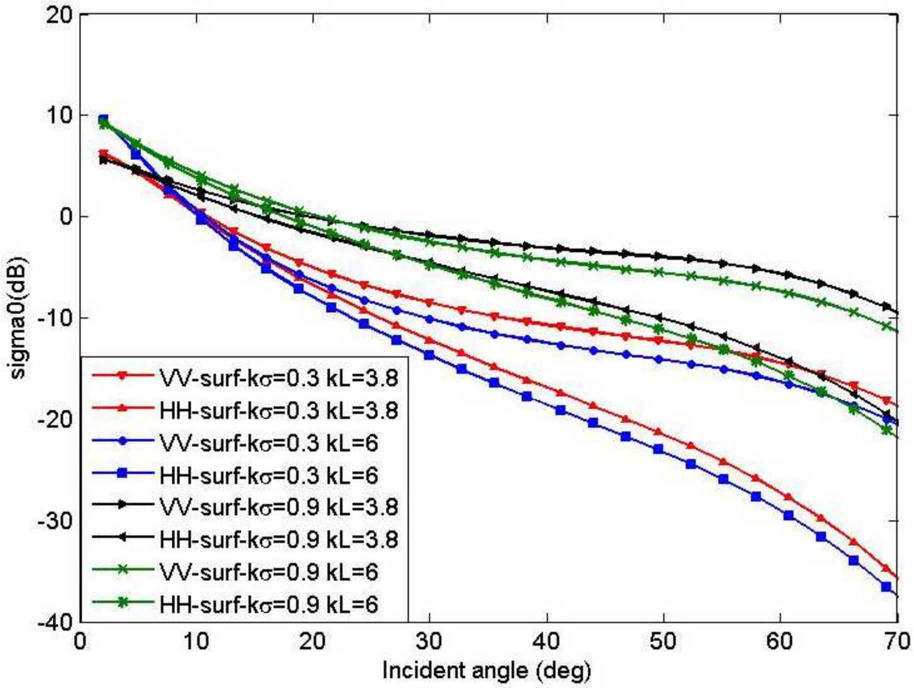

Figure 5-3 Direct surface scattering

For direct surface scattering, as seen from Fig 5-3, there is an increase in the correlation length, kL, for the same rms height, $k\sigma$, or decreasing $k\sigma$ for the same kL causes faster drop-off on the VV and HH curves. This occurs with larger angles due to increasing smoothness of the surface. This is expected, because for smoother surfaces, the coherent component has higher magnitude for small angles, and it falls off faster with larger angles. In Figure 5-2, for small angles the same pattern is seen. However, for larger angles considered surface roughness parameters make no difference in terms of both VV and HH components of the NRCS. This analysis shows that for small incident angles surface scattering for large incident angles, volume scattering is dominant on the backscattering data.

To see the effect of precipitation to the NRCS, three different rain rates; 10 mm/h, 20 mm/h and 50 mm/h are investigated with corresponding vertical drop size profiles and volume fractions as given in Table 5-1 and Figure 5-1. All other parameters are given in Table 5-3. As seen from Figures. 5-4 and 5-5, increasing the volume fraction and drop radius causes higher NRCS for larger incident angles due to higher volume scattering coefficients, however for small angles, surface scattering is the main factor and for smaller rain rates it is dominant.

Table 5-3 Model parameters for rain rate analyses

Rain rate (mm/h)	Average volume fraction	Sea surface parameters	Frequency (GHz)	Raindrop permittivity	Chord Ratio (CR)
10	0.65e-5	$k\sigma$= 0.3 kL= 3.8	13.6 (Ku-Band)	$\varepsilon=$ 51-i36.6	CR=1
20	0.80e-5				
50	1.20e-5				

For the same rain rate the effect of frequency is examined by using C, X and Ku band frequencies for the same rain rate and surface roughness, as given in Table 5-4. Analyses results, shown in Figures 5-6, 5-7 and 5-8 for C-, X- and Ku band respectively, imply that the effect of rain precipitation on the NRCS for small incidence angles is more significant at higher frequency i.e. Ku- Band whereas it is negligible for small frequency i.e. C-Band. As a result, it is obvious that the detection of precipitation for 20 mm /h at C-Band impractical due to much larger wavelength with respect to particle size.

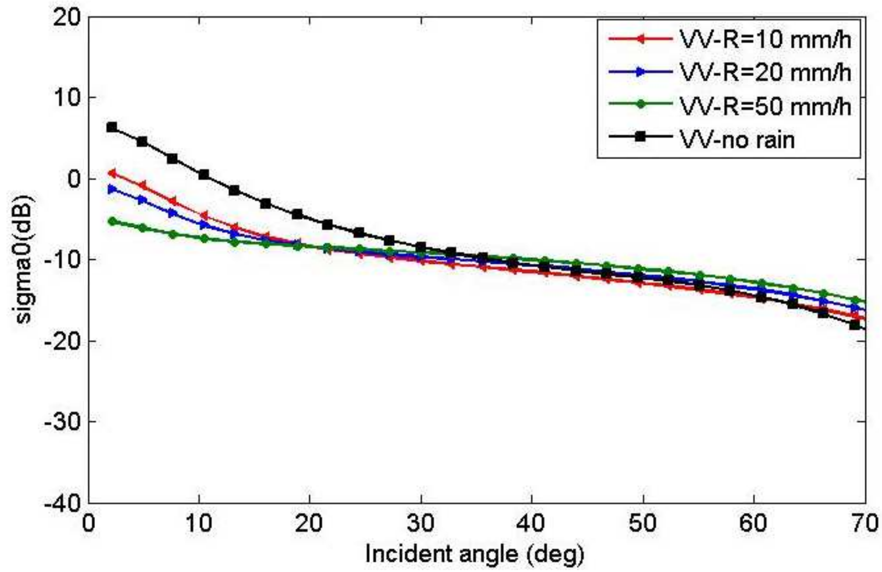

Figure 5-4 VV components of NRCS for the rain rates 10, 20 and 50 mm/h

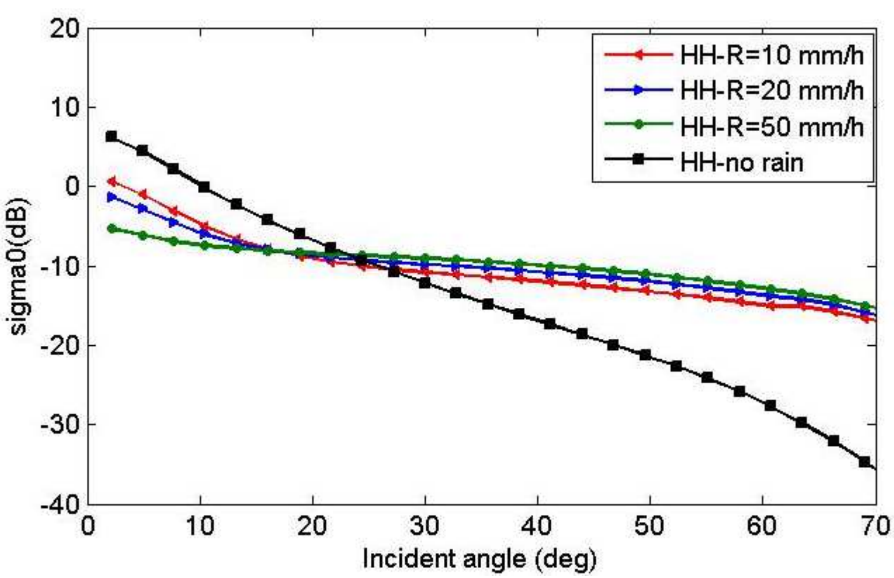

Figure 5-5 HH components of NRCS for the rain rates 10, 20 and 50 mm/h

Table 5-4 Model parameters for frequency analyses

Rain rate (mm/h)	Average volume fraction	Sea surface parameters	Frequency (GHz)	Raindrop permittivity	Chord Ratio (CR)
20	0.80e-5	$k\sigma$ =0.3 kL =3.8	5.3 (C-Band)	ε =73-i21.2	CR=1
			9.36 (X – Band)	ε =62-i31.6	
			13.6 (Ku-Band)	ε =51-i36.6	

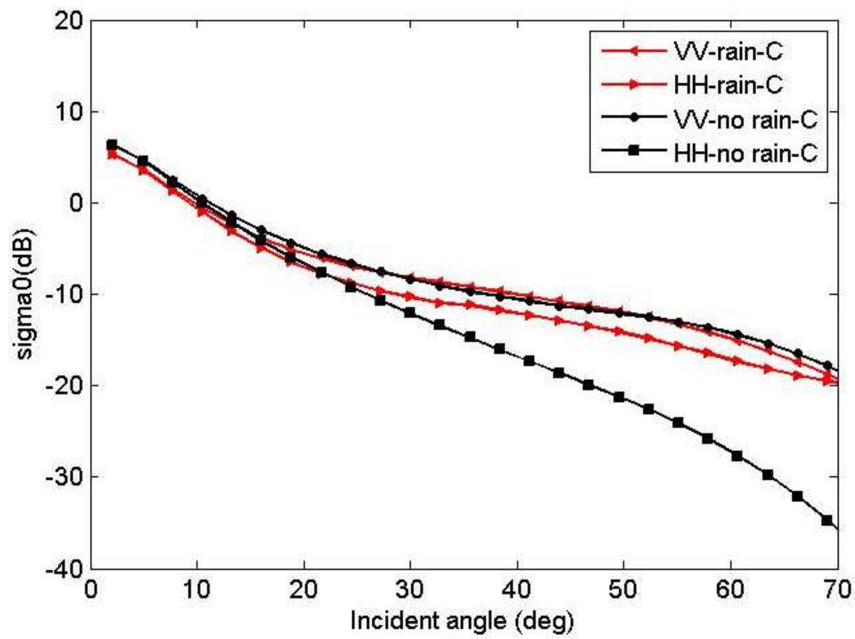

Figure 5-6 Effect of rain precipitation with rate 20 mm/h at C band

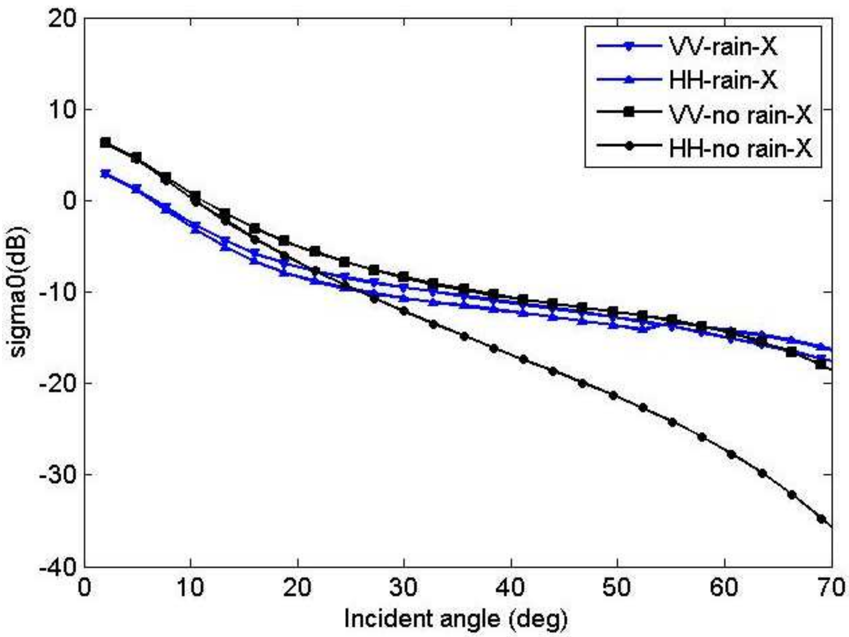

Figure 5-7 Effect of rain precipitation with rate 20 mm/h at X band

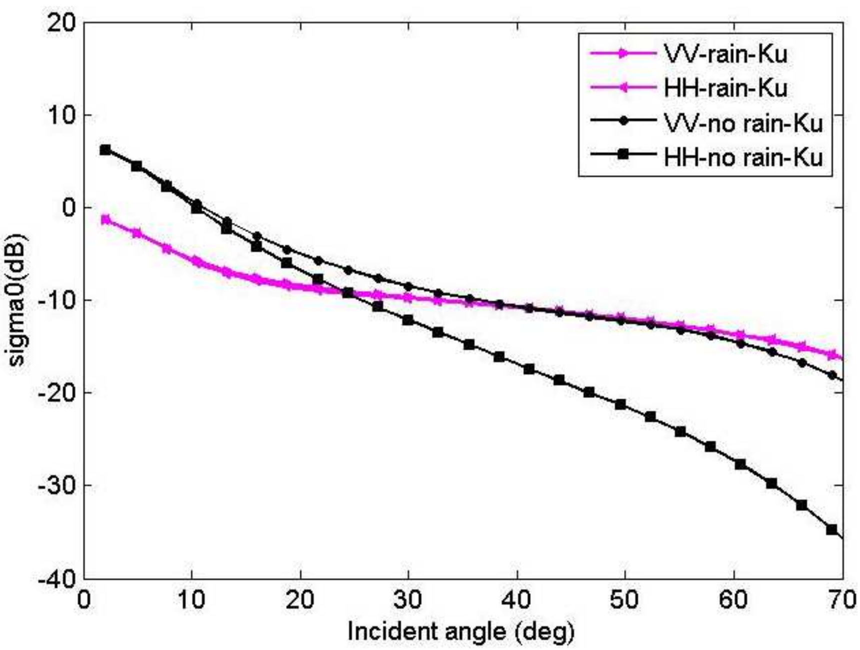

Figure 5-8 Effect of rain precipitation with rate 20 mm/h at Ku band

To see only the effect of the drop size variation to the backscattering data for the same rain rate and volume fractions, 20 mm/h rain rate is used at Ku-Band with volume fraction of 0.80e-5. The reference drop radius vertical profile is given in Fig. 5-1 for 20 mm/h rain rate. For smaller and larger drop size profiles are constructed by decrease and increase drop radius around 0.2 mm with the same volume fraction, since rain rate is assumed is same.

Results shows that both VV and HH polarized NRCS for bigger drops are higher at larger incident angles, whereas smaller VV and HH appear for bigger drops at small incident angles as seen from Figures 5-9 and 5-10. The reason behind that is the precipitation is the main factor effecting the backscattered data at large incidence however, for small incidence sea surface has much more impact.

For the different rain rates, it is possible to see different volume fractions for same size drops caused by vertical variations of drop sizes. To analyze the effect of volume fractions to the NRCS, model parameters are given in Table 5-5. The volume fraction analysis is given in Figure 5-11, which indicates that the higher volume fraction causes lower backscattering cross section due to the loss factor of rain precipitation.

Table 5-5 Model parameters for volume fraction analyses

Rain rate (mm/h)	Average volume fraction	Sea surface parameters	Frequency (GHz)	Raindrop permittivity	Chord Ratio (CR)
10	0.65e-5	$k\sigma$ =0.3	13.6	ε =51-i36.6	CR=1
40	1.00e-5	kL =3.8	(Ku-Band)		

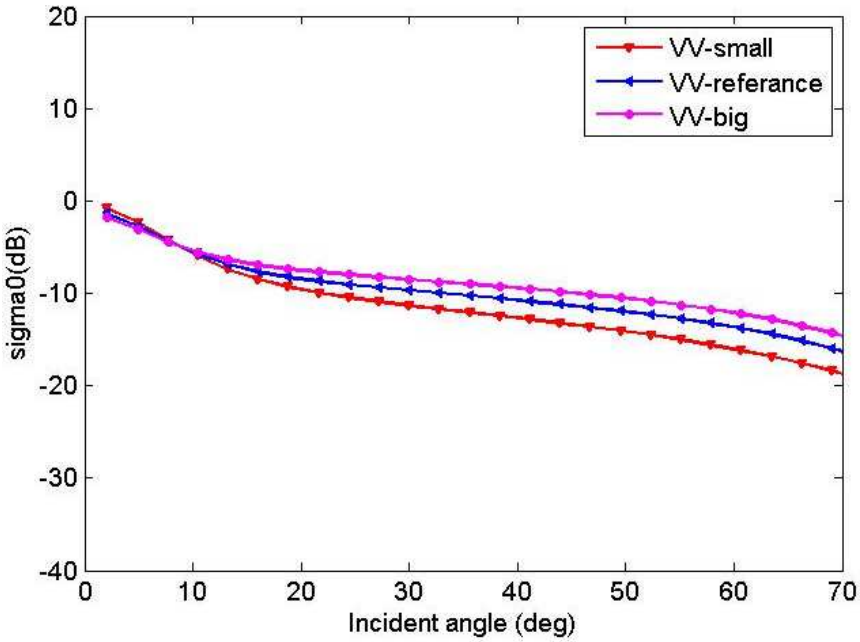

Figure 5-9 VV polarized NRCS for small, reference and big drop sizes

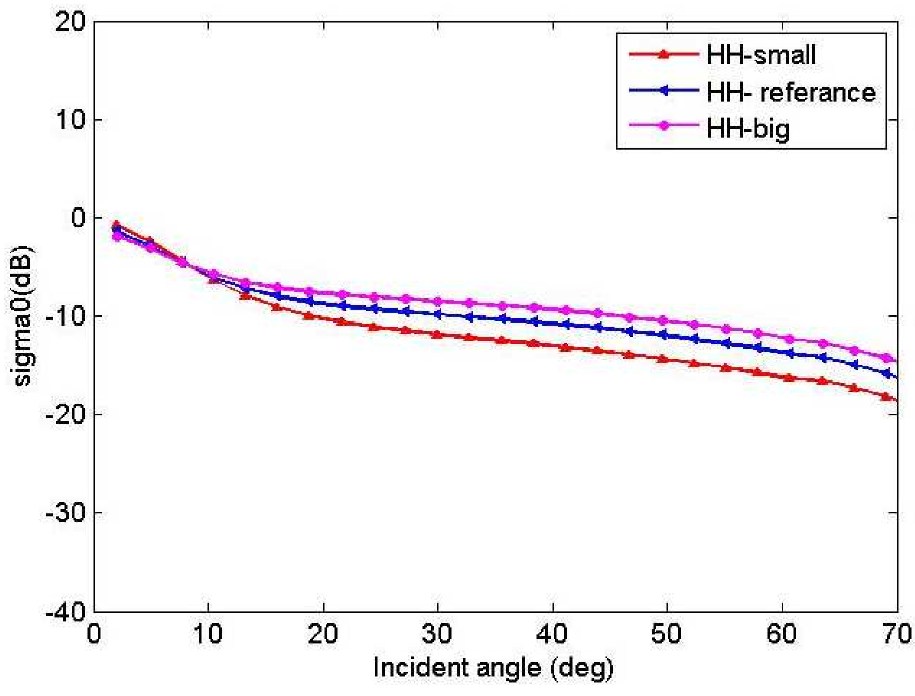

Figure 5-10 HH polarized NRCS for drop size analyses

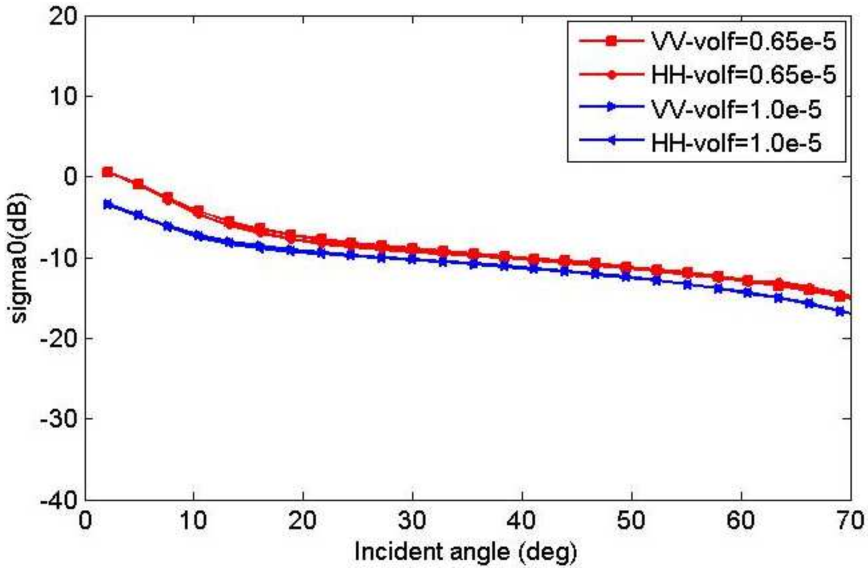

Figure 5-11 Volume fraction analyses

The effect of drop shape to the NRCS is analyzed for 20 and 50 mm/h rain rates using C- band and Ku-band wavelengths. The related volume fractions are given in Table 5-1 and other parameters i.e. surface roughness and drop permittivities with respect to chosen frequency are shown in Table 5-4. Figures 5-12 and 5-13 show the oblique shape effect by increasing the chord ratio up to 1.8 for 20 mm/h rain rate at C-band and Ku band respectively. Similarly, in Figures 5-14 and 5-15, for the same frequency and chord ratio is used, yet 50 mm/h rain rate is used to illustrate the shape effect to the NRCS in the case of larger size drops. As seen from the figures, for the high rain rate due to bigger sizes of drops, the oblique shape effect is more obvious at Ku-band because the wavelength for this frequency is small enough to resolve more shape details.

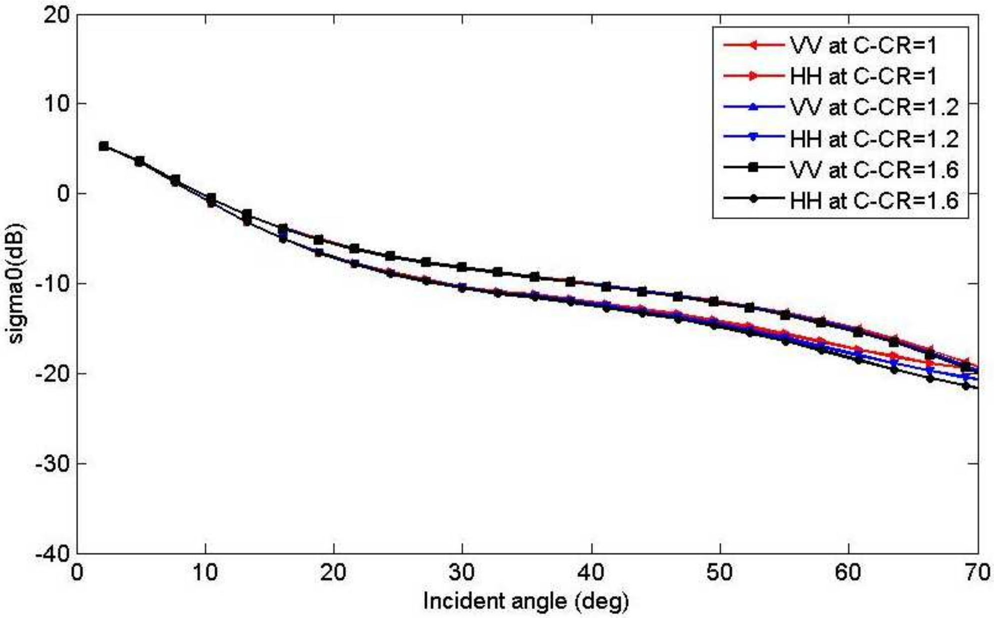

Figure 5-12 Shape analyses for 20 mm/h at C band

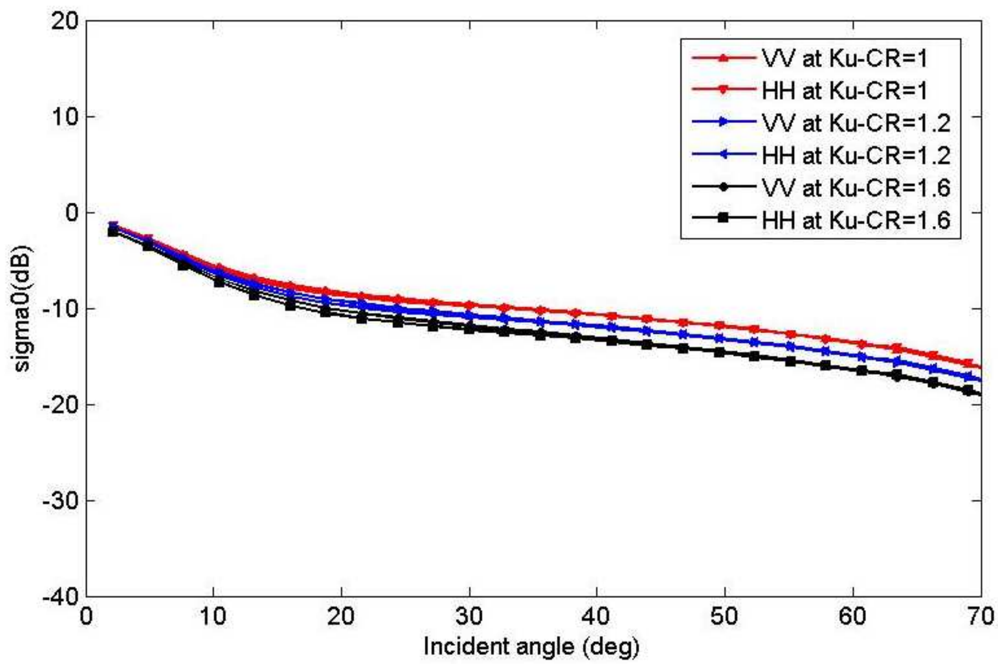

Figure 5-13 Shape analyses for 20 mm/h at Ku band

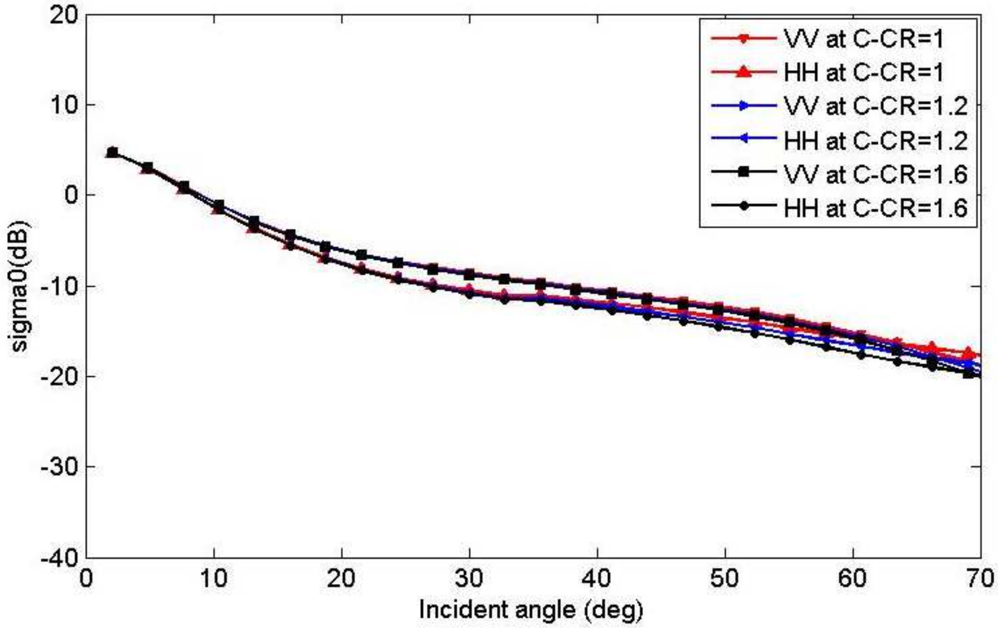

Figure 5-14 Shape analyses for 50 mm/h at C band

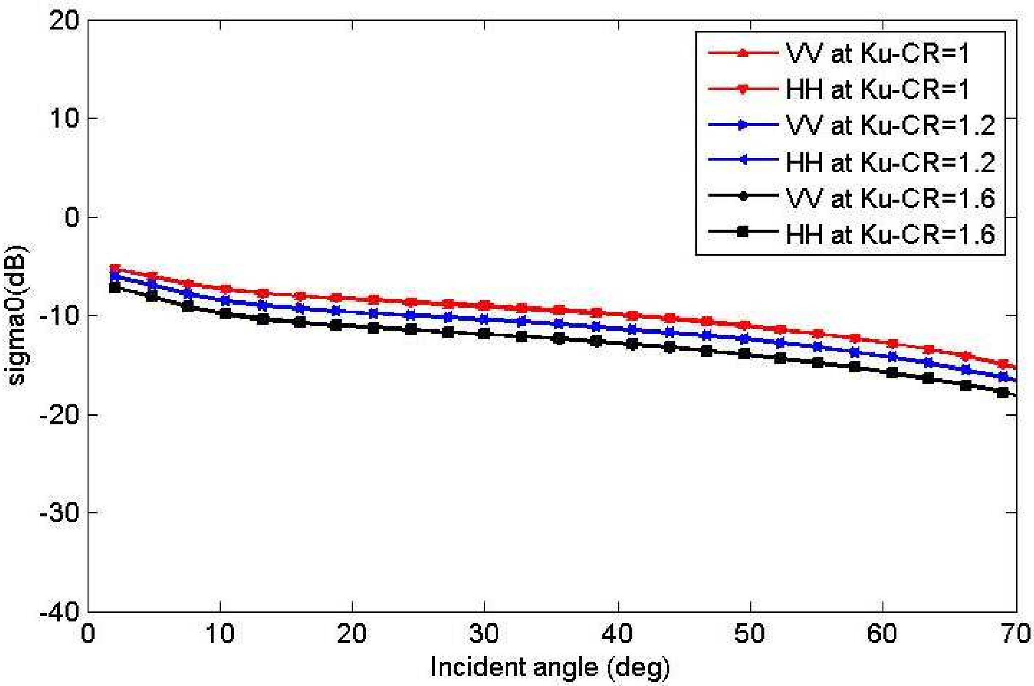

Figure 5-15 Shape analyses for 50 mm/h at Ku band

5.2 Ground-Based Radar VRT Model Analyses

5.2.1 Model Comparison with Rayleigh Approximation and Mie Scattering

In Section 5.1, multiple layered VRT model is examined with respect to rain rate, drop size, volume fraction and drop shape for spaceborne remotely sensed data. In this section, a ground based VRT model is developed, analyzed and compared with the Rayleigh and Mie approximations to see multiple scattering effects on the reflectivity. The ground based VRT model validation with PTWR measurements and estimated parameters for the rain, wet hail and snow precipitation are given in Chapter 4. In this section, traditional Mie scattering which is based on independent scattering approach and Rayleigh approximation performances are investigated using estimated parameters by VRT model given in Chapter 4.

For the rain data validation given in Figure 4-17, in Chapter.4, the limits related with physical and electrical parameters of rain i.e. drop size, volume fraction, dielectric permittivity are shown in Table 4-2. In this section, Figures 5-16 and 5-17 show the constructed range profile of the rain drop diameters and volumetric water fractions used in model validation given by Figure 4-17. Constructed range profiles of drop sizes and volume water fractions, and dielectric permittivities are used in the Rayleigh Approximation and Mie scattering to compare them with the VRT multiple layered model. This comparison is given in Figure 5-18. In this figure, it is obvious that in closer range, for small diameters and volume fractions, three models give similar results. However for increasing diameters up to 2 mm with higher volume fractions, the Mie scattering and Rayleigh approximation give a similar pattern of drop size. Especially, in the Rayleigh approximation as explained in Chapter.4, reflectivity is calculated from the sixth power of the diameters and so, for larger diameters it is significantly overestimated the measured data up to 10 dB for the same parameters. In the Mie scattering, estimated reflectivities are much closer than Rayleigh approximation to the measurements. However for larger volume fractions and sizes, due to multiple scattering and attenuation effects, which are not taken into account in Mie scattering, estimated reflectivities are higher than measurements up to 5 dB.

For the same reflectivity data in Figure 4-17 in Chapter.4, if wet hail is assumed instead of pure rain type precipitation, used parameters to provide best fit with the measurements are given in Table 4-3. The range profiles of the size of wet hail drops and water fractions are given in the in Figures 5-19 and 5-20. It can be seen from Figure 5-19, diameters of hail drops are increased with latent range up to 3 mm. On the other hand, the dielectric permittivity is decreasing with range due to ice core with water shield at higher altitudes as given in Table 4-3. Therefore, the decreasing reflectivities are due to decreasing water permittivity of precipitation and volume fraction of water for higher altitudes. Increasing size and loss factor for wet hail causes much larger difference between the Rayleigh approximation, Mie scattering and the VRT model as seen from Figure 5.21.

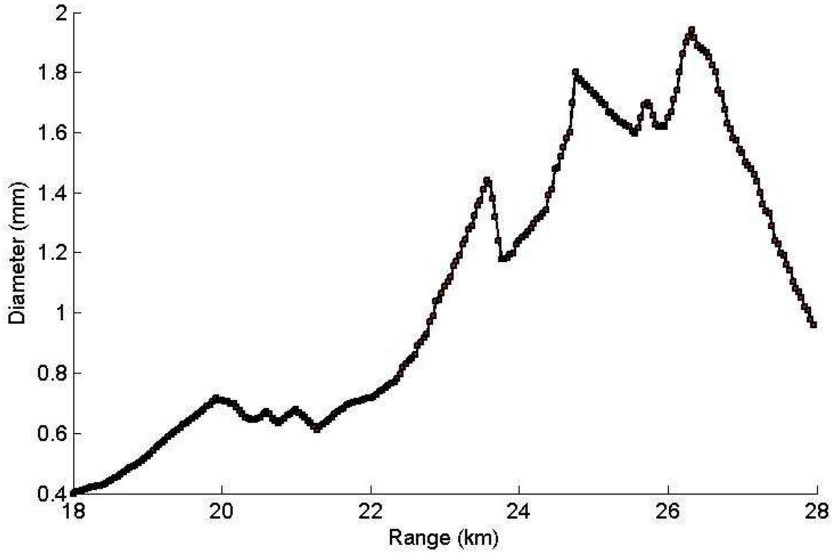

Figure 5-16 Estimated drop diameters for PTWR rain measurement

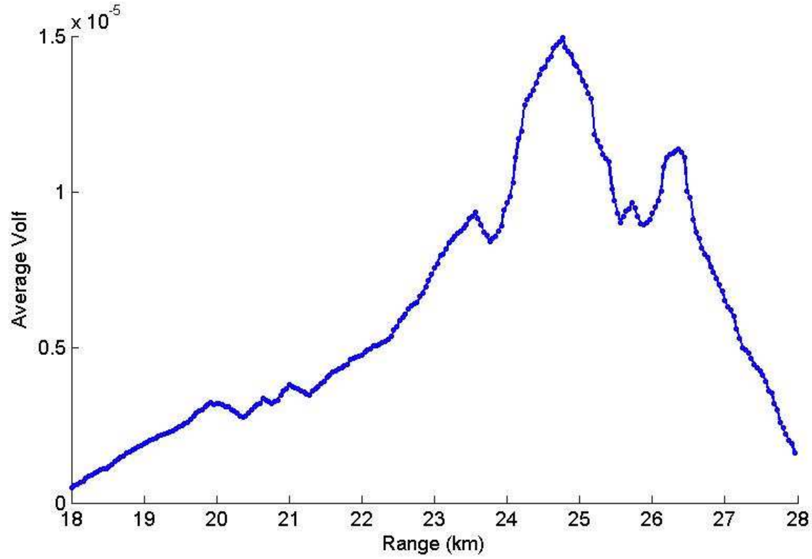

Figure 5-17 Estimated volume fractions for PTWR rain measurement

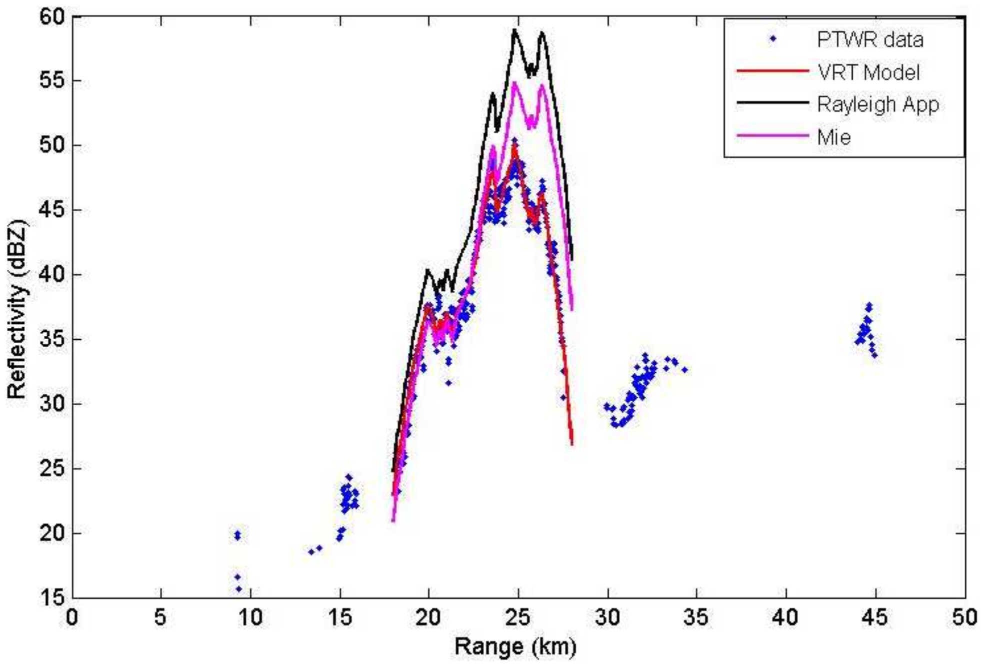

Figure 5-18 Comparison between the VRT model, Rayleigh Approximation and Mie scattering using PTWR data for rain type precipitation

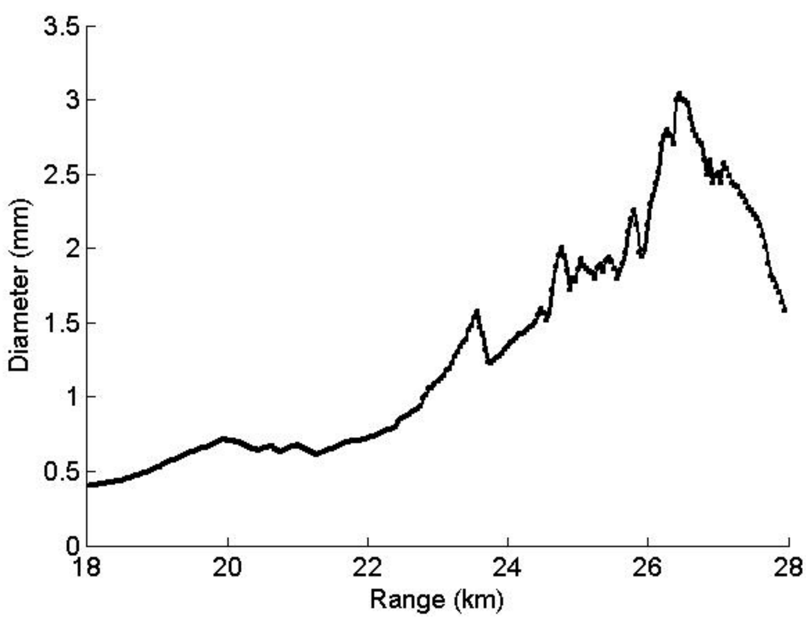

Figure 5-19 Estimated drop diameters in the presence of wet hail in rain column

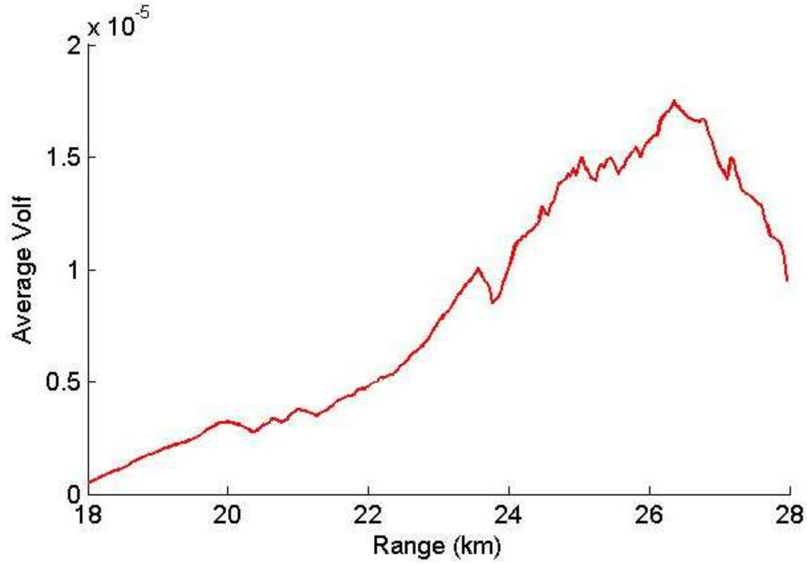

Figure 5-20 Estimated volume fractions in the presence of wet hail in rain column

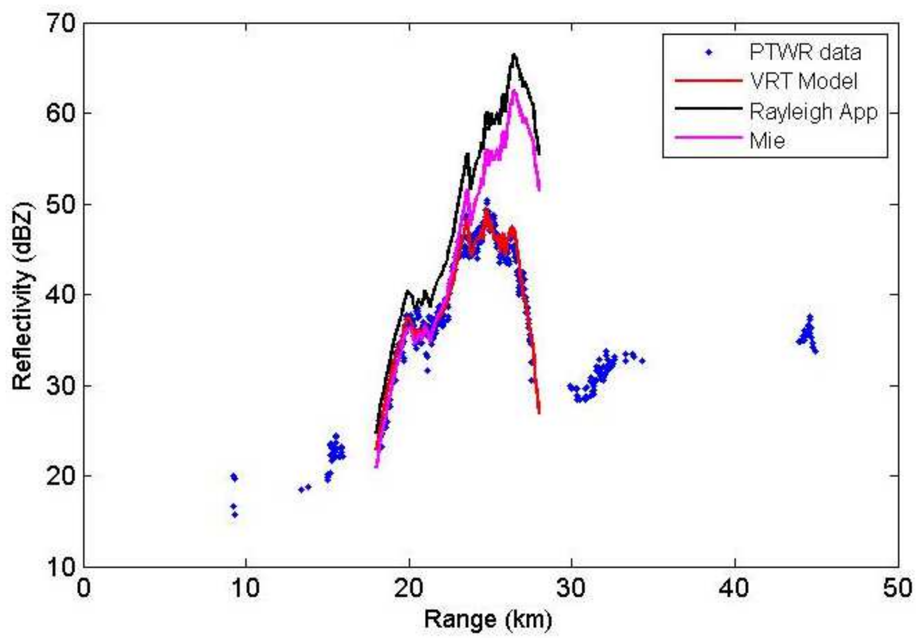

Figure 5-21 Comparison between the VRT model, Rayleigh Approximation and Mie scattering using PTWR data for wet hail type precipitation

5.2.2 T-matrix Approach in the Ground-Based VRT Model

Besides Mie scattering theory for closely spaced scatterers, T-matrix approach is also used in the multiple layer VRT model to take into account the obliquity of larger size rain drops. For oblique spheroid type scatterers, since spherical symmetry is not valid, calculated backscattering cross sections and reflectivities are polarization dependent as explained in Chapter 4, Section 4.3.2. Therefore, for scatterers which are oblique in shape, the ratio of the h-polarized reflectivity to the v-polarized reflectivity is known as the differential reflectivity, Z_{dr} which is given by Eq. (4.42). For the reflectivity data measured by PTWR given in Figure 4-17 in Chapter.4, calculated reflectivities, Z_h and differential reflectivities, Z_{dr} by the T-matrix approach used inside the multiple layer VRT model are given in Figures 5-22 and 5-23, respectively. Also, estimated parameters related this analysis is given in Table 5-6. As explained in Section 4.3.2, the computed Z_{dr} values are relatively lower than expected for the chord ratios up to 1.3. The reason behind it is that all the scattering and incident directions are used to account for all the interaction between scatterers in the calculation of volume scattering phase matrices. Moreover, this process increases computational time significantly.

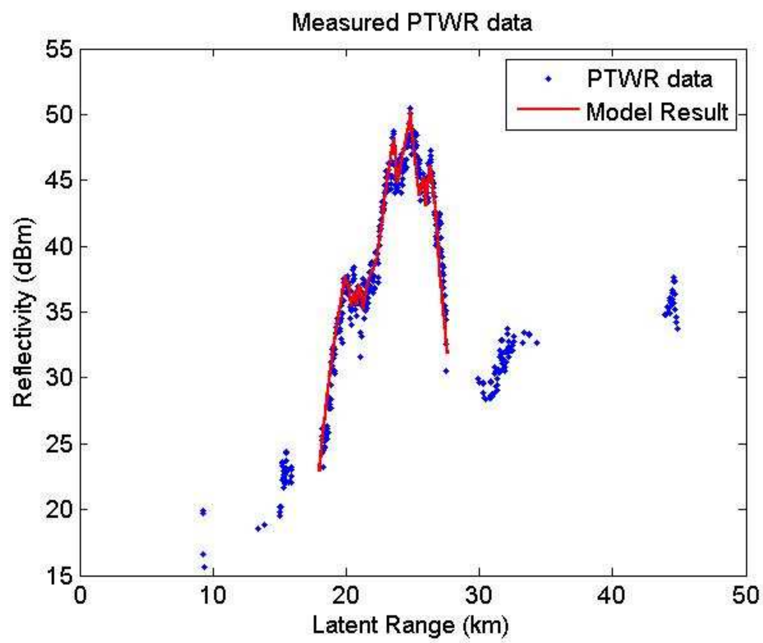

Figure 5-22 Calculated reflectivities, Z_h by T-matrix approach in the VRT model

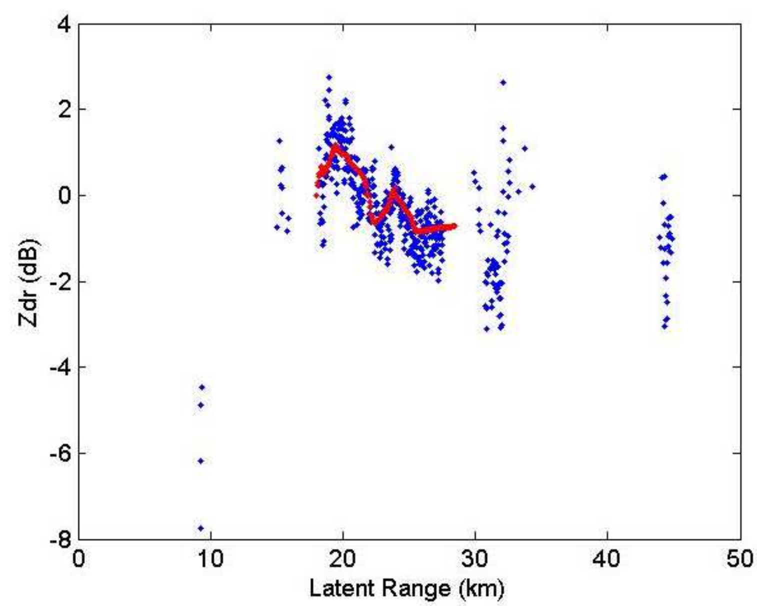

Figure 5-23 Calculated differential reflectivities, Z_{dr} by T-matrix approach in the VRT model

Table 5-6 Estimated parameters for the T-matrix calculation for the data measured by PTWR

Frequency (GHz)	Rain drop diameter (mm)	Average volume fraction of water	Dielectric Permittivity	CR
9.36 GHz (X Band)	D_{R_min}=0.4 mm D_{R_max} = 2 mm	0.050e-5< Vf < 1.5e-5	$\epsilon_w \approx$ 58.5+i36	0.8 – 1.3

5.2.3 Model Analyses for Different Types of Rain

In this section, the multiple layered ground based VRT model is analyzed for different types of rain to examine the effect of rain rate to the reflectivities. In Figure 5-24 shows the calculated reflectivities for shower type of rain with the rain rate up to 11 mm/h. For this calculation, frequency is 9.36 GHz, and the dielectric permittivities of water, ε_w is varied in the range 62.84+i31.61 $\leq \varepsilon_w \leq$ 44.85+i41.54. Totally 240 range gate are used to simulate reflectivities from 18 to 28 km. Constructed range profile for rain drop diameter and volumetric water fractions are given in Figure 5-25. From Fig.5-25, it can be seen that the maximum drop diameter, for 11 mm/h rain rate is estimated around 1.3 mm which is also agreed with empirical models developed for rain rate estimation as explained in Section 3.2.

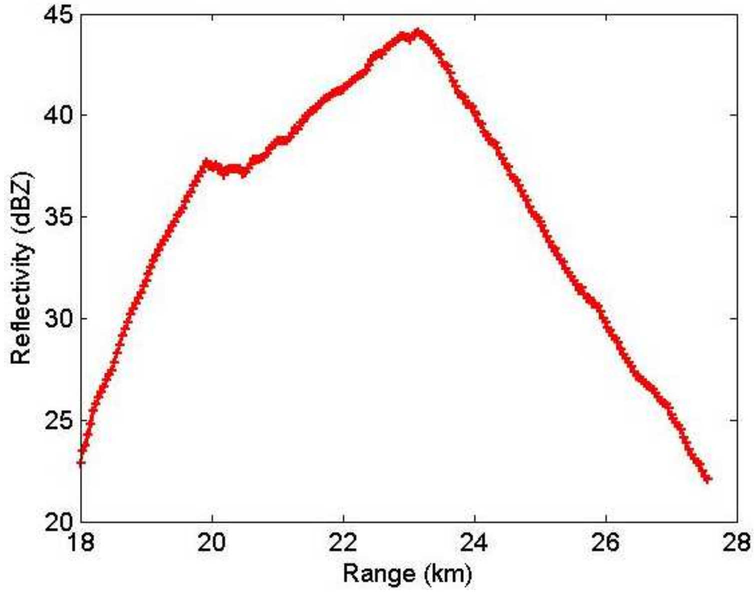

Figure 5-24 Calculated reflectivities for shower type rain

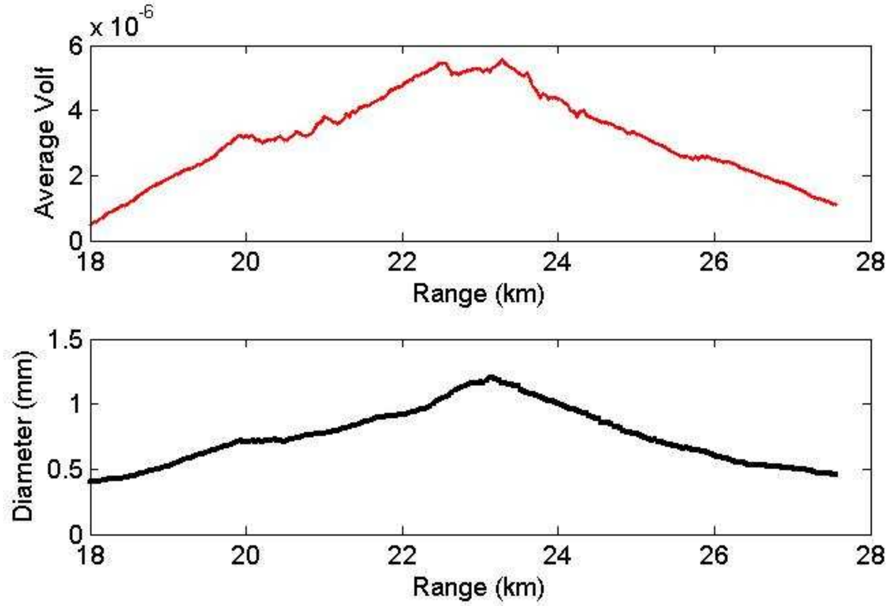

Figure 5-25 Constructed range profile for rain drop radius and volumetric water fractions

for shower type of rain

Similarly, for a thunderstorm rain, calculated reflectivities are given in Figure 5-26 for the same frequency and dielectric permittivity range. Estimated range profiles for drop radius and volume water fractions are shown in Figure 5-27. For thunderstorm type of rain, the maximum drop diameter is estimated around 2.8 mm and volume fraction of water is much higher than shower type of rain, as expected.

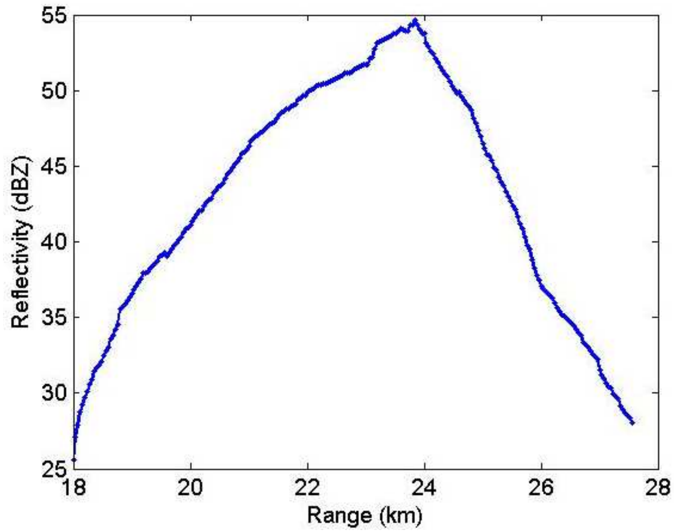

Figure 5-26 Calculated reflectivities for thunderstorm type rain

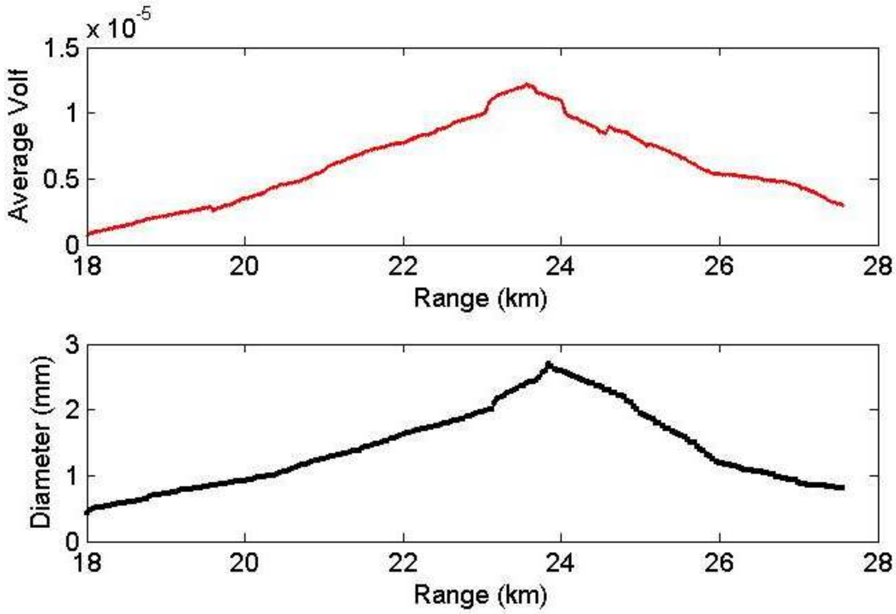

Figure 5-27 Constructed range profile for rain drop radius and volumetric water fractions for thunderstorm type of rain

5.2.4 Model Analyses for Snow Rates

In this section, the multiple layered ground based VRT model is analyzed for 1 mm/h and 2.5 mm/h snow rates in terms of melted water content. According to the empirical model developed by Gunn and Marshal or Sekhon and Srivastava, for dry snow precipitation, the reflectivity–snow rate relation is given by Figure 4-9. Similarly, the median snow drop diameters with respect to rain rates are shown in Figure 4-10. In X-band, for 1 mm/h snow rate, calculated reflectivities by using the multiple layers VRT model is given in Figure 5-28. For this analyses constructed range profile of snow parameters are given in Figure 5.29. Similarly, for 2.5 mm/h snow rate calculated reflectivities and corresponding range profiles are given in Figure 5.30 and 5.31. For both rain rates, snow densities are around 0.3, in closer ranges, and for increasing distance higher density snow drops with smaller diameters are used. The range between 0-15 km is divided 150 range gates. In Figures 5-28 and 5-30, slight curve after 7-8 km indicates denser medium with higher volume fraction of snow and smaller diameter, as expected. For 1 mm/h snow rate, calculated reflectivities are up to 30 dB with the snow drop diameter is maximum 1.7 mm. Similarly, for 2.5 mm/h snow rate, maximum snow diameter is around 2.2 mm which causes reflectivity around 40 dB. Note that for a typical snow precipitation, the measured reflectivities are around 30-35 dB. However, 2.5 mm/h snow rate in terms of melted water content indicates really strong snow storm and resulting reflectivities up to 40 dB are agreed with previous empirical studies.

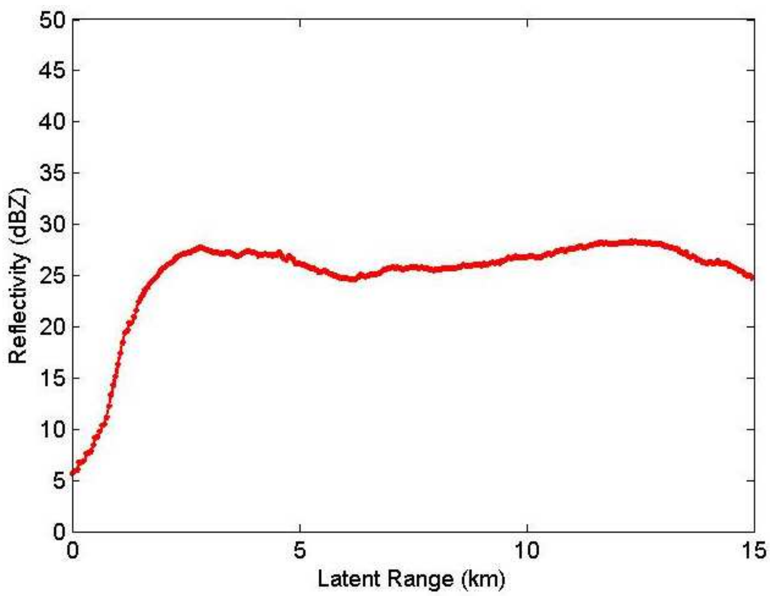

Figure 5-28 Calculated reflectivities using the VRT model 1 mm/h snow rate

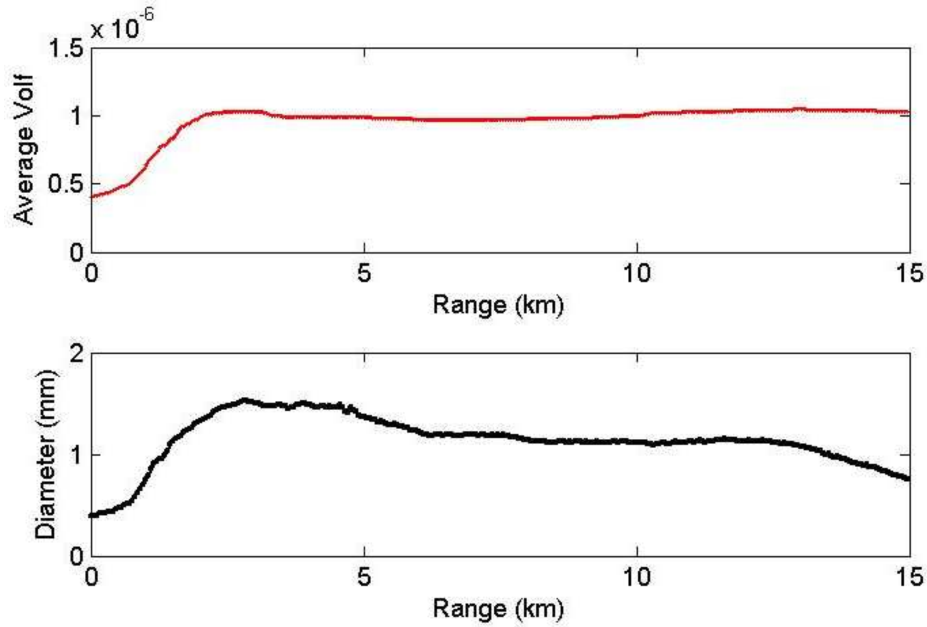

Figure 5-29 Range profile of snow diameters and volume fractions for 1 mm/h snow rate

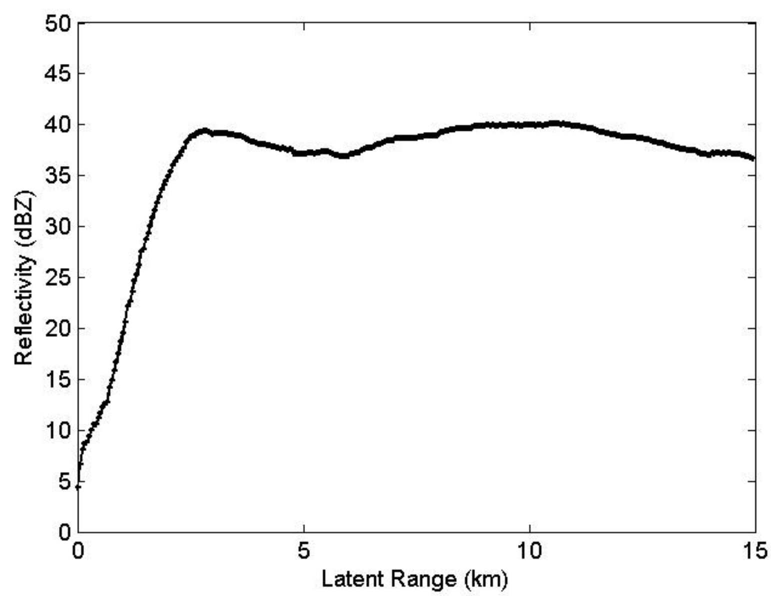

Figure 5-30 Calculated reflectivities using the VRT model 2.5 mm/h snow rate

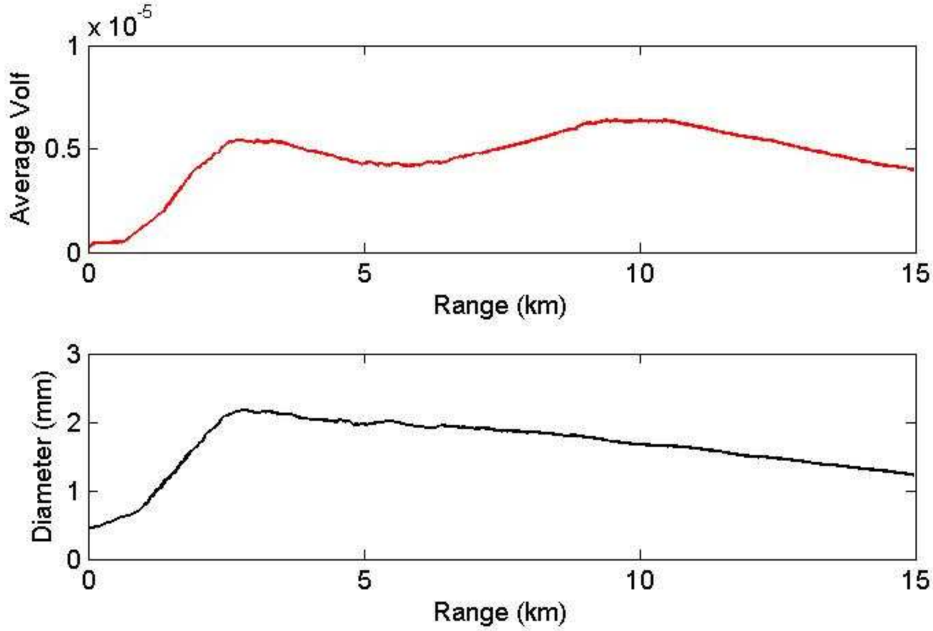

Figure 5-31 Range profile of snow diameters and volume fractions for 2.5 mm/h snow rate

Chapter 6

Conclusion and Recommendation

A geophysical microwave backscattering model for space borne and ground-based remote sensing of precipitation was used to analyze backscattering measurements from rain and snow type precipitation. Both spaceborne and ground based measurement system geometries were considered for the calculation of the backscattered wave.

In previous studies, this model was applied to calculation of backscattering from a rain column on a sea surface by using Mie scattering theory for closely spaced scatterers. Model analyses results were compared with the TRMM data, and they agreed well. In this study, besides Mie scattering theory, the T-matrix approach is used in the multiple layer VRT model. This is allowed us to examine shape effects of the raindrops to the backscattered wave.

In this study, the VRT model is modified for the calculation of reflectivities from precipitation hydrometeors received by a ground-based radar system. Backscattered reflectivities from each unit range of volume are calculated considering backscattering radar cross section and effective illuminated area of the radar beam. The overall aim of applied the multiple layered VRT model is to construct a range profile for the geophysical and electrical parameters of the precipitation hydrometeors and to calculate reflectivities by taking into account multiple scattering effect and attenuation loss. Model comparisons with simplified assumptions show that the multiple scattering and attenuation effect may cause up to 10 dB differences for rain or wet hail type precipitation with high intensity.

In the model, if the Mie scattering theory is used for the calculation of volume scattering phase matrices, the differential reflectivity calculation was not provided since the scatterers in spherical symmetry. However, by using the Mie scattering theory inside the VRT model, the scattering and extinction cross sections are calculated directly from expansion coefficients, and they are independent from the incident and scattering directions which decreases computational time and makes the model more practical.

To take into account polarization effect and differential reflectivity calculation by VRT model, the T-matrix approach is used inside the VRT model for nonspherical scatterers. However, since in the VRT model incident and scattering angles are in all directions, computation of scattering and extinction cross sections are significantly increase the computational time simply due to increasing summations with the number of range units. Moreover, calculated differential reflectivities are lower than measurements even for highly oblate spheroid raindrops due to averaging all over the scattering angles (θ_s,φ_s).

In the future studies, constructed range profiles of the physical parameters of hydrometeors from the multiple layer VRT model can allow building up a semi empirical Z- R relation using a statistical model. This relation will also take into account multiple scattering and attenuation effects, and provide a more practical calculation for reflectivities directly from the given rain rates. However, to construct such a relation, model should be tested with several measured data set for various types of rain or snow precipitation.

Appendix A

A Microwave Backscattering Model for Rain Column

(Double-click PDF object to open full paper)

A MICROWAVE BACKSCATTERING MODEL FOR RAIN COLUMN

Seda Ermis and Saibun Tjuatja

Wave Scattering Research Center, Department of Electrical Engineering

The University of Texas at Arlington UTA Box 19016, Arlington, TX 76019-0016, USA

Email: seda.ermis@mavs.uta.edu

ABSTRACT

A combined T-matrix algorithm and vector radiative transfer layered precipitation model has been used to analyze scattering from rain column. The raindrop is modeled as spheroid with complex permittivity. The phase matrices for differential layers rain-drop scattering within the rain column are computed using the T-matrix approach, and backscattering from the entire rain column that accounts for multiple-scattering and boundary interactions are determined by solving the vector radiative transfer equations. Model analyses and some data comparisons were conducted at Ku-Band using published measured/observed parameters. Results show that model predictions agree well with published TRMM measurements. More extensive model validation and analyses will be provided in the full paper.

INTRODUCTION

Recently, observations of precipitations (both rainfall and snowfall) taken by high resolution scatterometers have been able to directly use in many areas such as hydrology and water cycle, heat evaluation or climate studying [1]. However, existing rainfall estimation methods are inherently subject to various source of error because of the underlying model assumptions. Important effects of precipitation such as contribution from layers in rain column or changing surface roughness are highly related to its physical parameters [1]. In this paper, a backscattering model for rain column based on a combined T-matrix algorithm and vector radiative transfer (VRT) method is presented. The model and parameters used in this study are introduced in Section 1. The analyses results are presented in Section 2. Finally, summary and conclusions are given in Section 3.

RAIN COLUMN SCATTERING MODEL

Raindrop keeps its perfect spherical shape in the absence of external or internal forces such as hydrostatic force due to fluid flow or, electrostatic force [1]. When it is falling, its shape becomes flattened oblate spheroid. This shape can be modeled by a chord ratio, which is the ratio of the height to the width of the raindrop [1].

In [2], an inhomogeneous layered model with a different set of parameter for each sublayer is considered to simulate scattering from rain column with vertical profile, and Mie scattering is used to model raindrop scattering, i.e. the rain drop is model as perfect sphere. Since a falling raindrop deviates in shape from spherical, becoming flattened oblate spheroid, we propose the use of T-Matrix method to model raindrop scattering in

Appendix B

A Microwave Backscattering Model for Hail-Rain Mixture Precipitation

(Double-click PDF object to open full paper)

A MICROWAVE BACKSCATTERING MODEL FOR HAIL-RAIN MIXTURE PRECIPITATION

Seda Ermis and Saibun Tjuatja
Wave Scattering Research Center, Department of Electrical Engineering
The University of Texas at Arlington UTA Box 19016, Arlington, TX 76019-0016, USA
Email: seda.ermis@mavs.uta.edu

ABSTRACT

A rain column model is used analyze back scattering from precipitation in the presence of hail. Backscattering from the entire precipitation column comprising hail and rain that accounts for multiple-scattering and boundary interactions are determined by solving the vector radiative transfer (VRT) equations. Precipitation column is partitioned into sublayers and Mie scattering calculation is used to determine phase matrix for differential layers consist of hail stones and rain drops. The raindrops and hail stones are represented by using spherical shaped scatterers. Microphysical properties of rain and hail such as shape, composition and size distribution are considered in the model. Results from model analyses agree well with published measurement results.

INTRODUCTION

Distinguishing ice and water precipitation by remote sensing is a long-standing problem in meteorology [1]. This is especially challenging in a convective storm where water can exist at temperature below 0^{o} and ice can be found at temperature above 0^{o} [1]. Convective storms can produce large hail and heavy rain which leads to flash flooding or crop hail damage. Quantitative estimation of hail and rain rate by obtaining accurate backscattering information affords us a better means for estimating environmental and economic impacts of severe hailstorms. Although polarimetric radar measurements help improve quantitative estimates of liquid and solid form of precipitation, there are some difficulties in developing procedure to deduce dominant hydrometeor types from polarimetric measurements. Some of them are the lack of through understanding of radar signature of specific hydrometeor type, the need for information about size and characteristic of hydrometeor, the ambiguities in hydrometeor identification, or the errors about radar calibration, and attenuation in the presence of hail [2]. To overcome these difficulties, radar signature characteristic of hail embedded in rain column may help radar meteorologists to make it distinguish in the observations from polarimetric radar.

In previous works, a combined T-matrix VRT or Mie VRT layered precipitation model was used to analyze scattering from rain column [3,4]. The purpose of this paper is to construct a model for accurate quantitative estimation of backscattering data from rain-hail mixture precipitation and to provide better understanding of the effect of microphysical parameters of rain and hail such as shape, composition, and size distribution to the backscattering data. This paper is organized as follows. The model description is given in the first part. The model analysis is explained in the second part. Finally, results and future goals are stated in the last part.

MODEL DESCRIPTION

Appendix C

A Microwave Scattering Model for Ground-based Remote Sensing of Snowfall and Freezing Rain

(Double-click PDF object to open full paper)

A MICROWAVE SCATTERING MODEL FOR GROUND-BASED REMOTE SENSING OF SNOWFALL AND FREEZING RAIN

Seda Ermis[1], Krzysztof Orzel[2], Saibun Tjuatja[1], Stephen Frasier[2]

[1]Wave Scattering Research Center, Department of Electrical Engineering, The University of Texas at Arlington UTA Box 19016, Arlington, TX 76019-0016, USA
Email: seda.ermis@mavs.uta.edu, tjuatja@uta.edu
[2]Microwave Remote Sensing Laboratory, University of Massachusetts, Amherst, MA 01002, USA

ABSTRACT

A microwave backscattering model for ground-based remote sensing of precipitation is developed and used to analyze back scattering measurements from snowfall and rain type precipitation. Backscattering from entire precipitation region is calculated by solving vector radiative transfer (VRT) equations. Geophysical parameters for rain or snow are determined by considering altitude and latent range. VRT equations are solved numerically by using matrix doubling method to take into account multiple-scattering effects. Results from model analyses agree well with measured radar data.

Index Terms— ***Ground-based radar, snow/rain precipitation, vector radiative transfer model***

1. INTRODUCTION

Accurate analysis and estimation of weather conditions especially for low level of atmosphere, which is the part where most convective storms occurred, are important to reduce the adverse effects due to weather related problems [1]. Ground-based radar systems for the quantitative estimation of precipitation has played crucial role in weather analysis and prediction. To date, backscattering modeling studies for ground-based radar systems focus on low to moderate precipitation rate and ignore the multiple scattering effects [2]. In this study, a backscattering model for ground-based radar systems based on vector radiative transfer (VRT) theory that accounts for multiple incoherent scattering was developed and used to analyze scattering from precipitation. This paper is organized as follows: The model geometry is given in Section 1. The theoretical background of the model is explained in Section 2. Model validation and analysis are presented in Section 3. Finally, summary is given in Section 4.

2. MODEL GEOMETRY

For a radar system, meteorological targets (which composed of a larger number of hydrometeors) can be modeled as randomly distributed scatterers within a sample volume, also known as contribution volume. Within the radar range, the transmitted signal is first scattered by the closest contribution volume and parts of the transmitted energy returns to the radar. The remaining energy is transferred to next contribution volume and same process repeats itself until the signal is completely attenuated. Therefore, scattering from target volume with the radar beam consists of multiple contributing volumes of particles located at different range and height, as shown in Figure. 1. Due to beam spreading effect, contribution volumes at the farther distance cover much more area vertically, from lower to the higher level of atmosphere. In general, a precipitation column consists of ice or dry hail at the top; water droplets, wet hail or wet snow in the middle; and water droplets or snow at the bottom. A scattering/contribution volume may consist of different types of scatterers (e.g. hail and water droplets, snow with different particle sizes). The effective permittivity of a contribution volume with mixed type scatterers can be approximated using Maxwell-Garnett formulas. Using the effective permittivity, a contribution volume is approximated as a homogeneous random medium and backscattering from the volume is determined using VRT [3].

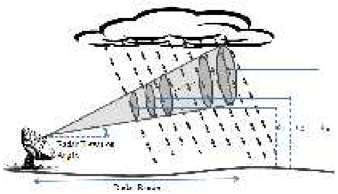

Figure.1 Problem geometry

References

1. Gebremichael, M., Testik, F. Y., Microphysics, measurement, and analyses of rainfall, Rainfall: State of the Science, Geophysical Monograph Series 191, American Geophysical Union, 2010.
2. Michaelides, S., Levizzani, V., Anagnostou, E., Bauer, P., Kasparis, T., Lane ,J.E., Precipitation: Measurement, remote sensing, climatology and modeling, Atmospheric Research, Volume 94, Issue 4, 2009, pp 512-533.
3. Cifelli, R., Chandrasekar, V., Dual-polarization radar rainfall estimation, Rainfall: State of the Science, Geophysical Monograph Series 191, American Geophysical Union, 2010.
4. Battan, L. J., Radar observation of the atmosphere, The University of Chicago Press, 1973.
5. Oguchi, T., Electromagnetic wave propagation and scattering in rain and other hydrometeors, IEEE , vol.71, no.9, Sept 1983, pp.1029-1078.
6. Straka, J. M., Zrnić, D. S., Ryzhkov, A. V., Bulk hydrometeor classification and quantification using polarimetric radar data: Synthesis of relations. J. Appl. Meteor., 39, 2000, pp 1341–1372.
7. Ulaby, F. T., Moore, R. K., Fung, A. K., Microwave Remote Sensing, Vol.3, Addison-Wesley, 1986, Ch. 13.
8. Ulaby, F. T., Moore, R. K., Fung, A. K., Microwave Remote Sensing, Vol.2, Addison-Wesley, 1986, Ch. 12
9. Mishchenko M. I., Travis L. D., Light scattering by polydispersions of randomly oriented spheroids with sizes comparable to wavelengths of observation. Applied optics, 33(30), 1994, pp. 7206-7225.

10. Matrosov, S. Y., Modeling backscatter properties of snowfall at millimeter wavelengths. J. Atmos. Sci., 64, 2007, pp 1727–1736.

11. Ryzhkov, A., Polarimetric radar observation operator for a cloud model with spectral microphysics, Journal of Applied Meteorology and Climatology, 50.4, 2011, pp. 873-894.

12. Ryzhkov, A. V. Kumjian, M. R. Ganson, S. M. Khain A. P., Polarimetric radar characteristics of melting hail. Part I: Theoretical simulations using spectral microphysical modeling. J. Appl. Meteor. Climatol., 52, 2013, pp. 2849–2870.

13. Ulaby, F. T., Long, D. G. Microwave Radar and Radiometric Remote Sensing, University of Michigan Press, 2013.

14. Eom, H. J., Theoretical scatter and emission models for microwave remote sensing, ProQuest Dissertations and Theses, 8301671,1982.

15. Winebrenner, D. P., Ishimaru, A., Application of the phase-perturbation technique to randomly rough surfaces, JOSA A 2.12,1985, pp 2285-2294.

16. Fung, A. K., Li, Z., Chen, K. S., Backscattering from a randomly rough dielectric surface, IEEE Transactions on Geoscience and Remote Sensing, Vol. 30, No. 2, March 1992, pp 356–369.

17. Tjuatja, S., Theoretical scatter and emission models for inhomogeneous layers with application to snow and sea ice, ProQuest Dissertations and Theses, 9301625, 1992.

18. Chandrasekhar, S., Radiative Transfer, Dover, New York,1960.

19. Fung, A. K., Eom, H., J. , A study of backscattering and emission from closely packed inhomogeneous media, Geoscience and Remote Sensing, IEEE Transactions on 5,1985, pp 761-767.

20. Wen, B., Dense medium radiative transfer theory: comparison with experiment and application to microwave remote sensing and polarimetry, Geoscience and Remote Sensing, IEEE Transactions on 28.1, 1990, pp 46-59.
21. Tsang, L., Modeling active microwave remote sensing of snow using dense media radiative transfer (DMRT) theory with multiple-scattering effects, Geoscience and Remote Sensing, IEEE Transactions on 45.4, 2007, pp 990-1004.
22. Howell, H. B., Jacobowitz, H., Matrix method applied to the multiple scattering of polarized light. J. Atmos. Sci., vol. 27, 1970, pp. 1195–1206
23. De Haan, J. F., Bosma, P. B., Hovenier, J. W., The adding method for multiple scattering calculations of polarized light. Astronomy and Astrophysics,183, 1987, pp 371-391.
24. Fung, A. K., Eom, H., A theory of wave scattering from an inhomogeneous layer with an irregular interface, Antennas and Propagation, IEEE Transactions, vol. 29(6), 1981, pp. 899-910.
25. Bohren, C. F., Huffman, D. R., Absorption and Scattering of Light by Small Particles. John Wiley & Sons, 2008.
26. Hulst, H. C., Van De Hulst, H. C., Light scattering by small particles. Courier Corporation, 1957.
27. Waterman, P. C., Matrix formulation of electromagnetic scattering,Proceedings of the IEEE 53.8,1965, pp 805-812.
28. Mishchenko, M.I., Travis, L. D., Andrew A. L., Scattering, Absorption and Emission of Light by Small Particles, Cambridge University Press, Cambridge, 2002.

29. Ryzhkov, A. V., Polarimetric characteristics of melting hail at S and C bands, Preprints, 34th Conf. on Radar Meteorology, Williamsburg, VA, Amer. Meteor. Soc. A. Vol. 4. 2009.

30. Yanovsky, F. J., Braun, I. M., Models of Scattering on Hailstones in X-band, Radar Conference, 2004. EURAD. First European. IEEE, 2004.

31. Aydin, K., Yang, Z., A computational study of polarimetric radar observables in hail, Geoscience and Remote Sensing, IEEE Transactions on28.4, 1990, pp 412-422.

32. Marshall, J.S., Palmer, W.M., The Distribution of Raindrops with Size, J. Metor., Vol. 5, 1948, pp. 165-166.

33. Laws, J.O., Parsons, D.A., The relationship of raindrop size to intensity, Trans. AGU, 24, 1943, pp. 425-460.

34. Ulbrich, C. W., Natural variations in the analytical form of the raindrop size distribution, Journal of Climate and Applied Meteorology 22.10, 1983, pp. 1764-1775.

35. Ulbrich, C. W., Atlas D., Rainfall microphysics and radar properties: Analysis methods for drop size spectra, Journal of Applied Meteorology 37.9, 1998, pp. 912-923.

36. Hong, Y., Gourley, J. J., Radar Hydrology: Principles, Models, and Applications by CRC Press, 2014.

37. Tzeng, Y. C., T-matrix approach to volume scattering simulation (Doctoral dissertation). Retrieved from ProQuest Dissertations and Theses. (Accession Order No. 9301627), 1992.

38. Tsang, L., Kong, J. A., Shin, R. T., Theory of Microwave Remote Sensing, Willey Series in remote sensing, 1985

39. Fung, A. K., Eom H. J., Application of a combined rough surface and volume scattering theory to sea ice and snow backscatter, Geoscience and Remote Sensing, IEEE Transactions on 4, 1982, pp 528-536.
40. Mishchenko, M. I., Hovenier, J. W., Travis, L. D., Light scattering by nonspherical particles: theory, measurements, and applications. Academic press, 1999.
41. Jiamei, L, Tjuatja, S., Dong, X., Parameter analysis of precipitation effects on sea surface scattering, Geoscience and Remote Sensing Symposium (IGARSS), 2012 IEEE International. IEEE, 2012.
42. Mishchenko, M., Light scattering by randomly oriented axially symmetric particles, J. Opt. Soc. Am. A 8, 1991, pp 871-882.
43. Mishchenko , M. I., Travis, L. D., Mackowski, D. W., T-matrix computations of light scattering by nonspherical particles: A review, J. Quant. Spectrosc. Radiat. Transfer, vol. 55, 1996, pp 535-575.
44. Mishchenko M., Light scattering by size-shape distributions of randomly oriented axially symmetric particles of a size comparable to a wavelength, Appl. Opt. 32,1993, pp 4652-4666
45. Mishchenko M. I., Calculation of the amplitude matrix for a nonspherical particle in a fixed orientation, Appl. Opt. vol. 39, 2000, pp 1026-1031
46. Simpson, J., Robert, F. A., Gerald, R. N., A proposed tropical rainfall measuring mission (TRMM) satellite, Bulletin of the American meteorological Society, 69.3 1988, pp 278-295.
47. Liao, L., Meneghini, R., On modeling air/spaceborne radar returns in the melting layer, Geoscience and Remote Sensing, IEEE Transactions on43.12, 2005, pp 2799-2809.

48. Matthew, L., Chandrasekar, V., Lim, S., Microphysical retrieval from dual frequency precipitation radar board GPM, Geoscience and Remote Sensing Symposium (IGARSS), 2010 IEEE International. IEEE, 2010.

49. Toshiaki, K., Nakamura, K., Rainfall parameter estimation from dual-radar measurements combining reflectivity profile and path-integrated attenuation. J. Atmos. Oceanic Technol., 8, 1991, pp 259–270.

50. V. N. Bringi, V. Chandrasekar, J. Hubbert, E. Gorgucci, W. L. Randeu, and M. Schoenhuber, 2003: Raindrop size distribution in different climatic regimes from disdrometer and dual-polarized radar analysis. J. Atmos. Sci., 60, 354–365.

51. Malinga, S. J., Owolawi,P. A., Obtaining raindrop size model using method of moment and its applications for South Africa radio systems, Progress In Electromagnetics Research B 46, 2013, pp 119-138.

52. Fujiwara, M., Raindrop-size distribution from individual storms, Journal of the Atmospheric Sciences 22.5, 1965, 585-591.

53. Beard, K. V., Chuang, C., A new model for the equilibrium shape of raindrops, Journal of the Atmospheric sciences 44.11,1987, pp 1509-1524.

54. Pruppacher, H. R., Pitter, R. L.., A semi-empirical determination of the shape of cloud and rain drops, Journal of the atmospheric sciences 28.1,1971.

55. Brandes, E. A., Guifu Z., Vivekanandan, J.,Experiments in rainfall estimation with a polarimetric radar in a subtropical environment, Journal of Applied Meteorology 41.6, 2002, pp 674-685, 86-94.

56. National Research Council (NRC), 2004: “Where the Weather Meets the Road: A Research Agenda for Improving Road Weather Services,” National Academies Press, www.nap.edu/catalog/10893.html.

57. Sihvola, A. H., Electromagnetic mixing formulas and applications. No. 47., 1999.

58. Gunn, K. L. S., Marshall, J. S., The distribution with size of aggregate snowflakes, Journal of Meteorology 15.5, 1958, pp 452-461.

59. Sekhon, R. S., Srivastava, R.C., Snow size spectra and radar reflectivity, Journal of the Atmospheric Sciences 27.2, 1970, pp 299-307.

60. Orzel, K., Masiunas, L., Hartley T., Frasier, S., Deployment of the X-band dual polarization phased array radar in the Dallas-Forth Worth Urban Demonstration Network, ERAD, 2014.

61. Orzel, K., X-band Dual Polarization Phased-Array Radar for Meteorological Applications (2015).

62. Ermis, S., Tjuatja, S., A microwave backscattering model for the rain column, Geoscience and Remote Sensing Symposium (IGARSS), 2013 IEEE International, 21-26 July 2013

63. Ermis, S., Orzel, K. , Tjuatja , S., Frasier, S., A microwave scattering model for ground-based remote sensing of snowfall and freezing rain, Geoscience and Remote Sensing Symposium (IGARSS), 2015 IEEE International, 22-28 July 2015

Biographical Information

Seda Ermis was born in Mersin, Turkey, in 1984. She received her B.S. and M.S degrees in Electrical Engineering department from Mersin University, Turkiye, in 2006 and in 2009. Afterwards, she started her Ph.D. study in Electrical Engineering at the University of Texas at Arlington in 2010. She completed her Ph.D. under the supervision of Saibun Tjuatja in July, 2015. Her research area involves geophysical modelling of precipitation for calculation of back scattered electromagnetic wave.